1-1-2018

Automated CFD Optimization to Maximize Wind Farms Performance and Land Use

Rafael Valotta Rodrigues
University of Denver

Automated CFD Optimization to Maximize Wind Farms Performance and Land Use

_____

A Dissertation

Presented to

the Faculty of the Daniel Felix Ritchie School of Engineering and Computer Science

University of Denver

_____

In Partial Fulfillment

of the Requirements for the Degree

Doctor of Philosophy

_____

By

Rafael V. Rodrigues

November 2018

Advisor: Corinne S. Lengsfeld

Author: Rafael V. Rodrigues
Title: Automated CFD Optimization to Maximize Wind Farms Performance and Land Use
Advisor: Corinne S. Lengsfeld
Degree Date: November 2018

Abstract

In this research, a computational system was designed to analyze and optimize the layout of wind farms under variable operational conditions. At first, a wind turbine computational fluid dynamic (CFD) model was developed covering the near wake. The near wake flow field was validated against near wake velocity data from the MEXICO experiment. The CFD simulation demonstrated that the tip speed ratio and the pitch angle greatly influence the near wake behavior, affecting the velocity deficit and the turbulence intensity profile in this region. The CFD model was extended to cover the far wake, aiming to become a computational tool applicable to propose a solution to the Wind Farm Layout Optimization Problem. The CFD model was then coupled to a MATLAB optimization routine, working in an automated way to find optimized solutions to maximize wind farm land use. The study concludes that it is possible to have a significant improvement on the use of land and output power production by staggering the first row of turbines away from the wake effects. The staggered configuration achieved 10% improvement in the use of land compared with an aligned configuration, both of them working under the same operational conditions. Additionally, control strategies can result in benefits for the wind farm: two cases studies showed improvements within 2.52% and 4.63% in the output power. The last study of this dissertation implemented different inlet velocity profiles to evaluate the impact of vertical wind shear on wake profiles. At the heights analyzed,

different velocity inlet profiles did not result in significant changes to the wake of the wind turbine. The velocity deficit remained approximately the same for the three approaches (log law, HRRR and constant inlet) implemented in this work. The vertical wind shear might be more significant at higher altitude and for greater wind turbine diameters. Moreover, a transient model based on LES theory showed that there can be changes in the direction of propagation of the wake when velocity fluctuations are introduced to the model.

Acknowledgments

I am thankful for the opportunity of becoming a Doctor of Philosophy in Mechanical Engineering at the University of Denver. My acknowledgments to CNPq, the sponsor of this research. I am thankful to my wife Mayra Vidal, for supporting me during this journey. My adviser Corinne Lengsfeld, I am really thankful for all the support. I am never going to forget the research lunch events, some of the most enjoyable days of my daily routine at DU. I am thankful to all my lab partners that supported me during this whole time, in special to Donn Sederstrom and Meagen Puryer. I am thankful to my family that lives in Brazil (Mariana, Camile, and Antonio), but never let me down when I most needed. And most important: I dedicate this research to everyone that somehow advocates for the use of clean renewable energy sources.

Table of Contents

List of Figures

List of Tables

Chapter 1. Introduction

Limited carbon resources and environmental concerns are some of the reasons leading the energy industry to exploit alternative energy sources. Wind energy systems have been developed and applied for sites with suitable conditions since the first modern commercial-scale wind turbines placed in United States approximately 40 years ago. At the present, the most common and profitable applications for wind energy systems are wind farms. In large wind farms, the turbines are usually arranged in rows. This configuration requires a massive amount of land to overcome wake effects, which can decrease the output power and the components' useful lifetime. Wake effects are characterized by the formation of slower and more turbulent air behind the wind turbine, thus organizing wind turbines in a row might result in stronger effects of wake from one turbine to another. Optimizing the land use in wind farms is important because some countries do not have enough land availability for wind farms, while others have geographical constraints or obstacles which can negatively influence the local wind flow regime. Furthermore, a substantial increase in land used for wind farms will be required, as the capacity of wind energy generated and size of rotors continue to increase. For instance, the world total cumulative capacity reached 539 GW at the end of 2017, which represented 10.67% in the global cumulative wind installed capacity in comparison with 2016. Additionally, the size of the rotor increased from 40m diameter in 1990 to approximately 125m in 2015 [1].

Not to mention that the most profitable areas with the highest wind energy potential are limited, reinforcing the necessity for more efficient wind farm layouts.

1.1 Wind Farm Layout Optimization Problem (WFLOP)

An important phase of a wind farm design is solving the Farm Layout Optimization Problem (WFLOP), which consists of optimally positioning the turbines within the wind farm to minimize wake effects and therefore the expected power production is maximized [2]. Several studies attempt to computationally optimize the layout of wind turbines. However, little rigorous work has been done to optimize the wind farm layout to minimize wake effects and maximize power output based on specific hub location. Computational Fluid Dynamics (CFD) models are powerful tools capable of providing a rigorous level of accuracy to evaluate wake aerodynamics characteristics. The first aspect to consider is to define what wind farm characteristics the CFD model will in fact capture. There are two characteristics of wind turbine wakes that are critical for wind farm design: (a) The velocity deficit, which is related to the power loss from the wind turbine; and (b) The turbulence levels, which may influence rotor loads on downstream turbines affecting turbines components fatigue lifetime. The influence on both power losses and components fatigue are characteristics closely related to wind turbine wakes. This means that a wind turbine CFD model must account for wake effects to determine how the output power and turbine components lifetime are affected by the wind farm layout and the operational conditions. In order to evaluate the accuracy of the CFD model's prediction, the results from the CFD simulation must be validated by comparing the computational results with real life observations.

1.2 Wake Numerical Models

As a wind turbine extracts energy from the incident wind, a wake region characterized by reduced velocity and increased turbulence intensity levels is formed behind the rotor. The wake region can be classified according to the downstream distance from the rotor [3]:

(1) Near-Wake: region immediately behind the turbine, characterized by wake expansion that causes the velocity deficit to attain its maximum value between 1D (D is the rotor diameter) and 2D. The near wake ends between 2D and 4D. The turbine's design and loading strongly influence wake development.

(2) Far-wake: the flow is influenced indirectly by the turbine in terms of the velocity deficit and enhanced turbulence. There are three main sources of turbulence: atmospheric (surface roughness and heating), mechanical (rotor and tower) and the shear layer. The velocity deficit is often negligible beyond 10D but the increased turbulence intensity is sensible as far as 15D.

The main physical models to predict the wake behavior are: the Jensen Model, the Reynolds Averaged Navier Stokes Equations (RANS), and the Large Eddy Simulation (LES).

1.2.1 Jensen Model

The physical sketch of the Jensen Model (Fig. 1.1) represents the wind turbine with the black rectangle at the left side. The wake radius r_1 in Eq. (1.1) is a function of the downstream distance from the wind turbine (x distance), as well as the non-dimensional parameter α which is defined by the Eq. (1.2) and the rotor radius r_r .

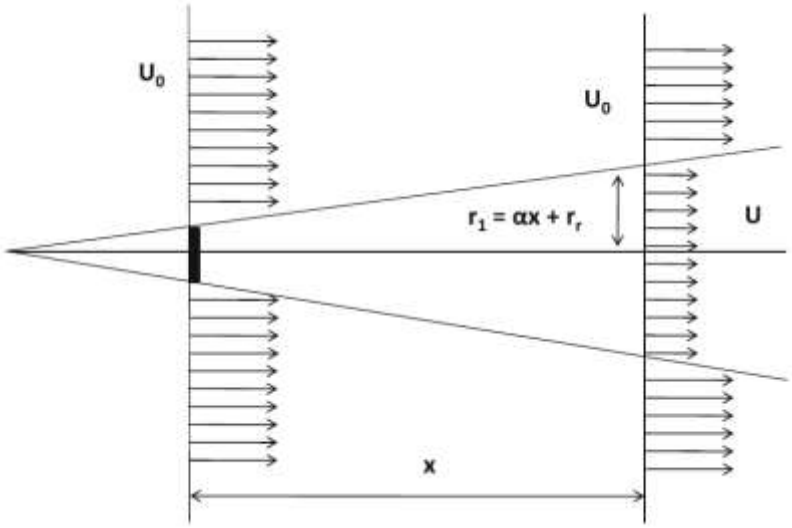

Figure 1.1 - Representation of the wake effect[2]. The black rectangle in the left represents the wind turbine.

$$r_1 = \alpha x + r_r \tag{1.1}$$

$$\alpha = \frac{0.5}{\ln \frac{z}{z_0}} \tag{1.2}$$

Where z is the hub height of the wind turbine and z_0 is the surface roughness.

Let i be the position of the wind turbine that generates wake, and j the position of the wind turbine affected by the wake, u_0 the ambient velocity, and u_j the velocity at the position j. The velocity deficit is calculated using Eqs. (1.3) and (1.4):

$$u_j = u_0(1 - vd_{ij}) \tag{1.3}$$

$$vd_{ij} = \frac{2a}{1+\alpha\left(\frac{x_{ij}}{r_d}\right)^2} \tag{1.4}$$

Where vd_{ij} is the velocity deficit induced on position j by the wake generated by i, x_{ij} is the distance between the positions i and j, and r_d is the downstream rotor radius.

The term *a* in the numerator of Eq. (4) is called axial induction factor which is represented by the Eq. (1.5). This term represents the ratio between the velocity right before the windmill and the velocity after the windmill in the wake.

$$a = (1-\sqrt{1-C_T}) \tag{1.5}$$

Where C_T represents the thrust coefficient of the rotor.

Eq. (1.6) shows the how the downstream rotor radius (r_d) is related to the axial induction factor *a*:

$$r_d = r_r\sqrt{\frac{1-a}{1-2a}} \tag{1.6}$$

1.2.2 Wake CFD Modeling

The Jensen Model is one of the first analytical physical models developed to characterize the velocity deficit for wind turbine wakes. Wind farms experience a significant range of different operational conditions, for instance, the rotational speed of the turbines changes instantaneously as well as the incident wind. These conditions may severely affect the wake aerodynamics, however, analytical models such as the Jensen Model in general do not account for variability in the operational conditions. CFD models are capable of simulating variable operating conditions, accounting for the influence of

important wind turbine design parameters on the wake behavior, such as blade geometry and rotational speed.

• Reynolds Averaged Navier Stokes (RANS) equations: most engineering models resolve the wake turbulence with RANS models. The model´s constants are predetermined using aerodynamic data from wind farms[4].

$$u = \overline{u} + u' \tag{1.7}$$

Where u is a vector and u' is its ensemble average over many realizations of the flow.

$$\frac{\partial \overline{u_i}}{\partial x_i} = 0 \tag{1.8}$$

$$\frac{\partial(\rho_0 \overline{u_i})}{\partial t} + \frac{\partial(\rho_0 \overline{u_i u_j})}{\partial x_j} = -\frac{\partial \overline{p}}{\partial x_i} + \frac{\partial}{\partial x}\left(\mu\left(\frac{\partial \overline{u_i}}{\partial x_j} + \frac{\partial \overline{u_j}}{\partial x_i}\right)\right) - \frac{\partial \tau_{ij}^R}{\partial x_j} + \rho_0 \overline{f_i} + f_{c^{\epsilon ij3}} u_j \tag{1.9}$$

Where p is the pressure, μ is the molecular viscosity, u_i is the component of velocity along the ith direction, t is the time, x_i is the position vector, $f_c{}^{\varepsilon ij3}u_j$, $\tau_{ij}{}^R$ is equal to $\overline{u'_i u'_j}$ and comes from the decomposition of the convective term and dictates the transport of mass and momentum due to the fluctuating velocity u'. $\tau_{ij}{}^R$ represents the closure problem in terms of known ensemble-averaged flow variables.

• Large Eddy Simulation (LES): enables the analysis of phenomena like gusts, atmospheric stratification and even the effect of wind farms on local weather. LES resolves all eddies size scales, except the ones compared to the smallest scale Kolmogorov [4].

• Filtered Navier-Stokes equations: a filter is an operator that is high-pass in scale size and removes eddies that are smaller than the filter's cut-off length. Upon filtering the incompressible NS equations in the absence of body forces [4].

• The advantage of LES over engineering models is its ability to capture the transient evolution of turbulent eddies that are most relevant to wake development and power production. The use of RANS instead of LES may save computational effort but increase dependency on experimental data [4].

1.3 Wake Experiments

There are three ways to measure wake effects [5]. The first one is to collect data for a single turbine in a full-scale field test. The second one is to collect data for one turbine working in the wake of another one. The last one is to collect data from a controlled reduced-scale test in a wind tunnel.

1.3.1 Low-speed Wind Tunnel Experiments

In the case of a controlled reduced-scale test, a prototype has to fit into a wind tunnel. Two main problems with this approach are the scaling effects and the blockage effects (wind tunnel wall interference). However, wind tunnel tests are still preferred to field tests because the incoming flow in field tests is much more difficult to describe in sufficient detail [6]. Full-scale tests are much more expensive to carry out, and it is rarely possible to get all the information needed to act as a well-defined test case for CFD[6]. A full review of low-speed wind tunnel studies and scaled turbines is provided by Crespo et al[3].

1.3.2 Full-Scale Field Tests

A wind farm is a huge financial investment, therefore even small wind velocity fluctuations can severely affect the payback to the investor. When attempting to prospect

suitable atmospheric conditions for wind farms, the wind velocity must be carefully measured at the wind turbine hub height, which corresponds to the center height of the rotor. The incident wind angle needs to be measured because the atmospheric wind is multidirectional. Furthermore, the potential electrical power generated is not only a function of the wind velocity and direction, but it also depends on the air density. Therefore, the pressure and temperature need be measured in order to determine the instant available power at the site according to the incident wind.

Field tests are usually meant to assess proper atmospheric conditions for wind farms, as well as to estimate the output power curve as a function of the incident wind. However, this is not necessarily the best option for validating a wind farm simulation because the inflow and the flow behind the wind turbines are subjected to atmospheric conditions. These conditions are more difficult to measure and to determine reliable average values because of the inherent wind fluctuations present in the natural environment. If a field test is utilized to validate a CFD wind farm model, the repeatability of the results from the test is not guaranteed.

There are two ways to perform field tests: meteorological mast or SoDar (Sound Detection and Ranging) / LiDar (Light Detection and Ranging) Technologies. In the case of a meteorological mast test, the natural atmospheric environment of a real wind farm could be used to collect the necessary experimental data upstream from the wind turbine. However, a dataset collected from atmospheric conditions is much more difficult to interpret. Because average velocity values are more difficult to determine, characterizing the wind flow is not necessarily an easy task. These difficulties occur because the wind direction changes instantaneously, therefore the conditions are not controlled and the

inflow wind is not well determined. In summary, the meteorological mast method would have severe limitations if the objective were to validate a wind turbine farm simulation.

A more accurate methodology would be using SoDar (Sonic Detection and Ranging) and LiDar (Light Detection and Ranging), however the cost for deployment of these devices is expensive. The SoDar technology is comparable to radar systems. Instead of radio signals, SoDar systems send out tone pulses into the atmosphere. The sound is reflected by small temperature variations. The reflected sound has a different frequency from the transmitted, due to the Doppler Effect. The difference between both frequencies is used to calculate wind speed and direction. The LiDar technology measures wind conditions with the help of a laser beam, which is reflected by aerosols moved by the wind flow. The system evaluates the frequency shift caused by the Doppler Effect between sent and received signals. By measuring at least three different directions, wind speed and wind direction can be calculated[7].

1.4 Designing an Experiment for CFD Validation

1.4.1 Requirements

An experimental dataset to validate a wind farm CFD model must reflect the typical operational range of commercial-scale wind turbines, which includes:

- Diameters varying between 40m to 90m
- Typical rotational speeds of the blades between 5 and 20 rpm
- Two or three blades and horizontal axis (for wind farms)
- The towers have increased to 400ft.
- Velocity range: Cut-in velocity: 3m/s and Cut-out velocity=25m/s
- Power range: commercial scale is around 2MW

In order to satisfy these requirements, the design of an experiment to validate a wind turbine farm simulation should basically have the subsystems shown in the Functional Decomposition Diagram from Fig. 1.2: the Upstream Environment, Rotor and Downstream Environment.

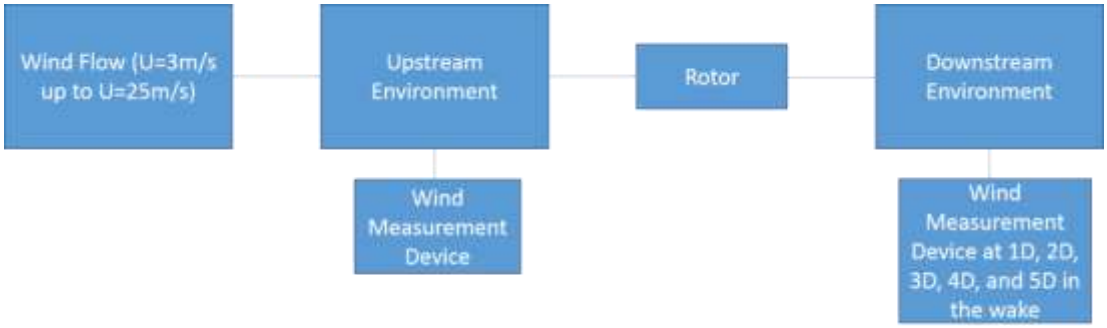

Figure 1.2 - Functional Decomposition Diagram.

1.4.2 Assumptions

Computationally modelling an entire wind farm is intensive and assumptions have to be made to run a full parametric optimization. Among all factors affecting wind turbine farm layout design, the following factors are within the scope of this study:

- The layout optimization routine is based on: 1) maximizing the output power; and 2) minimizing the use of land.

- Either the horizontal or vertical length are considered valid options in order to achieve optimized layouts.

- It is almost impossible to match the same Reynolds number conditions for a wind turbine prototype and a full-scale model. However, the prototype can correctly reflect the

full-scale (wake) operational conditions if the Tip Speed Ratio of the full-scale rotor and the prototype is kept the same.

- If the Tip Speed Ratio of the prototype and the full-scale rotors are kept the same, the wake conditions do not greatly vary as a function of the Reynolds Number.

- The terrain of the wind farm is assumed to have uniform topography, meaning that possible topography variations are not going to be accounted.

1.4.3 Identification of Key Technical Issues

1.4.3.1 Wake Characterization

Subsystem Affected: Downstream Environment

A typical wind farm layout has wind turbines arranged in rows, so that a layout will always have a wind turbine working in the wake of another one. Thus, the downstream environment subsystem must be properly characterized because the output power as well as the wind turbine lifetime components can be severely affected. The mean wind velocity and the velocity fluctuations are the parameters to be measured in this region in order to determine the velocity deficit and the turbulence intensity. The velocity deficit affects the output power and the turbulence intensity affects the turbine component's lifetime.

1.4.3.2 Scaling Effects

Subsystem Affected: Rotor / Downstream Environment

The use of wind turbine prototypes is a possibility for collecting the necessary data to validate a wind turbine farm simulation. However, the similarity between the prototype and the full-scale rotor must be ensured in order to have reliable results. The π-Buckingan dimensionless parameters may be used to correlate the models, and the prototype must basically experience similar conditions for these design parameters.

1.4.3.2.1 Reynolds Number

The velocity operational range for commercial wind turbines is commonly 3m/s up to 25m/s, as described by the requirement 1.4.1. The Reynolds number of a full-scale turbine is different compared to the prototype because of the chord length, as Eq. (1.10) states. The prototype Reynolds number will need to be equal to the Reynolds number of the full-scale turbine if the wake conditions are desired to be reproduced exactly. Eq. (1.11) and Table A.1 (Appendix A) show how it is difficult for the rotors to have the same Reynolds number because of the velocity that would be required for the prototype. For instance, if the ratio between the chord lengths is 15, the incident wind velocity on the prototype would need to reach up to 375m/s (Vp) in order to keep the same Reynolds number of the full-scale model. This conditions are obviously extremely difficult to achieve.

$$\mathrm{Re} = \frac{\rho V_{REL} c}{\mu} \tag{1.10}$$

$$\frac{\rho \cdot V_p \cdot c_p}{\mu} = \frac{\rho \cdot V_f \cdot c_f}{\mu}$$
$$V_p = \frac{V_f \cdot c_f}{c_p} \tag{1.11}$$

1.4.3.2.2 Tip Speed Ratio

Alternatively, the Tip Speed Ratio (TSR) is a design parameter to derive aerodynamic performance (Eq. 1.12). The TSR and the Reynolds number are π-Buckingan

non-dimensional parameters to correlate scaled rotors. According to the TSR value, the wind relative velocity varies and this affects the lift force as well as the behavior of the wake. Eq. (1.14) demonstrates that a prototype may easily achieve the typical Blade Tip Speed (BTS) of the commercial full-scale models (considering 5rpm angular velocity). This way, although the similarity with regards to the Reynolds number is difficult to reach, the similarity is assured with regards to the TSR.

$$\lambda = \frac{\omega R}{U} = \frac{Blade\ Tip\ Speed}{Wind\ Free{-}Stream\ Velocity} \tag{1.12}$$

$$5rpm = 5 * \frac{2\pi}{60} \frac{rad}{s} = 0.524 \frac{rad}{s} \tag{1.13}$$

$$BTS = \frac{0.524 rad}{s} * 45m = 23.56 m/s \tag{1.14}$$

1.4.3.3 Blockage Effects

Subsystem Affected: Upstream Environment / Rotor / Downstream Environment

A wind tunnel may simulate the environmental conditions and it is possible to work in a controlled environment, however the air flow conditions are affected by the friction in the region adjacent to the wind tunnel walls. The Blockage Ratio is defined as the ratio between the rotor area and the wind tunnel cross-sectional area (Eq. 1.15). The Blockage Ratio level widely acceptable for most of the literature studies is 10%, thus this is the

reference value adopted in the present experimental design to avoid undesirable effects compromising the reliability of the experiment.

$$B.R. = \frac{RotorArea}{WindTunnelArea} \leq 0.1 \tag{1.15}$$

1.4.4 Alternatives for Experimental Design to Validate a CFD Model

1.4.4.1 Field Experiment - Meteorological Mast

In order to use full-scale field tests to validate a wind turbine farm simulation, the sizing proposal for the anemometer tower must follow some requirements proposed by the IEC 64000-12-1 standard [8]. This guide is intended to determine power curves of wind turbines according to the incident wind on the rotor. An example of a meteorological mast sizing based on this standard is shown in Fig. 1.3. The sizing specified in Fig. 1.3 would be meant for a 70 m rotor diameter at an 80 m tower height and it basically consists in:

- The horizontal spacing between the tower and the control anemometer is recommended to be 8.2 times the tower diameter. So the total horizontal length of the support rod indicated by the letter "y" of the Fig. 3 should be 16.4 times the tower diameter. This recommendation is intended to avoid the tower to interfere with the incident wind on the anemometer.

- The vertical distance between the control anemometer rotation plane and the horizontal rod (distance x of Fig. 1.3) is a function of the support rod diameter. The IEC 61400-12-1 states that the vertical length of the support rod shall be 15 to 20 times the

support rod diameter. Again, this is a precaution to avoid interferences on the fluid flow and consequently interfere with the measurements done by the anemometer.

- The anemoscope and the control anemometer should be installed close to the hub height, which in this case is 80 meters. The distance proposed (72 meters) is 10% below the hub height, and it is safe for this requirement.

- The thermocouple and the barometer should be installed at least 1.5 diameters below the rotor diameter. The rotor diameter is 70 meters, so that 1.5 times the rotor diameter is greater than the tower height. Therefore, the best alternative is to use the closest distance to the ground (the distance z of Fig. 1.3) to install the thermocouple and the barometer.

- The IEC 61400-12-1 standard recommends each anemometer tower (upstream and downstream) to be at a minimum distance of 2.5 times the rotor diameter (and maximum 4D), which corresponds to 175 meters.

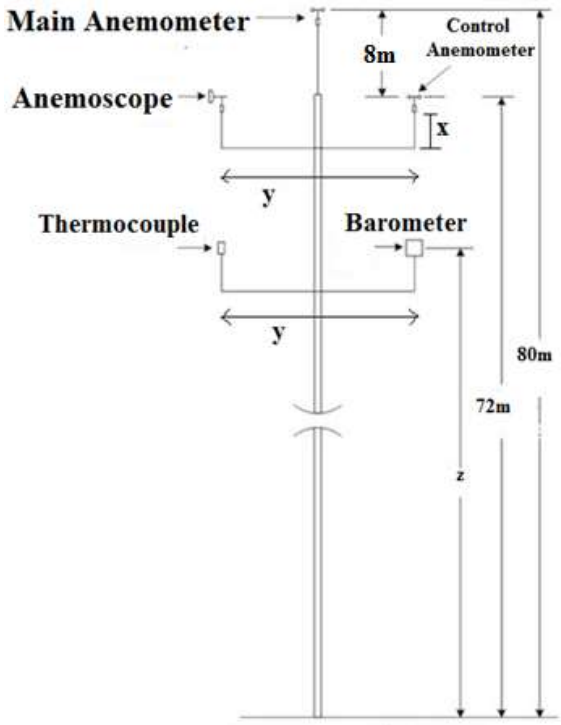

Figure 1.3 - Sizing proposal for the instrumented anemometer tower to measure velocity upstream a wind turbine and downstream (in the wake) and consequent power deficit.

The upstream velocity of the wind turbine could alternatively be measured below the hub height of the wind turbine. Therefore, a smaller support tower would be needed and the design could potentially be cheaper. The power law could be used to extrapolate data for a taller height from data from a smaller height tower using the power law (Eq. 1.16). The mentioned extrapolation requires assuming data for the surface roughness of the terrain, which can be found in literature for the main types of terrain. The previous extrapolation is not going to work properly for downstream velocity because of the wake effects. The α value is usually less than 1/7 during the day to more than ½ during the night.

$$V = V_0 \left(\frac{z}{z_0} \right)^{\alpha} \tag{1.16}$$

1.4.4.2 Low-Speed Wind Tunnel

The upstream environmental conditions may be simulated using a low-speed wind tunnel to create artificial air flow. This alternative creates controlled upstream conditions instead of atmospheric conditions, which are not controllable. The instrumentation required for creating and measuring the artificial air flow to simulate the incident wind is:

- Hot-wire anemometer: intended to do velocity measurements and turbulence intensity measurements (velocity fluctuations). The resolution of most commercial-scale sensors are usually 0.1m/s [18], which is suitable for reaching CFD validation requirements. Alternatively, other wind measurements devices could be utilized such as Particle Image Velocimetry (PIV). PIV measurements are more accurate, however, this type of experiment is highly complex because of the possibility of external factors interfering on the results, such as external light or vibration and velocity fluctuations close to solid surfaces.

- Axial Fan: meant to provide air flow. The axial fan must be designed according to Eq. (1.17) and (1.18), and the physical concepts from Fig. 1.4.

- Inverter: intended to control the velocity intensity by controlling the power of the fan.

- Honeycomb: intended to direct the flow in a straight trajectory.

A low-speed wind tunnel can be constructed using a subsonic nozzle (test section) followed by a diffuser (Fig. 1.4). The velocity is smaller than the sound velocity, it means that the Mach number (represented by Mp, Ms and Md) is smaller than one. The approach for designing the wind tunnel geometry is based on the Conservation of Mass Law (Eq. 1.17), as well as the Bernoulli Equation (Eq. 1.18). This approach may be used in order to

estimate the required power for the axial fan, as well as the test section dimensions / contraction ratio of the wind tunnel.

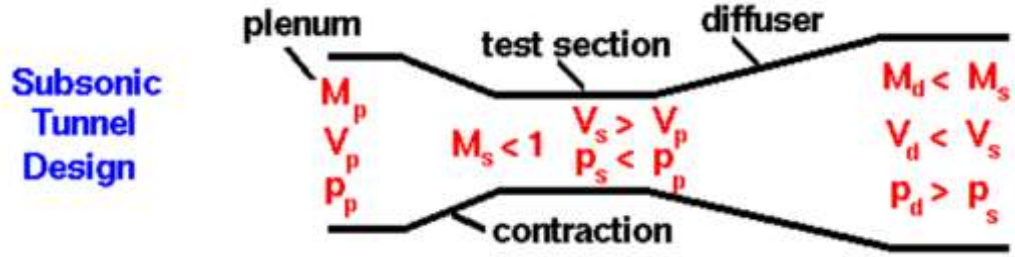

Figure 1.4 - Subsonic Tunnel Design.
Source: NASA, 2015 [9].

$$Q_{inlet} = Q_{test\ section}$$
$$A_{inlet} \cdot V_{inlet} = A_{test\ section} \cdot V_{test\ section} \tag{1.17}$$

$$\dot{W}_{pump} = \dot{m}\left[\left(\frac{p}{\rho} + \frac{\overline{V}^2}{2} + gz\right)_{test\ section} - \left(\frac{p}{\rho} + \frac{\overline{V}^2}{2} + gz\right)_{inlet}\right] \tag{1.18}$$

The test section of the wind tunnel is where the rotor has to be placed. A very important key requirement for the wind tunnel is related to blockage effects. As previously mentioned, the blockage ratio must be no greater than 10% in order to avoid interference on the air flow. Table 1 shows how the blockage ratio requirements dictate the required wind tunnel dimensions according to the rotor diameter, considering a rectangular cross-sectional test section area. Table 1.1 basically provides the wind tunnel sizing requirements to avoid wall interference. For instance, the wind tunnel should have a lateral length of 208

meters and a vertical length of 312 meters to test a wind turbine with a rotor of 90.9 meters in diameter.

Table 1.1 - Blockage ratio as a function of the rotor diameter and the wind-tunnel dimensions. LH is the lateral length of the tunnel, LV is the vertical length, and d prot is the diameter of the prototype.

LH (m)	LV (m)	Area LH*LV [m^2]	D (m)
200	300	60000	87.40
201	301.5	60601.5	87.84
202	303	61206	88.28
203	304.5	61813.5	88.71
204	306	62424	89.15
205	307.5	63037.5	89.59
206	309	63654	90.03
207	310.5	64273.5	90.46
208	312	64896	90.90

An important conclusion from Table 1.1 is: a wind tunnel for a full-scale model satisfying the requirement 1.4.1 and the requirements for the blockage ratio / wall interference is not technically viable because of its large dimensions. This conclusion justifies the necessity for a wind turbine prototype to represent the typical operational conditions of wind farms, and Table 1.2 provides the prototype diameters and wind tunnel dimensions to satisfy all requirements. For instance, the wind tunnel would need a lateral length of 24 meters and a vertical length of 36 meters to test a prototype with a rotor of

10.49 meters in diameter. Specifically, the last dimension values (wind tunnel and prototype) of the table are approximately the same as the wind turbine prototype tested in the NASA Ames Wind Tunnel[10]. This was one of most comprehensive large scale experiments in the field of wind turbine aerodynamics, providing a reliable database that may be used for validation purposes. However, a weakness of the NASA Ames experiment was the lack of wake / downstream velocity measurements.

Table 1.2 - Blockage ratio as a function of the rotor diameter and the wind-tunnel dimensions. LH is the lateral length of the tunnel, LV is the vertical length, and d prot is the diameter of the prototype.

LH (m)	**LV (m)**	**Area LH*LV (m^2)**	**d prot (m)**
5	7.5	37.5	2.19
6	9	54	2.62
7	10.5	73.5	3.06
8	12	96	3.50
9	13.5	121.5	3.93
10	15	150	4.37
11	16.5	181.5	4.81
12	18	216	5.24
13	19.5	253.5	5.68
14	21	294	6.12
15	22.5	337.5	6.56
16	24	384	6.99
17	25.5	433.5	7.43

18	27	486	7.87
19	28.5	541.5	8.30
20	30	600	8.74
21	31.5	661.5	9.18
22	33	726	9.61
23	34.5	793.5	10.05
24	36	864	10.49

An important aspect to determine the wake behavior is the velocity deficit caused by the obstacle (rotor), because it can greatly affect the incident wind on the downstream rotor since wind turbines are arranged in a row in wind farms. The wind velocity deficit is calculated comparing the velocity measured in the near wake of the rotor and the upstream velocity. The velocity profile must be measured over the rotor extension, and the measurements should cover the near wake length. The Jensen Model assumptions are suitable to determine the extension necessary to collect velocity measurements, and to determine the region affected by velocity deficit.

Fig. 1.5 and Table 1.3 show the rotor wake lateral extension at distances equal to 1D, 2D, 3D, 4D, and 5D, based on a prototype diameter of D=10.5m. According to the Jensen model, this is the region affected by the velocity deficit, and this information was used to determine the extension required for the measurements. As previously mentioned, the prototype rotor diameter (D=10.5 m, Table 1.2) was determined considering blockage effects and attempting to avoid Reynolds number discrepancy as much as possible. Furthermore, the CFD models usually have the required level for validation from 1% up to

10%. Consequently, most of the commercial sensors available in the market are suitable for this purpose. The required sensor for the downstream environment is the same sensor required for the upstream environment, the Hot-Wire Anemometer or alternatively a PIV measurement system.

The assumption 1.4.2 states that either vertical or horizontal lengths are possibilities for obtaining optimized wind farm layouts. This justifies the necessity for measurement points located on horizontal and vertical positions in order to cover the whole wake radius as much as possible. As Fig. 1.5 and Fig. 1.6 show, the required number of measurement points is 9 points for each downstream location corresponding to the wake radius and one additional upstream point to control the upstream velocity. Thus, five downstream locations spaced by a distance D (rotor diameter) would require 45 measurement points in order to be able to characterize the full near wake length. So, the total number of measurement points is 46 points but only two Hot –Wire Anemometers are required. One of the sensors would be at an upstream position and the other would have variable position at each of the 9 points on each wake radius extension. It is preferable to do that instead of using 46 Hot-Wire Anemometers for two reasons: (1) The sensors would certainly interfere and modify the downstream wind flow, and (2) the associated costs to include 46 Hot-Wire Anemometer sensors could be prohibitive.

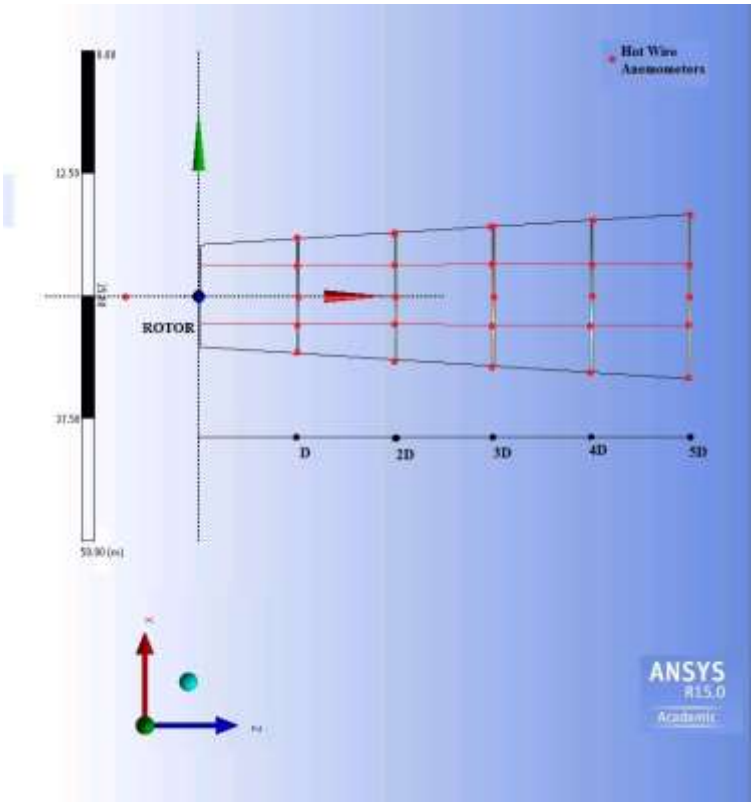

Figure 1.5 - Top view of the rotor and the measurement points to collect velocity data. The wake rotor is estimated using the Jensen Model.

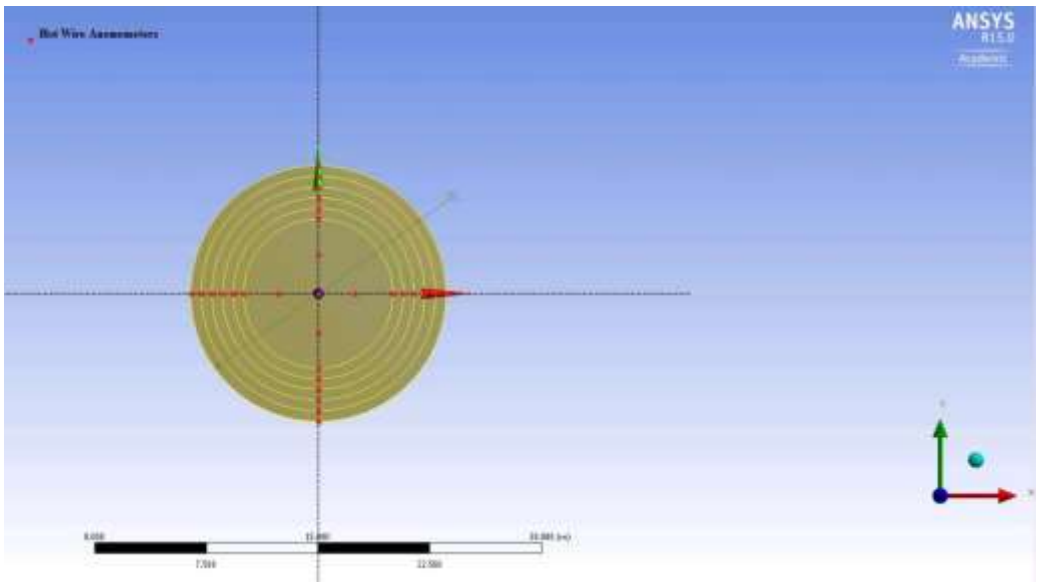

Figure 1.6 – Front view of the rotor and the measurement points to collect velocity data. The wake rotor is estimated using the Jensen Model.

Table 1.3 - Wake radius calculations based on the Jensen Model assumptions.

Dd (diameters)	x (m)	rr (m)	z (m)	z0 (m)	α	r1 (m)	Wake d1 (m)
1	10	5	60	0.055	0.071482	5.71	11.43
2	20	5	60	0.055	0.071482	6.43	12.86
3	30	5	60	0.055	0.071482	7.14	14.29
4	40	5	60	0.055	0.071482	7.86	15.72
5	50	5	60	0.055	0.071482	8.57	17.15

Legend: Dd is the downstream distance in number of rotor diameters.

1.5 Limitations and Considerations

Field tests are subjected to atmospheric conditions, making it more difficult to obtain sufficient data to cover the whole operational range. Field tests are important for predicting suitable climate conditions for wind farms. However, other aspects have to be considered if one is aiming to validate a computational simulation. For instance, it is desirable to control the conditions upstream of the wind turbine to investigate potential effects influencing the outputs. Additionally, specified conditions applied in the computational domain may be easily reproduced in a controlled environment. The same is not necessarily true in the field environment, where atmospheric conditions usually change the wind direction instantaneously. This by itself is potentially a barrier to validating a model.

For those reasons, the best way to validate a wind turbine CFD model is to use a wind tunnel experiment in a controlled environment. Wind tunnel tests are complex and expensive procedures, as shown in details in section 1.4.4.2. Therefore, **in this research we identified an existing dataset in literature to validate the CFD model.** The MEXICO (Model Experiments in Controlled Conditions)[11] experiment was one of the most

comprehensive collaborative efforts by the IEA (International Energy Agency), which created the task 29 to gain understanding about wind turbine wake aerodynamics, as well as to improve aerodynamic models used for wind turbine design. A series of tests for a small wind turbine prototype were performed using the DNW German Dutch open section wind tunnel using PIV to measure wake velocity flow field. This dataset was identified as the one most suitable to the goals of this research: validating a CFD wind turbine wake model. Although the rotor wake measurements of the MEXICO comprised only the near wake region right behind the wind turbine (up to 1.5D downstream of the rotor), the experiment is a very rich source of data useful to validate wind turbine CFD wake models.

1.6 Dissertation Overview

The objective of this dissertation is to develop and implement a computational model to optimize wind farm layout according to typical wind farm operational conditions. To do that, at first a wind turbine CFD model was developed and validated against near wake velocity data. Then, the model was extended to cover the far wake of the wind turbine. At this point, the influence of wind farm design parameters on the wake aerodynamic development was quantified, such as Pitch Angle, Tip Speed Ratio, and Free-Stream Velocity. The computational model was coupled with a MATLAB optimization routine. This dissertation is divided into 4 studies:

Study 1: This study shows the computational implementation and the validation of a wind turbine CFD model using of the MEXICO rotor. The validation of the model was performed against experimental wake data from literature (from the MEXICO experiment), including wake velocity data covering the near wake. Moreover, the influence of important wind farm design parameters on the near wake was evaluated.

Study 2: The second study was an extension of the wind turbine CFD model to cover the far wake of the wind turbine. The goal is to have a computational model capable of simulating the interaction between turbines in a wind farm. The physical domain of the CFD model from study 1 was extended to cover the far wake, allowing the study to quantify the influence of wind farm design parameters on the far wake aerodynamic development.

Study 3: The third study integrates the CFD model developed in the studies 1 and 2 with an optimization code developed and automated in MATLAB. The objective is to optimize wind farm land use by maximizing the ratio output power and area of the wind farm. This study shows the critical differences in using aligned or staggered rows in a wind farms, and the consequences in terms of power production and use of land. Additionally, control strategies are presented as a possibility for optimizing output power and use of land.

Study 4: The fourth study shows the computational implementation of more realistic wind shear profiles for the CFD model. Real time data was interpreted using the mesoscale model HRRR (High Rapid Radar Refresh), allowing the study to create a more realistic wind profile for specific weather conditions. The results were compared with the classic Log-Law approach, which is a method to evaluate wind shear profile.

Chapter 2: Development of a Computational System to Optimize Wind Farm Layout – Part I: Near Wake CFD Validation and Analysis

Abstract

This work describes the validation of a wind turbine farm CFD (Computational Fluid Dynamics) simulation using velocity wake data from the MEXICO experiment from literature. The work is intended to establish a computational framework from which to investigate wind farm layout. This work seeks to validate the simulation and identify parameters influencing the wake. Additionally, the wake analysis is extended beyond the operating range found in literature. A CFD model was designed to mimic the same experimental conditions of the experiment and simulate new operating conditions with regards to tip speed ratio and pitch angle. Results demonstrated that velocity deficit and the turbulence intensity in the near wake is strongly influenced by the tip speed ratio and the pitch angle. Considering the case corresponding to the designed tip speed ratio of TSR=6.6, the velocity in the wake increases at a rate of approximately 15% of the free-stream velocity per rotor diameter at the wake regardless the free-stream velocity applied. Moreover, analysis of a radial traverse right behind the rotor showed an increase of 20% in the velocity deficit as the TSR varies from TSR=6 to TSR=10, corresponding to an increase ratio of approximately 5% m/s per dimensionless unit of TSR.

2.1 Introduction

Limited carbon resources and environmental concerns are some of the reasons leading the energy industry to exploit alternative energy sources. Wind energy systems have been developed and applied for sites with suitable conditions, the first modern commercial-scale wind turbines were placed in United States approximately 40 years ago. Nowadays, the most common and profitable applications for wind energy systems are the large wind farms. Commercial-scale wind generators for wind farms are within 3MW and 5MW, and all have a predominantly horizontal axis and are three bladed. One problem of these large wind farms is the row arrangement of the generators. The towers are usually placed in rows, requiring large areas of land for rotors up to 100 meters in diameter. Previous research has suggested safe distances to avoid the wind turbines blade/components damage and output power waste. However, the optimum spacing between turbines in a wind farm is still a challenging and open question in wind energy research.

Several efforts using different methodologies have been done to achieve layout optimization, focusing on finding optimal spacing between turbines in a wind farm. Park & Law[12] applied sequential convex programming to maximize wind farm output power by optimizing the placement of wind turbines of the Horns wind farm in Denmark. They found that the optimal spacing between wind turbines is dependent on the wind direction. Scattering the turbines helped to avoid wake chain effects, so that downstream rotors were not significantly affected. Moreover, the same study considered wind statistical data to optimize the wind farm power production over a long period, resulting in a 7.3% power increase. Son et al.[13] found that the total wind farm output power is strongly related to the

distance between the first and second wind turbine rows. When the referred distance became larger, the output power considerably dropped in comparison to smaller distances. This means that the increase of the spacing between the first and second rows is ineffective in improving output power. On the other hand, decreased distances made the second wind turbine row much less efficient. They discovered the importance of keeping turbines as close as possible, but with enough space so that the second row can have guaranteed output power. Longer distances did not contribute to increase the total output power. Further, increasing the space between the fourth and the fifth rows has a better contribution than increasing the space between the first and second rows. Wu & Porté-Agel[14] investigated two layout configurations in the same area with 30 turbines either arranged in aligned or staggered conditions. In comparison to the aligned configuration, the staggered one allows better wake recovery. This exposes the downstream turbines to higher local wind speeds (consequently higher performance) and lower turbulence intensity. Stevens[15] found that the distance of 10 diameters (or higher) would minimize the cost per unit of energy production, and the same is true for a distance of 15 diameters if the objective function was evaluated using dimensionless parameters. Those value are significantly higher than applied values in wind farms (6-10 turbine diameters). Meyers[16] found that the current wind farms layout solutions in literature have characteristics with considerably lower spacing than computationally optimized layout solutions.

Moreover, other efforts have attempted to achieve wind farm optimization using control strategies to mitigate wake effects, applying sub-optimal operating conditions. This means that each rotor will not necessarily deliver the best aerodynamic performance, but the goal is to find the best solution that avoids wake interaction effects, increasing the total

wind farm output power. Park[17] studied control strategies for wake effects mitigation, showing that control techniques can be applied for each individual rotor to improve overall wind farm efficiency. González[18] proposed the individual selection of an operating point on each wind turbine in order to maximize the overall wind farm output power. This is performed by studying the optimal pitch angle and tip speed ratio of each rotor in regards to the total wind farm output power. Additionally, the methodology also allows decreased turbulence intensity levels in the produced wakes. The results showed increased power production when the wind speed is lower than the rated wind speed, and for non-prevailing wind directions. Lee[19] found an increase of 4.5% in the total output power by applying pitch angle control for the Horns Rev wind farm. Kazda[20] applied weakened wake conditions for upstream turbines by using sub-optimal operations through control strategies. They found that a 12.5% reduction for the upstream turbines resulted in a 2.5% increase in the sum of the upstream and downstream turbines. This could be achieved by either a change of 3.5° in the pitch angle or by a 24% reduction in TSR compared to optimum TSR. For the case of two upstream turbines operating at 87.5% of optimal conditions, the sum of total power of the upstream and downstream turbines increased by 9.7%. Gil[21] applied control strategies, achieving from 1.86% up to 6.24% in energy captured by using sub-optimal operating points. Chowdhurry[22] found that using variable rotor diameters improved efficiency, achieving 30% increase in the total power generation.

All these efforts in the literature described above provided relevant contributions to wind farm optimization and turbine spacing research. However, they did not consider a rigorous evaluation of three-dimensional wake effects, which this study will achieve. In the context of science applied to wind farm optimization, this work proposes a numerical

CFD (Computational Fluid Dynamics) model to rigorously analyze wind turbine wake flow field, characterizing wake flow characteristics for the most relevant wind farm parameters: velocity flow field and turbulence intensity. The current study will do a full computational analysis of the near-wake aerodynamic behavior, considering configurations not analyzed before in literature: several different loading, free-stream velocity and pitch angle conditions. The goal is to achieve a validated model by comparing computational and experimental data from existing literature. Engineering tools such as CFD or wake analytical methods have been improved to accurately characterize wake characteristics, but there are few experiments to effectively validate wind turbine wake flow. Literature shows a variety of techniques and different goals in regards to wind turbine CFD. The next section shows a description of the main experimental approaches found in literature, which will be useful to provide data to develop and validate the numerical model in this study.

2.2 Brief Description of Wind Tunnel Experiments

A full review of low-speed wind tunnel studies and scaled turbines is provided by Crespo et al.[3]; additionally, other recent relevant studies can be found in the literature [23-32]. Most of these studies are meant to validate wind turbine simulations, and some of them are described below to provide an overview of low-speed wind tunnel experiments. The objective of this literature review is to show the way that experimental data can be used in order to validate wind turbine simulations.

Wind turbine experiments conducted by the Norwegian University of Science and Technology validated the numerical results against wind tunnel measurements in terms of mean velocity, turbulence intensity and the power and thrust coefficients. This research

center has low-speed wind tunnel facilities, with dimensions of 2.71 m wide, 1.8m high and 11.1m long. An experimental study was performed using two aligned prototype rotors of 0.944 m and 0.894 m, and the blade consists of 14% S826 NREL profile for the two rotors[23]. The velocity profile was characterized using Pitot-Static tubes, and the thrust force was determined using a Six-Component Balance Force.

A qualitative study of the rotor wake behavior by Chamorro & Porté-Angel[24] analyzed a 150 mm diameter three-bladed wind turbine prototype, which was tested using a wind tunnel with 37.5m length driven by a 200hp fan. The experimental data was used to produce a qualitative study of the wake behavior, since the Reynolds number is different compared to full-scale wind turbines. A particularly interesting aspect that distinguishes this study from the others is that the authors were able to characterize the surface roughness by placing straight chains of approximately 5mm height covering a 10m section of the tunnel. These chains were aligned perpendicular to the flow direction and separated from each other by 0.20m. The mean wind velocity in the tunnel was measured using Pitot static tubes, and constant tip speed ratio values (λ=4.2 for smooth surfaces and λ=4.4 rough surfaces) were maintained in order to reflect the typical operational conditions of full-scale field turbines (typically $3 < \lambda < 6$).

In another experiment, a virtual wind-tunnel model (24.4m x 36.6m) with the same dimension of the NASA wind tunnel was analyzed using the ANSYS Fluent package[25]. The model validation was performed comparing the pressure coefficient at different span-wise sections along the turbine blade. In addition, the wind turbine output power was compared to published experimental results for the NREL phase VI rotor tested in the NASA wind tunnel. Several other studies in literature utilized data from the NREL/NASA

framework to develop CFD studies using pressure coefficient values on the blades and aerodynamic torque data for comparison and validation. Zhou[33] performed LES of the NREL phase IV to evaluate the effect of different inflow conditions on the aerodynamic loading and near wake characteristics. Hsu[34] implemented a finite-element (Lagrangian-Eulerian) model of the NREL Phase IV using a non-structured rotating mesh refined close to the rotor disc. Wake characterization was not the focus of the study, what explains the wake made out of coarse non-structured cells with no refinement. Gundling[35] evaluated low and high fidelity models using the NREL Phase VI for predicting wind turbine performance, aeroelastic behavior and wakes: 1) The Blade Element method with a free-vortex wake; 2) The actuator disc method; 3) The full-rotor method. Mo[36] did a study in more depth to understand wake aerodynamics performing a LES of the NREL Phase VI using dynamic Smagorinsky-model, additionally verification of the average Turbulence Intensity was performed against an analytical model. They found that the downstream distance where instability and vortex breakdowns occur is dependent on wind free-stream inlet conditions (7m/s happens at 4 rotor diameters, while 15.1m/s between 11 and 13 diameters), and a decrease of the turbulence intensity happened after instability and vortex breakdowns. Choudhry[37] performed a very similar CFD study of the NREL phase VI using computational methods very similar to the ones found in the study conducted by Mo[36], finding that regions of velocity deficit and high turbulence intensity are within the high vorticity region.

Sturge et al.[26] utilized an open-circuit suction tunnel, driven by an eight-blade axial fan positioned at the outlet. In this experiment, the wind speed is controlled by using a variable frequency drive. The air flow passes through a honeycomb mesh with cells 0.01m

wide and 0.1m long. The dimensions vary along the tunnel, with a 6.25:1 contraction section and 1.2m high x 1.2m wide x 3m long test section. Afterwards, analysis of static pressure along the blade showed a large reduction in the suction peak along the leading edge, which reduced the lift generated by the rotor and consequently the torque production.

The wake flow of a 5 x 5 array of 50mm micro-wind turbines was studied and analyzed by Houssain et al[28] using a wind tunnel. These 1/10 scaled prototypes were placed in a 3m x 1.8m wind tunnel, allowing the velocity profile and turbulence intensity (velocity fluctuations) behind the array to be measured at different downstream locations. The wake flow was characterized by using hot-wire anemometer, ultrasonic anemometer measurements, and Particle Image Velocimetry (PIV). The full-scale rotor of 500mm diameter was analyzed as well. The results for velocity deficit and the turbulence intensity were similar for both rotors.

In this sense, the MEXICO experiment[11] was one of the most comprehensive collaborative efforts by the IEA (International Energy Agency), who created the task 29 to gain understanding about wind turbine aerodynamics, as well as to improve aerodynamic models used for wind turbine design. A series of tests for a small wind turbine prototype were performed using the DNW German Dutch open section wind tunnel. Although the rotor wake measurements comprised only the near wake region right behind to the wind turbine (up to 1.5D downstream the rotor), the experiment is a very rich source of data useful to validate wind turbine CFD wake models.

This present work covers the gap of characterizing the wind turbine wake flow field based on experimental data from existing literature, which describes the validation of a wind turbine CFD simulation using velocity wake data from the MEXICO experiment. The

goal is to extend the understanding of the wake flow field beyond the distances analyzed in these experiments, and also analyzing the influence of variable operating conditions on near wake aerodynamic behavior. In order to do so, variable operating conditions with regards to the Tip Speed Ratio (TSR) and the Pitch Angle (Θ) were simulated to understand how these specific design parameters affect the flow field. The second part of this work will extend the analysis beyond the near wake, characterizing the far wake aerodynamic behavior according to the same TSR and Pitch Angle (Θ) conditions.

2.3 Detailed Overview of the MEXICO Experiment

The experiments described in the previous section only performed rotor measurements. However, computational models based on CFD assumptions also need flow field measurements to be successfully validated. The most comprehensive experiment flow field measurement study was the MEXICO (Model Experiments in Controlled Conditions) Experiment[11], which used a rotor prototype of 4.5m diameter and the largest wind tunnel existent in the European continent. PIV techniques were employed to collect flow field measurements around the rotor plane (Fig. 2.1). Several recent studies utilized data from the MEXICO experiment to validate their CFD models [38-54] with different research goals as detailed below.

Figure 2.1 - Sketch showing an overview of the MEXICO Experiment (Top View).Sketch showing an overview of the MEXICO Experiment (Top View).

In regards to Lifting Line codes, Yang[38] showed the necessity for developing new techniques to account for 3D rotational effects on predicting loading for rotors. They created a new technique to determine the angle of attack on rotating blades using data from the MEXICO experiment, a Blade Element Momentum (BEM) code relying on 2D airfoil data was found to over-predict the loading of the rotor; this discrepancy was attributed to the 3D effects originated from the rotor geometry. Xudong[39] developed an aerodynamic/aero-elastic design tool to optimize wind turbine blades and validated the results using MEXICO data for turbine loading.

Regarding the first round of PIV wake measurements (axial flow), Bechmann[40] performed a CFD simulation of the MEXICO rotor using RANS equations further

downstream up to 2.5 diameters behind the rotor. All the simulations were done fully turbulent, but there might be laminar flow at the leading edge of the blades; further work is needed to demonstrate the length of accuracy of laminar turbulent-transition models. Micallef[41] characterized the radial velocities in the near wake close to the MEXICO rotor using a potential-flow panel model to characterize the wake radial induction. Tip vortex characterization performed by tracking its location showed that the radial flow velocity in the rotor plane is not fully dominated by the blade vorticity. Carrión[42] assumed periodic boundary conditions to model only one of the MEXICO rotor blades under axial flow conditions, finding good agreement for the wake flow field by using a compressible multi-block solver without needing to switch between compressible and incompressible flow. Herraez[43] validated a CFD model in OpenFoam using the Spalart-Allmaras turbulence model, showing comparisons for pressure distributions from several blade sections, and PIV near wake measurements. Shen[44] performed CFD simulations of the MEXICO rotor including the geometry of the wind tunnel, and regarding tunnel wall effects this study found that tunnel effects are not significantly influenced by the fluid flow. Garcia[45] developed a hybrid filament-mesh vortex method to improve computational efficiency, using the MEXICO experimental dataset for near wake validation. Nilsson[46] described vortex structures in the near wake of the MEXICO rotor using the actuator line method. The trajectory of the tip vortices and wake expansion were described according to the TSR, implementing a RANS LES model. Wimshurst[47] simulated the near wake flow field of the MEXICO rotor using multiple reference frame approach. The actuator line method using 2D aerodynamic data was compared to a 3D polar actuator line model. Zhong[48] developed a numerical tool combining Lagrangian dynamic large-eddy and actuator line models using

PIV wake data for validation, finding that the tip vortices contribute to a maximum velocity deficit peak and turbulence intensity peak near the blade tip. Guntur[49] developed a full rotor CFD model of the MEXICO rotor focusing on the flow at the inboard part of the blades, analyzing the boundary layer separation at this region to understand differences in behavior between 3D flow and 2D flow. This latter study showed that the fluid flow separation starts at a higher angle of attack for the 3D case.

In regards to the second round of measurements (yawed flow), Sorensen[50] did the first attempts to validate the near wake flow field in yawed flow. Tsalicoglou[51] performed RANS computations of the MEXICO rotor wake for yawed and uniform flow cases, showing that the velocity deficit in the near wake (up to 2 diameters downstream) does not follow a Gaussian distribution. Additionally, the interaction with structures of the wind turbine (nacelle and tower) is more significant for yawed flows. The effects on the wake caused by the tower and the blade could still be observed at the end of the near wake. Grasso[52] showed that the lifting line code coupled with the free wake method can accurately represent the near wake at uniform or yawed conditions. Shen[53] developed an actuator line/Navier-Stokes model using the MEXICO rotor experimental dataset under yawed flow for flow field validation, considering both loading and velocity flow field for the simulation.

2.4 Computational Methods

2.4.1 Rotor Blade Geometry

The MEXICO experiment performed several different flow field measurements to characterize the three-dimensional velocity flow field in the near wake. Experimental measurements such as traverse and longitudinal wind velocity, both upwind and downwind

of the rotor, were performed at a few specific locations. Here, we validated the computational model by plotting the velocity in the wake region of the blade and directly comparing the simulation results with experimental data from the MEXICO rotor. Because our hope is to implement a rapid computational simulation, the objective is to obtain agreement between experimental and computational velocities within 5%. The rotor simulated in this work was the MEXICO Rotor (Fig. 2.2); the three-bladed model has three types of airfoil: DU91-W2-250 (20% to 45%), Riso-A1-21 (54% to 65%), and NACA 64-418 (75% until the blade tip). The blade is also twisted, and a pitch angle of -2.3° was applied for the measurements. The blade geometry can be found in the final report of this experiment[11]. Since some of the airfoil data are not publicly available, a reverse engineering process was performed to find the airfoil coordinates.

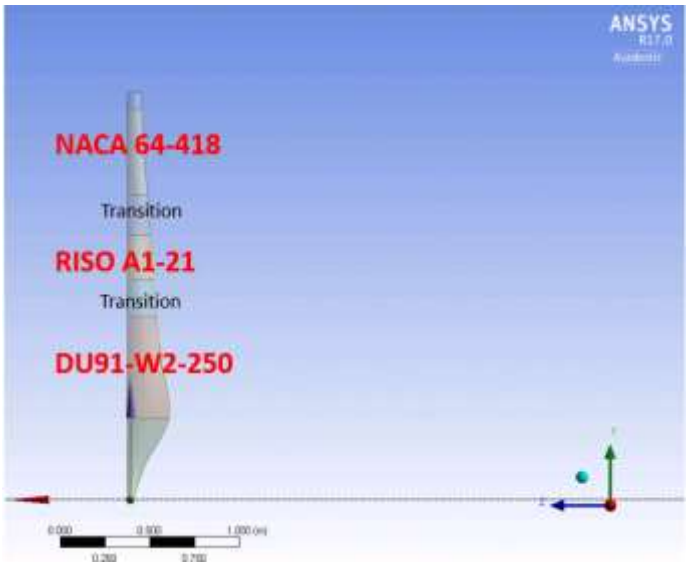

Figure 2.2 - MEXICO rotor geometry, a three-bladed rotor with 4.5m diameter. Source for the blade geometry: Scheppers et al[11].

2.4.2 Layout and Boundary Conditions

We broke down the computational domain into smaller parts for two reasons. First, local mesh sizing: the meaningful region can be refined to correctly characterize the flow field. Second, pressure-far-field boundary conditions for the lateral and superior boundaries require a larger domain to keep straight streamlines at the boundaries to achieve numerical convergence. The dimensions of the square part containing the wind tunnel and the rotor extends from -1D to 1D, while the exterior part corresponding to the surroundings extends from -10D to 10D.

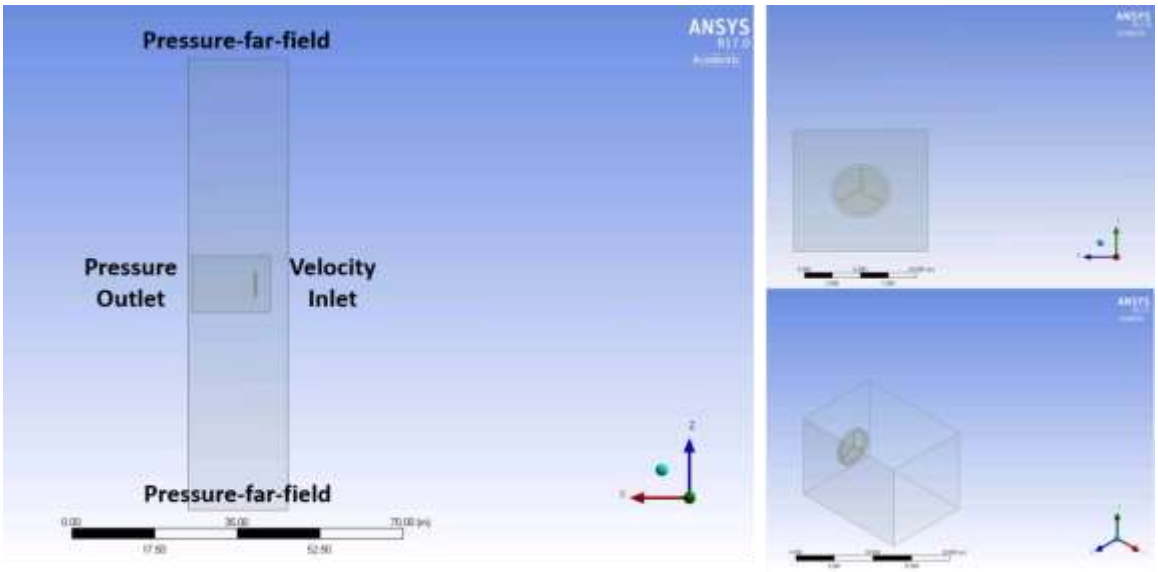

Figure 2.3 – Layout of the computational domain and boundary conditions.

2.4.3 Computational Fluid Dynamics Modeling

CFD assumptions are based on the Finite Volume Method (FVM) for representing and evaluating partial differential equations in the form of algebraic equations. The domain of interest is divided into small cells, reducing the Navier-Stokes equations to algebraic or simple differential equation. Integration of the volume is conducted to obtain surface fluxes

because the flux entering a given volume is identical to that leaving the adjacent volume. The CFD solver implemented in this work was ANSYS Fluent 17, housed in two computers, each with 64GB RAM/ 8 processes with the processor Intel Xeon CPU E5-1620 v2 3.7GHz. The computational time for each simulation was approximately 10 hours. The simulation was performed using a steady state Moving Reference Frame approach, and setting the rotational speed to match experimental conditions. The turbulence model selected was the k-ω SST, which is suitable for swirl flow, and it was used in the literature studies as their main turbulence modelling technique. Pressure-far-field boundaries are applied for the lateral and superior boundaries, pressure-outlet for the exit, velocity-inlet for the front boundary, and a special type of wall with no shear for the inferior boundary (Fig. 2.3). Different operating conditions were tested in this experiment, and some of them were mimicked in this computational study for the validation: ω=424.5rpm, U=15m.s^{-1} (which results in a TSR=λ=6.6), and U=10m.s-1 (TSR=10). Additionally, several other operating conditions regarding Free-Stream Velocity, TSR and Pitch Angle were simulated to characterize the wake aerodynamic behavior.

The physical domain was meshed using unstructured elements (Fig. 2.4), which are suitable for CFD applications because of its good convergence rate. After doing a mesh sensitivity study, a total of approximately 10 million cell elements was found to be sufficient to accurately validate the model and describe the near wake. A mesh sensitivity study is presented at the Appendix D confirming the need for 10 million cells to accurately validate the model. The meshing process consisted of a sphere of influence with 0.1m cell elements in a radial distance of 6 meters surrounding the rotor, and a square part extending from -0.5D to 3D with 0.15m cell elements. The blade surface mesh was dimensioned

using local edge sizing to reduce the skewness of the cells, resulting in 175 nodes spanwise and 75 nodes chordwise at the blade tip. Additionally, 10 inflation layers with a ratio of 1.1 were built to ensure y+<1 next to the blade surface. The physical domain needs to be large enough to result in a good simulation convergence, since pressure-far-field boundaries (lateral boundaries) require straight streamlines to avoid divergence for the residuals. However, the mesh at the exterior part surrounding the wind turbine and the rotor domain is coarse, since this region is not meaningful for the CFD aerodynamics analysis.

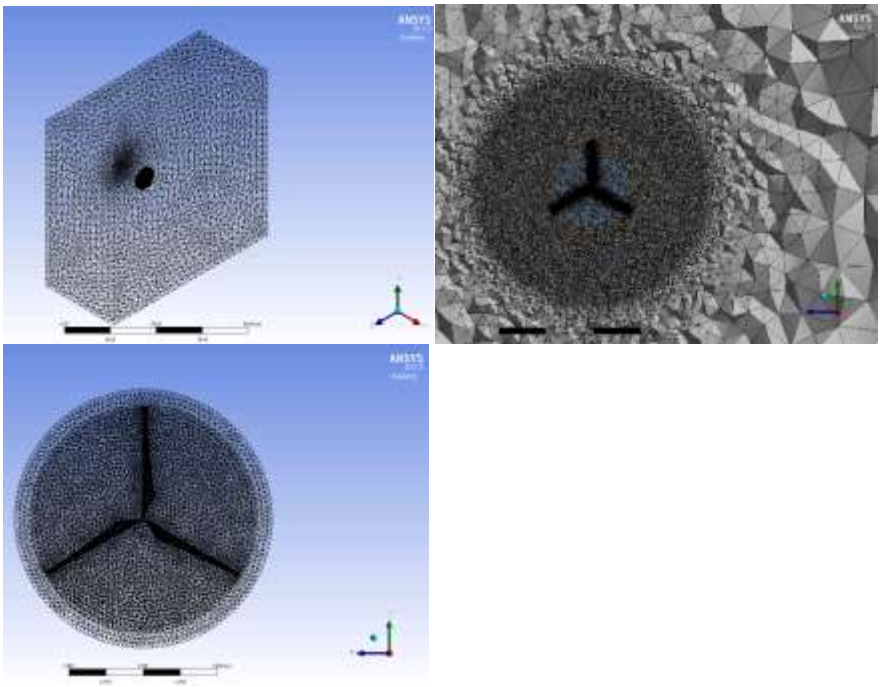

Figure 2.4 – Mesh of the Computational Domain. a) Computational Domain. b) Details of the Sphere of influence for Meshing. c) Sectional plane showing details of the rotative central disc.

2.4.4 Tip Speed Ratio Effect on the Near Wake

A very important design parameter for wind farms is the Tip Speed Ratio (TSR), which is defined as the ratio between the blade tip speed velocity and the free-stream

velocity (Equation 1). The TSR and other parameters such as free-stream velocity are critical to determine the wake behavior.

$$\lambda = \frac{\omega \cdot R}{U_{freestream}} \tag{2.1}$$

Where ω is the rotor rotational speed, R is the blade radius and U is the free stream velocity.

Another important design parameter is the Turbulence Intensity (TI). This parameter can be calculated using the Equation (2):

$$TI = \frac{\sigma_U}{U_{freestream}} \tag{2.2}$$

Where σ_U is the velocity standard deviation.

2.4.5 Wake Validation

The flow field at the wake of the rotor is validated by comparison between experimental[11] and computational data from the CFD simulation. The axial and radial traverses at the wake described in the section 2.3 (Fig. 2.1) are considered for the validation.

2.5 Results and Discussion

2.5.1 Validation Dataset

Fig. 2.5 shows the axial and radial traverses considering the free stream velocity=15m/s and at one radial and one axial downstream positions: R=1.8m and x=0.3m. The computational results match the experimental data very well for R=1.8m (Fig.

2.5), and almost entirely match the radial traverse at x=0.3m (Fig. 2.5). This demonstrates that this CFD model can accurately reflect the real rotor behavior. Fig. 2.6 shows the validation for the radial traverse at 0.3m downstream of the rotor, while considering free stream velocity of 15m/s. The computational results qualitatively agree with the experimental results; however, there are minor numerical discrepancies (Fig. 2.6). Even though the velocity values do not completely overlap, the shape of the computational curve is very similar to the shape of the curve obtained with the experimental procedure (Fig. 2.6). A possible explanation for the minor discrepancies comes from the Moving Reference Frame approach utilized in the numerical method applied here, which assumes steady state behavior. This means that the Navier-Stokes equations are averaged by the Reynolds number (RANS). In spite of that, the simulation is suitable to determine how design parameters (such as TSR, velocity and pitch angle) affect the wake aerodynamic behavior. Discrepancies between experimental and computational data were also verified in other studies. First of all, the type of experiment apparently plays an important role in regards to the discrepancies. Particle image velocimetry (PIV) is a technique very sensitive to experimental conditions. In the case of the MEXICO experiment, the light path close to the hub of the wind turbine can potentially disturb and induce the oscillations in the velocity profile observed in the traverse at R=1.4m. The problem with light reflection caused by the blade or the nacelle was also described by Carrion[42], however the numerical discrepancies found in this study could be related to numerical reasons. Wimshurst[47] mentioned that the upstream axial free-stream velocity is lower in the MEXICO experiment than the computational simulation, arguing that the open tunnel configuration caused expansion of the streamtube between the wind tunnel nozzle and the collector, consequently causing

smaller axial induction downstream of the rotor. The computed axial velocity was lower than the experimental axial velocity, which was explained by the greater force applied to the flow by the rotor. Shen[44] observed that the computed axial free-stream velocity upstream of the rotor was 2.5% lower than the experimental ($15m.s^{-1}$), and the discrepancies in the near wake were attributed to smaller thrust prediction. A potential contribution to discrepancies is attributed to the type of experiment (PIV measurements), which does instantaneous measurements containing fluctuations. Additionally, the wake fluctuation caused by the tip vortex could not be captured by the computational physical model employed in that study. The type of mesh refinement from Shen's study was claimed to be dependent on the upstream velocity, where a coarse mesh causes excessive dissipation. The sudden drop in velocity for the radial traverse at x=0.3m was attributed to the vortex shedding from the transition between the airfoils DU and Riso, and the intensity of the vortex was related to the change of circulation on the blade. Nilsson[46] attributed the slightly overestimated axial velocity to the thrust, which was underestimated for all flow configurations. Furthermore, the light in the tunnel might have reflected on the turbine hub, affecting the experimental PIV measurements at the blade inboard radial position 0.52R (closer to the hub). Garcia[45] found underprediction of the thrust close to the blade root, attributed to rotational Coriolis effects and centrifugal forces in the boundary layer. Sorensen[50] found that the size of the nacelle influenced the inboard blade flow for yawed cases, so that the nacelle must also be included for accurate CFD modeling at the inboard region.

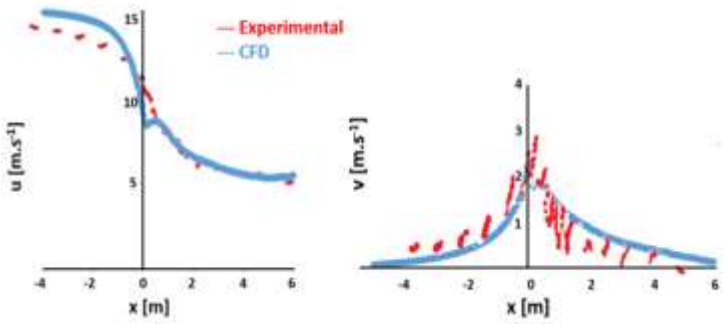

Figure 2.5 – Validation dataset for an axial traverse at R=1.8m and a radial traverse at x=0.30m, showing comparison between computational and experimental data for U=15m.s-1.

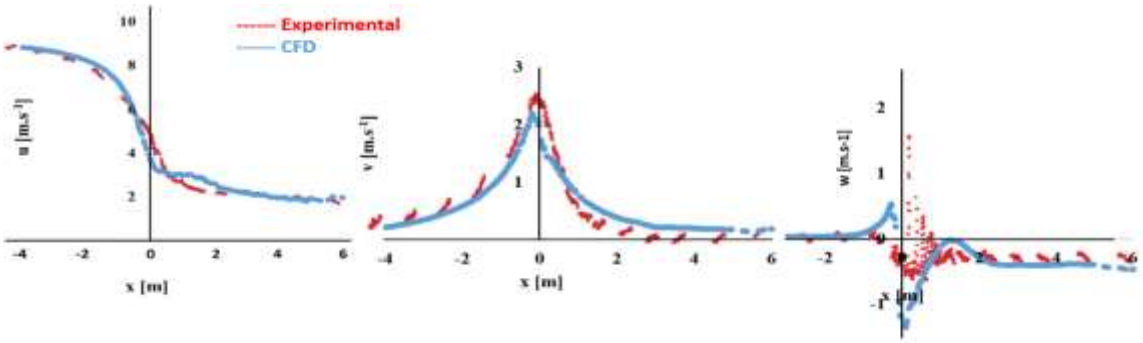

Figure 2.6 – Validation of the axial traverse at R=1.8m and radial traverse at x=0.30m showing comparison between computational and experimental data for U=10m.s-1.

2.5.2 Tip Speed Ratio (λ) Effect on the Near Wake

2.5.2.1 Velocity Profile at the Near Wake

The near wake aerodynamic behavior is dependent on the rotor loading, which is dependent on the TSR. The rotor loading increases as the TSR increases, leading to an increase of the velocity deficit at the wake. Fig. 2.7 shows the streamwise velocity-deficit evolution at five downstream positions in intervals of 0.5D, under different loading (or TSR) and upstream velocity conditions. The x-axis shows a radial traverse downstream of

the rotor, while the y-axis shows the velocity at the wake. First of all, the axial induction increases as the rotor loading/TSR increases. As a consequence, the velocity deficit in the near wake increases as the rotor loading (or TSR) increases. A TSR=6.6 results in a higher rotor loading and more produced power compared to a TSR=4, thus extracting more energy from the incident wind. The shape of the curves with the same TSR is very similar, regardless of the incident upstream velocity. For a TSR=6.6 and U=10m.s^{-1} (Fig.2.7), the velocity increases from approximately 4m/s at 1D downstream of the rotor to 7m/s at 3D downstream of the rotor, showing an increased rate of 1.5m/s for each diameter or 15% of the free-stream velocity per rotor diameter at the wake. From the perspective of the same analysis, but considering the case of TSR=6.6 and U=15m.s^{-1}, the velocity increases from approximately 6m/s at 1D downstream of the rotor to approximately 11m/s at 3D downstream of the rotor. This corresponds to an increased ratio of 2.5m.s^{-1} for each rotor diameter or approximately 15% of the free-stream velocity per rotor diameter at the wake. Moreover, the radial traverse right behind the rotor in Fig.2.8 shows an increase of 20% in the velocity deficit as the TSR varies from 6 to 10, corresponding to an increased ratio of approximately 5% m.s^{-1} per dimensionless unit of TSR. Our work, unlike previous efforts in literature, simulated the near wake of the MEXICO rotor within an extended downstream region including 3 diameters, while considering other TSR and free-stream velocity operating conditions. The same trend between axial induction and rotor loading was observed in other studies[37, 40], in which the axial induction significantly increased from TSR=4.2 to TSR=10. Furthermore, the rotor loading influences the shape of the velocity profile at several downstream positions (Fig.2.7). While little perturbation to the velocity curves is observed for lower rotor loading, unsteady behavior/oscillation is present for

higher rotor loading. The dependence of the velocity deficit on the streamwise distance is clearly more significant for higher TSR. These results agree with other studies in literature[55]. Fig. 2.8 shows the radial traverse in the wake immediately behind the MEXICO rotor at x=0.3m, confirming the trend between loading and velocity deficit, even immediately adjacent to the rotor. Moreover, the tip vortices cause the region close to the blade tip to present the highest velocity deficit in comparison to the other blade radial locations; this will determine the wake expansion. Tari[56] also found that the axial induction of horizontal axis wind turbines increases with the TSR, in which a maximum axial velocity deficit occurs between $0.75 < r/R < 0.9$.

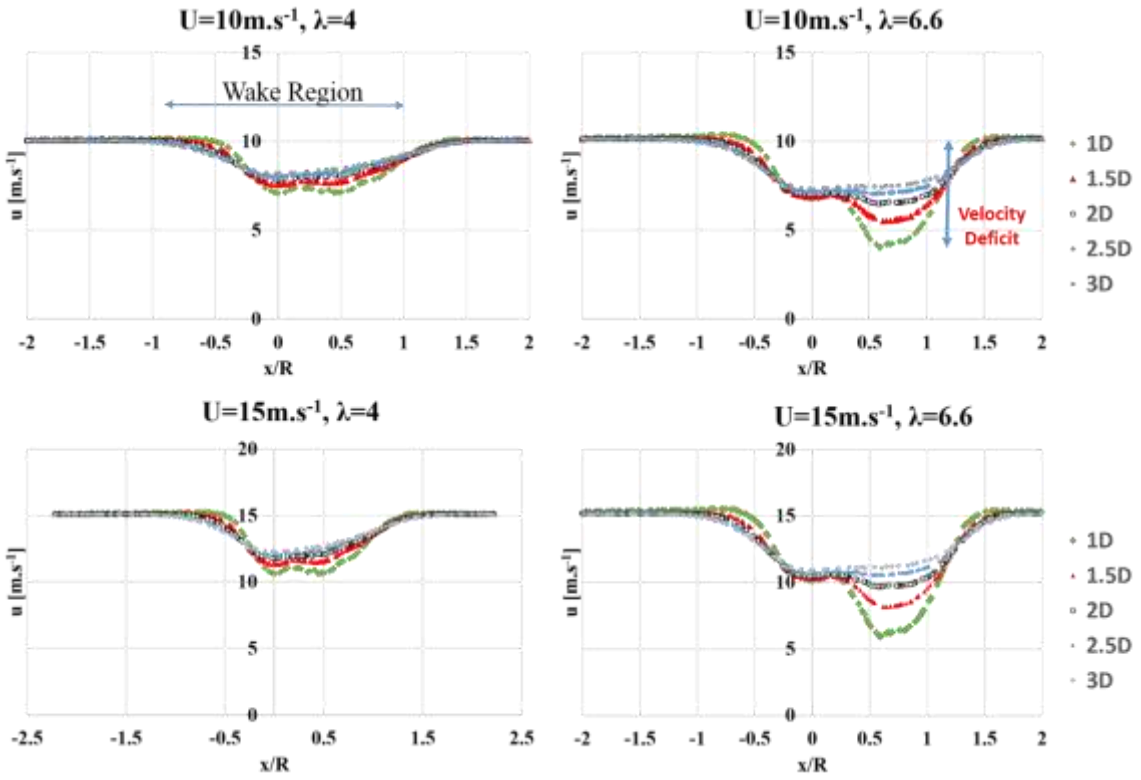

Figure 2.7 – Wake development for two different velocity and TSR (λ) values.

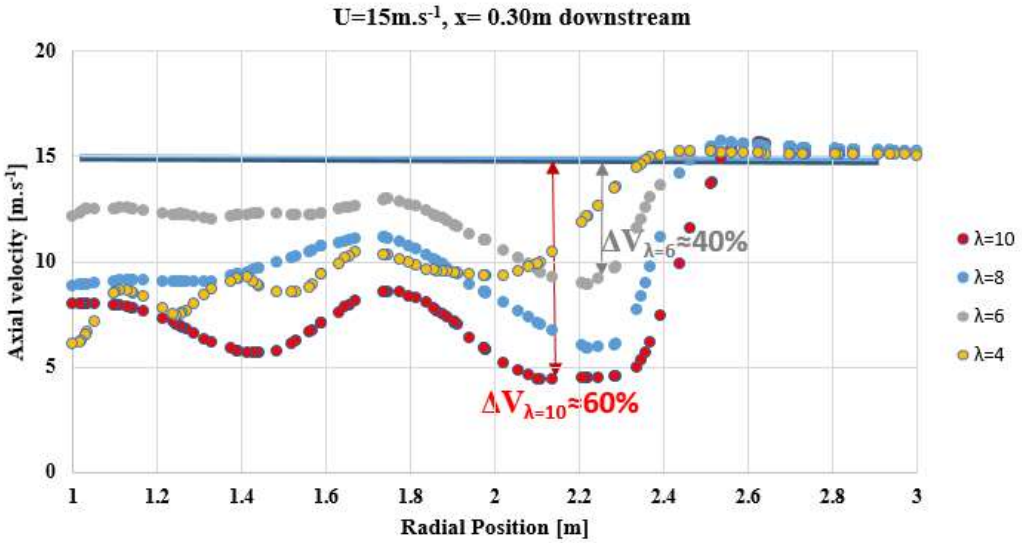

Figure 2.8 - Axial Velocity profile for a radial traverse, and several TSR values.

2.5.2.2 Turbulence Intensity Profile at the Near Wake

Fig.2.9 shows a plot of the TI profile in the y-axis as a function of the radial position in the x-axis, for three free-stream velocity values. The first thing to notice is that the TI profile is relatively more symmetric in comparison to the velocity profile, especially for the downstream positions corresponding to 2D and 3D. Moreover, the TI reaches a maximum peak at a location right behind the rotor in the wake at 1D, decreasing through the wake for the subsequent radial positions of 2D and 3D (Fig. 2.9). This trend is observed for all the three free-stream velocities analyzed in this work. Additionally, when comparing the TI profile between 1D and 2D/3D it is also possible to see the wake expansion effects as the fluid flow develops in the wake: the shape of the curves is slightly tighter for 1D than for 2D or 3D. Furthermore, the TI peak increases as the free-stream velocity increases. When considering a downstream position of 1D (Fig. 2.9b): the TI reaches a maximum value of 0.35 for U=10m.s^{-1}, while TI reaches a maximum peak of 0.65 for U=15m.s^{-1}, and

finally TI reaches 0.90 maximum peak for U=24m.s^{-1}. This shows that there is a dependence of the TI behavior according to the free-stream velocity, and the same trend can be extended to the downstream positions of 2D (Fig. 2.9d) and 3D (Fig. 2.9f). The TI aerodynamic behavior in the near and far wake was also characterized in previous studies. For instance, Shives[57] found that the oscillating /fluctuating behavior is less significant for x/D>5 in comparison to the near wake, and the curve shape becomes more similar to a Gaussian distribution. This trend was different in comparison to the velocity curve behavior, where the velocity curve starts to define its shape at x/D>3. Chamorro[58] investigated the effect of the Reynolds number on the wake characteristics, finding that the TI profile in the near wake is dependent on the Reynolds number, and independent at approximately x/d=4. It is pointed that the non-uniformity of the boundary layer influences the TI profiles to present relatively asymmetric distribution, which could also explain the asymmetric shape of the velocity profile. Additionally, the effect of the TI could still be observed even up to 12 rotor diameters downstream. Xie[59] found that the streamwise component of the Turbulence Kinetic Energy (TKE) is dominant for horizontal axis wind turbines. Turbulence Intensity contours showed that the streamwise component of the TI reaches a maximum at 5D, which extends up to approximately 15D, when it starts decaying. A low TI region happens immediately behind the rotor, which contradicts the TI trend behavior found in our study (Fig. 2.9). Zhou[60] investigated the influence of the inflow characteristics on the near wake of the NREL Phase IV, finding that the combination of inflow turbulence and wind shear can also have an impact on the turbulence generation in the near wake. Fig. 2.10 shows plots for the TKE as a function of the velocity and downstream distances (in rotor diameters) in the near wake. The TKE has some

components: the advection by the mean flow, the transport by the vorticity, the TKE production, and the TKE dissipation. The TKE presents a similar trend observed in the TI, where the near wake immediately next to the rotor at 1D presents the TKE peak for all the velocities.

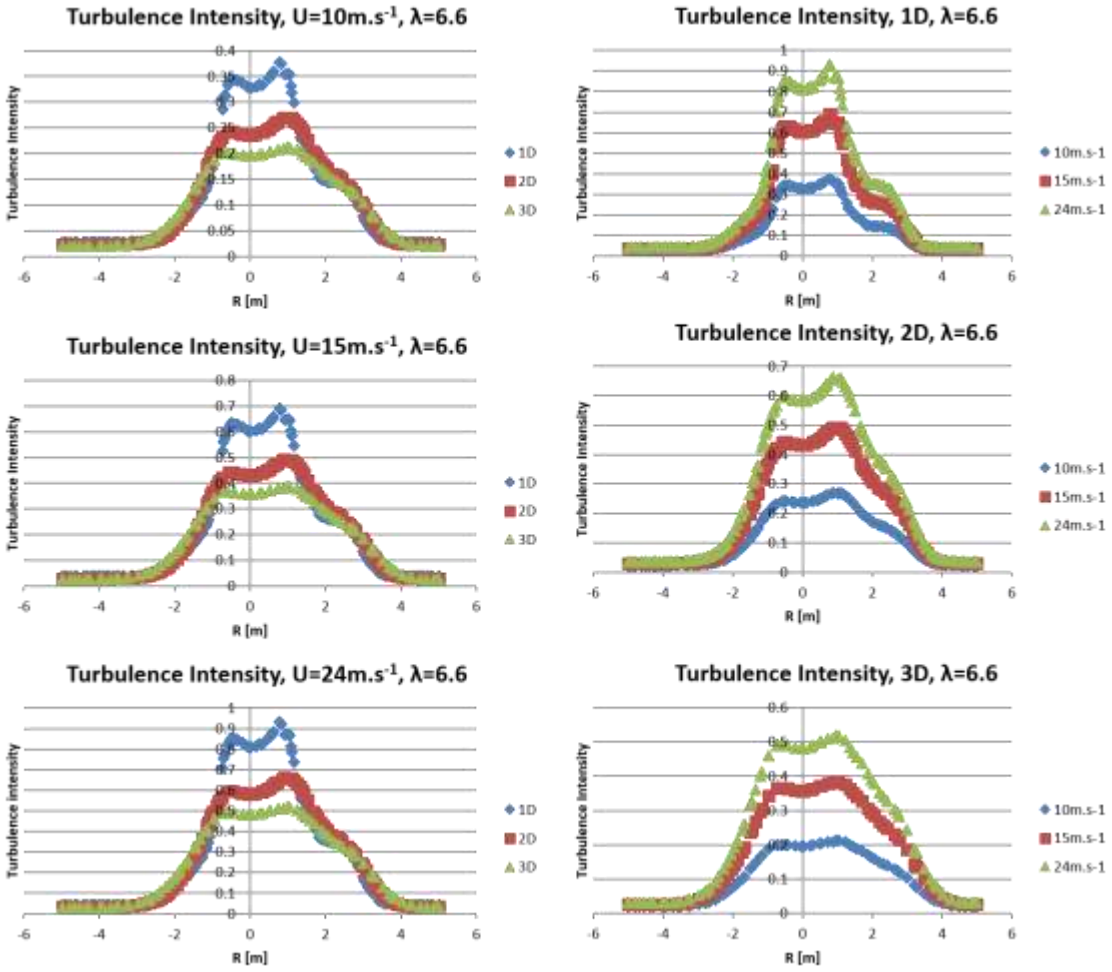

Figure 2.9 – Turbulence Intensity as a function of Velocity and TSR.

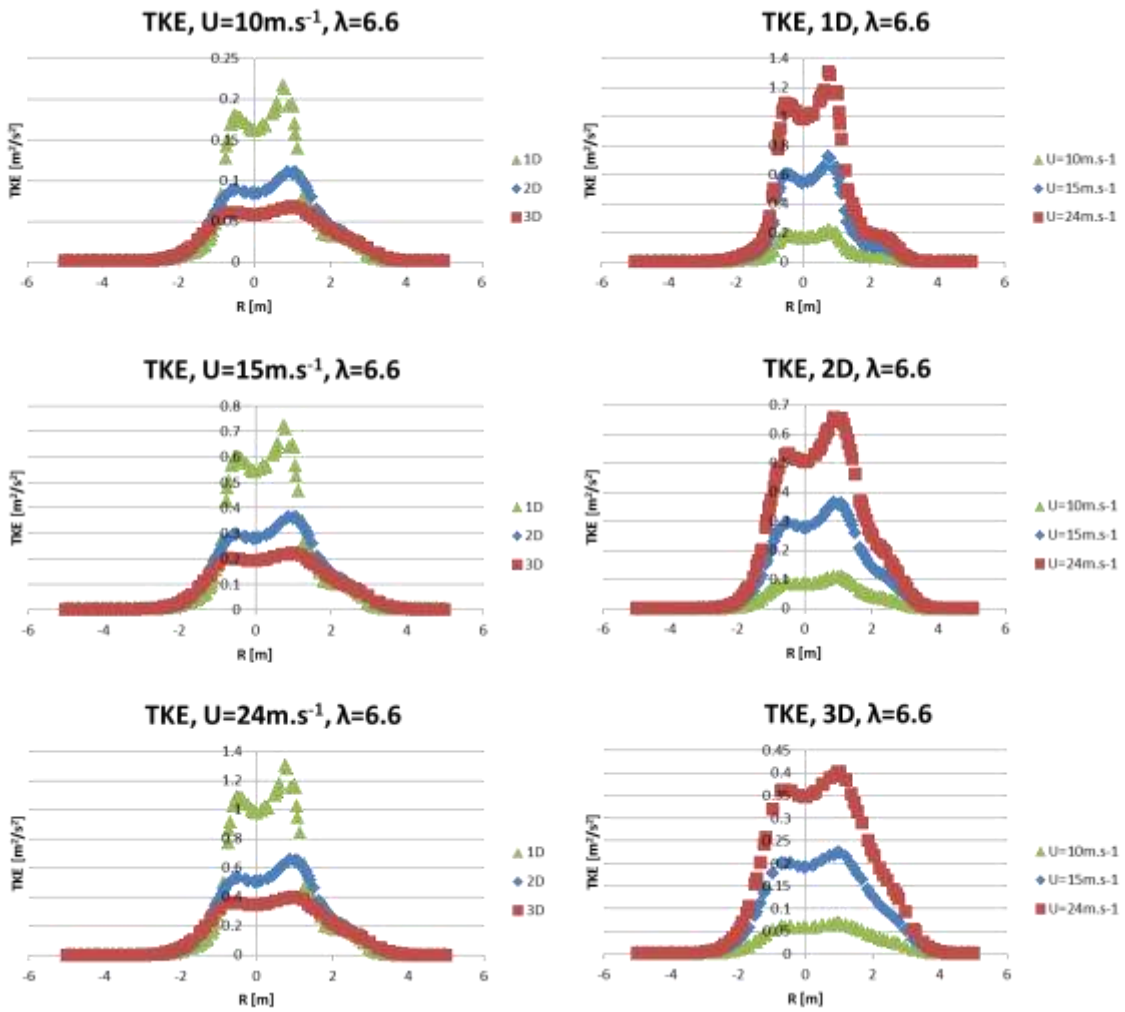

Figure 2.10 – Turbulence Kinetic Energy as a function of Velocity and downstream distances in the near wake.

2.5.2.3 Pitch Angle (θ) Effect on the Near Wake

The Pitch Angle (Θ) influences the near wake development in regards to the velocity deficit (Fig. 2.11). The rotor design process aims to deliver the best aerodynamic performance according to the blade geometry (chord length, airfoil, rotor diameter), and a specific set of operating conditions. It is important to point out that the designed pitch angle for the MEXICO rotor blade is Θ=-2.3°, corresponding to a TSR of λ=6.6 for U=15m.s^{-1}

and ω=424.5rpm. The pitch angle Θ can significantly influence the near wake aerodynamic behavior. However, the far wake will likely not be affected if the pitch angle is close to the designed condition. As can be seen by the axial velocity behavior (Fig. 2.11), the velocity deficit is greater for negative pitch angle values than for positive values. This happens because in the case of the MEXICO rotor, negative pitch angle values are closer to the designed condition, thus extracting more energy from the incident wind. Consequently, the axial induction is greater for those pitch angle values close to the designed condition. Additionally, the velocity deficit increases as the pitch angle becomes more negative. This can be verified in Fig. 2.11, where a pitch angle of -1° resulted in a smaller velocity deficit in comparison to a pitch angle of -2.3° or -3°. Since the pitch angle is proven to have impact on wind farms and wind many researchers. Markou[61] showed that individual-pitch controllers allowed fatigue load reductions for offshore applications, while not significantly influencing the far wake behavior. Tests for a wake compensator resulted in a minimal reduction in average output power of 0.05% for 10D downstream distance. Kanev[62] showed the benefits of using a pitch-based system for wind farms with turbine distances from 6D to 7D, in which 1% to 4% of the wake losses were regained yearly. Additionally, a lifetime extension of 1% was achieved by reducing fatigue loads. Kanev[62] found that turbines, the influence of the pitch angle in wakes and aerodynamic performance has been studied by the wake loss reduction was unresponsive to a particular farm layout. Moreover, higher benefits could be achieved by combining pitch-based and yaw-based wind direction wise systems. In this case, a pitch-based system would be operated for wind directions well-aligned with the rows of turbines, while the yaw system would act as the wind comes at an angle in respect to the rows. Symmetrical layouts combining both

systems could approximate the sum of the power production benefits of the two separate strategies.

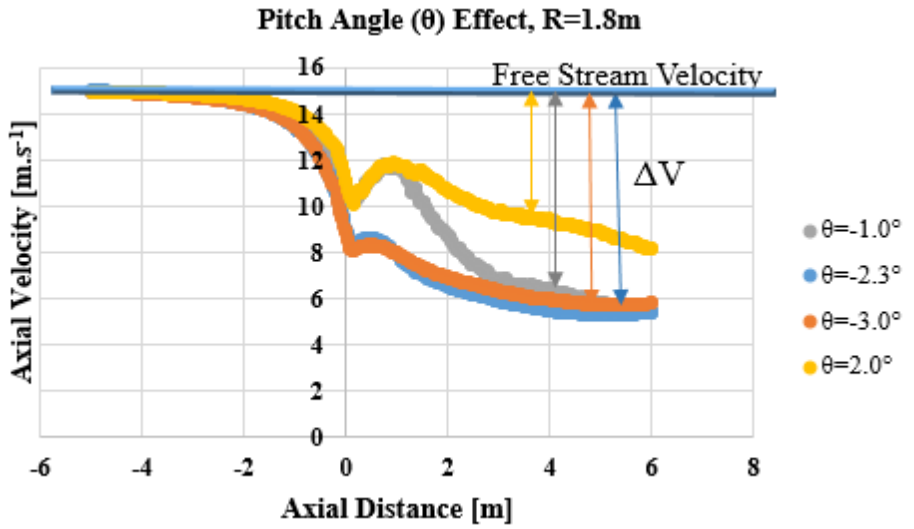

Figure 2.11 – Influence of the pitch angle (Θ) in the wake. The designed pitch angle is Θ=-2.3°.

2.6 Conclusions

In this present work, a computational system was designed to analyze and optimize the operational conditions of a wind turbine and the flow field surrounding the rotor wake region. This work is intended to establish a computational framework from which to investigate wind farm layout, and to validate the simulation and identify parameters influencing the wake. The computational results match the selected experimental data for the radial and axial traverse in axial flow conditions. Even though there are minor numerical discrepancies, this CFD model is suitable to determine how design parameters (such as TSR, velocity, and pitch angle) affect the wake aerodynamic behavior. The level of agreement is very similar in comparison to those found in literature.

CFD simulation demonstrates that the TSR and the pitch angle greatly influence the near wake behavior, affecting the velocity deficit and the turbulence intensity profile in this region. In the near wake region, the velocity deficit increases as the TSR increases, revealing an increase of 20% in the velocity deficit as the TSR varies from 6 to 10. This corresponds to an increased ratio of approximately 5% $m.s^{-1}$ per dimensionless unit of TSR. The velocity in the wake increases at a rate of approximately 15% of the free-stream velocity per rotor diameter at the wake, regardless of the free-stream velocity applied. The TI peak increases as the free-stream velocity increases. Considering TSR=6.6, a downstream position at 1D behind the rotor shows an increase of around 85% in the TI peak from U=10$m.s^{-1}$ to U=15$m.s^{-1}$, and 40% from U=15m.s-1 to U=24m.s-1. This shows that there is a dependence of the TI behavior according to the free-stream velocity. The Pitch Angle can significantly influence the near wake aerodynamic behavior; however, the far wake will not be affected if the pitch angle is close to the designed condition. Wake characteristics such as velocity deficit and TI could also be affected by the pitch angle, the TSR, and at further downstream distances. Our results give support to the notion that the far wake analysis is extremely relevant for the optimal positioning of wind turbines in a wind farm.

Chapter 3: Development of a Computational System to Optimize Wind Farm Layout, Part II: Far Wake CFD Analysis.

Abstract

This work describes a wind turbine CFD (Computational Fluid Dynamics) simulation, including the far wake modeling and analysis. The work is intended to establish a computational framework from which to investigate wind farm layout. In the first part of this research, a CFD model was designed to mimic the same experimental conditions of the MEXICO experiment for the near wake, and simulate new operating conditions with regards to tip speed ratio and pitch angle. The second part of this work seeks to verify the accuracy of the simulation compared to kinematic models, field data and previous computational models from literature. The wake analysis is extended beyond the distances and operating range found in literature. Results demonstrated that velocity deficit and the turbulence intensity in the near wake is strongly influenced by the tip speed ratio and the pitch angle. Considering the case corresponding to the designed tip speed ratio of TSR=6.6, the velocity in the wake increases at a rate of approximately 15% of the free-stream velocity per rotor diameter at the wake regardless the free-stream velocity applied. Moreover, analysis of a radial traverse right behind the rotor showed an increase of 20% in the velocity deficit as the TSR varies from TSR=6 to TSR=10, corresponding to an increase ratio of approximately 5% m/s per dimensionless unit of TSR. The Turbulence Intensity peak

increases as the free-stream velocity increases: the TI reaches a maximum of 0.9 for $U=24m.s^{-1}$ for a downstream position of 1D, while TI reaches 0.65 maximum peak for $U=15m.s^{-1}$, and finally TI reaches 0.35 maximum peak for $U=10m.s^{-1}$. This shows that there is a dependence of the TI behavior according to the free-stream velocity. The Pitch Angle can significantly influence the near wake aerodynamic behavior; however the far wake will not be affected if the pitch angle is close to the designed condition.

3.1 Introduction

The necessity for improving wake models has become more apparent over the last decade with the continuous growth of the wind energy market. Literature shows several analytical wake models: Infinite Wind Farm Boundary Layer model, Jensen Wake model, Larsen model, Dynamic Wake Meandering model, FUGA, Ellypsys3D. All these models are excellent tools to estimate wake effects, but there is still room for improvement. Usually, analytical models do not consider wake characteristics according to variable operating conditions. However, Computational Fluid Dynamics (CFD) models have the capabilities to model wake velocity deficit and Turbulence Intensity (TI) according to variable operating conditions. Although computationally expensive, CFD models are powerful tools that can be applied to solve some of the most complex problems in engineering. The chapter 2 of this dissertation described how operational parameters affect the near wake aerodynamic behavior of a wind turbine. This chapter now proposes a CFD model to characterize three-dimensional far wake effects, and numerically quantify the influence of some important wind farm design parameters on the far wake aerodynamic behavior. Literature shows that there is a gap in attempting to solve the Wind Farm Layout Optimization Problem (WFLOP) while still considering a rigorous evaluation of the wake

effects. The objective of this work is to develop a CFD model with such capabilities, applicable for future applications related to the WFLOP.

3.2 Review: Wind Farm Aerodynamics

3.2.1 Wake Aerodynamics

Wake models are usually divided in literature [3, 63, 64, and 65] in two categories: 1) analytical/empirical/explicit wake models; 2) computational/implicit wake models. The analytical models solve a set of equations based on conservation of mass and empirical relations of wake decay, characterizing the energy content in the flow field and ignoring the details of the exact nature of the flow field. Kinematic Models such as Jensen, Larsen, and Frandsen´s model assume self-similar velocity deficit profiles, not solving turbulence field but only the momentum equation[63.] The velocity deficit is derived from global momentum conversation, using thrust coefficient of the turbine as an input[3]. The computational models solve the fluid flow equations for the wake velocity and turbulence field, whether simplified or not [63].

3.2.2 Wind Energy CFD Review

Although there are many CFD studies in literature approaching wind energy, this is a field of study still in development. CFD modeling techniques applicable for wind turbines significantly vary in literature, showing that there is no well-stablished standard approach. This section presents a comprehensive literature review in CFD models applicable to wind energy, providing an overview about what have been done prior to this work. In regards to CFD techniques for modeling wind turbine flow field, the goal is to investigate what possibilities have not been explored yet, seeking to develop a novel wind turbine CFD model capable of evaluating far wake aerodynamics characteristics. As

previously mentioned, a correct evaluation of such characteristics can help to achieve better solutions for the WFLOP.

3.2.2.1 NREL Phase VI

Several studies utilized the NREL/NASA AMMES Phase VI experimental data campaign to validate their computational models, all of them using pressure coefficient on the blades and aerodynamic torque data for comparison. However, it is difficult to validate wake flow field since no wake measurements were performed in these experiments. Zhou et al.[33] performed LES (Large-Eddy Simulation) of the NREL phase VI, evaluating the effect of different inflow conditions (using user-defined-functions) on the aerodynamic loading and near wake characteristics. A structured multi-block mesh (with sliding mesh zone) was implemented with refinement on leading and trailing edges. They found that the wind shear and turbulence effects destroyed the uniform and symmetric wake profile in the far wake. Hsu[34] validated a finite-element (Lagrangian-Eulerian) model of the NREL Phase VI using a non-structured rotating mesh. Wake characterization was not the focus of the study, which explains the wake made out of coarse non-structured cells with no refinement. Gundling[35] evaluated low and high fidelity models using the NREL Phase VI for predicting wind turbine performance, aeroelastic behavior and wakes: 1) the Blade Element method with a free-vortex wake; 2) the Actuator Disc method (AD); 3) the Full-Rotor method (FR). No specific information or sketch of the wake was provided or described. The full rotor method showed the largest wind deficits and the slowest dissipation rate for the far wake. Mo[36] developed a study in more depth to understand wake aerodynamics performing a LES of the NREL Phase VI using the Dynamic Smagorinsky model; additionally, verification of the average Turbulence Intensity was performed

against an analytical model. They found that the downstream distance where instability and vortex breakdowns occur is dependent on wind free-stream inlet conditions: 7m/s happens at 4 rotor diameters, while 15.1m/s between 11 and 13 diameters. A decrease of the turbulence intensity happened after instability and vortex breakdowns. The strategy for meshing the physical domain consisted of a virtual wind tunnel with the same dimensions of the NASA AMES; the rotor located at 2 diameters downstream of the inlet with a downstream domain of 20 rotor diameters in length. Choudhry[37] performed a very similar CFD study of the NREL phase VI using the same computational methods of the study conducted by Mo[36], finding that regions of velocity deficit and high turbulence intensity are within the high vorticity region. Choudry's study did not specify if the mesh is structured or unstructured.

3.2.2.2 NREL 5MW

Many studies have developed CFD models considering the NREL 5MW wind turbine. Among these studies, Troldborg et al[66] developed a wake CFD (Ellypsys3D) study for the NREL 5MW considering three different models: 1) a fully resolved rotor geometry; 2) AL method; and 3) AD method. A comparison for wake properties in uniform and turbulent inflows was performed. All the models correctly predict mean axial velocity within 4 radii downstream of the turbine for laminar inflow. The agreement between AD and AL methods is acceptable for the wake deficit. They found that the AD/ AL model is sufficient to simulate turbines under atmospheric boundary layer conditions. Storey et al.[67] implemented a CFD model using a modified actuator technique to develop transient simulations, considering the NREL 5MW turbine. They achieved reduction in the computational time for the simulation while still keeping flow solution fidelity compared

to the standard actuator disc model. Seydel et al[68] performed a RANS k-ω simulation of the NREL 5MW to study wake effects between two wind turbines. Réthoré et al[69] investigated CFD techniques based on permeable body forces including: AD, AL and the Actuator Surface (AS). These approaches can potentially reduce the necessity for mesh refinement next to the rotor. Verification for the AD in comparison with analytical solution for heavily loaded turbines demonstrated that the actuator disc can be a cost-effective way to model wind turbine wake. The verification of the actuator disc model showed that 10 cells per diameter are adequate to describe the near wake flow characteristics, and the cell size becomes less critical in the far wake. The computational domain extends 10 diameters laterally and 25 diameters horizontally, and the wake computational grid is uniformly spaced with cells of the same size. Heinz et al[70] developed a fluid-structure interaction simulation using EllipSys3D and aero-elastic HAWC2 for the NREL 5MW considering yaw and standard conditions. Miao et al[71] developed an unsteady CFD (STAR-CCM+) model for the NREL 5MW rotor considering yawed flow to investigate wake deviation. The full rotor geometry was modeled considering the 5MW NREL wind turbine, under neutral atmospheric boundary layer conditions. Wilson et al[72] developed a CFD model based on the RANS (OpenFoam and ANSYS Fluent) equations, considering k-ε and k-ω SST turbulence model to investigate interactions between wind turbines in neutral atmospheric boundary layer conditions. The AD, the AL, and the FR models were compared considering the NREL 5MW. Weipao et al[73] considered the tilt and cone angle to maximize the power generation of a wind farm for the NREL 5MW.

3.2.2.3 Floating Offshore

CFD modeling techniques have been applied for designing and analysis of floating offshore wind farms. Wu et al[74] developed a CFD for offshore floating wind turbine. The near-wake domain is defined as 3D downstream, whereas a 0.5D distance upstream of the rotor is maintained with a constant size mesh cells. Two different approaches for blade meshing were implemented: unstructured tetrahedral and unstructured hexahedral. Theunissen et al[75] developed a computational and experimental study to optimize the layout of an offshore wind farm array with 80 turbines. Tran et al[76] developed an unsteady CFD model for a floating offshore, using the software FAST and Unsteady BEM equations for the analysis.

3.2.2.4 Other Topics

In regards to other topics within wind turbine CFD modeling, Zhale et al.[77] performed unsteady yaw description for a 500kW rotor modeling the RANS equations using Ellipsys3D. A pressure-based incompressible flow was setup, considering an iterative SIMPLE and PISO second-order accurate scheme, the turbulence k – ω SST model (good performance for wall-bounded adverse pressure gradient flows). The computational mesh was generated using the software (Gridgen) with structured elements. Aschulz et al.[78] performed a CFD (FLOWer) study of the yaw flow (-50° to +50°) on a generic 2.4MW using Detached Eddy Simulation (DES). Sarmast et al[79] developed an actuator line model using new vortex code on the Biot-Savart law, and considering two different wind turbines: constant and variable circulation along the blades. They concluded that a simplex vortex code has similar results to the actuator line, and a lower computational cost. Prospathopoulos et al[80] developed a RANS k-ω model modified for atmospheric

flows, finding that CFD models underestimate near wake deficit even for single-wind turbine wake predictions specially under neutral atmospheric conditions. The accuracy was better for the far wake, and this study also considered the multi-wake interaction considering the case of five turbines in a row. Mittal et al.[81] developed a CFD model (Tenasi: Finite Volume unstructured flow solver) of a wind turbine at various tip- speed-ratios, evaluating the effect of temporal convergence on the predicted thrust and power coefficient. Three turbulence models were evaluated: Spalart-Allmaras, Menter SST two equations), and DES version of the Menter SST. The results pointed that the DES model is significantly better for predicting velocity components in the wake. Lann et al[82] developed a new k-ε model consistent with Monin-Obukhov similarity theory (MOST), comparing it to other k-ε models. Lann et al[83] developed k-ε-fP viscosity model applied to one on-shore and two off-shore wind farms, and the results were compared with power measurements. The k-ε underpredicts the power deficit of the first downstream wind turbine, while k-ε-fP eddy viscosity shows good agreement with measurements. The difference becomes smaller for wind turbines further downstream. Lann et al[84] achieved an improvement for the k-ε model, comparing this model with the original k-ε eddy viscosity model, the Large Eddy Simulations and a total of 8 field test cases measurements. The results showed a better agreement with measurements and LES in comparison to the original k-ε. Ivanell et al[85] studied stability properties of wind turbine wakes using a CFD model based on Large-Eddy actuator line on the tip vortices of the Tjaereborg wind turbine. Ivanell et al[86] developed a CFD (EllipSys3D) actuator-line model using 5 million mesh points to evaluate downstream wake flow field characteristics and the tip vortices positioning. Larsen et al[87] reviewed several studies in wake aerodynamics. Bromm et al[88] investigated the impact of

directionally sheared inflow in the wake development, and analysis of the impact of wakes on energy production and loading on a downstream turbine. A Large eddy simulation was performed using the actuator line representation. Masson et al.[89] developed a RANS k-ε actuator disc model to assess impacts of the variation of operational parameters influencing the turbulent flow around a wind turbine nacelle. Storey et al[90] developed a technique coupling transient wind simulation with an aero-elastic simulation to dynamically model turbine operation and wake structures. A Large Eddy simulation with actuator disc model was performed for that study. Troldborg et al[91] developed a Large eddy simulation with actuator line technique using 8.4 million grid points to study the near and far wake of a wind turbine at various tip speed ratios. Troldborg et al[92] developed an unsteady RANS actuator line model to analyze wake interaction between two wind turbines under different degrees of ambient turbulence intensity: laminar, offshore and onshore conditions. The results show the influence of the upstream turbine wakes on external blade loading of the downstream turbines. Gopalana et al[93] developed a coupled mesoscale-microscale model (WINDWYO) coupled with WRF (Weather Research and Forecasting) model and CFD codes of different complexity in order to assess the power predictions and wake visualization at the Lillgrund wind farm. Choi et al.[94] developed a CFD model using ANSYS CFX for 2MW wind turbines, and using blade element momentum theory for the blade design. The distance from upstream and downstream wind turbines changed from three to seven times the diameter, and obviously power output was affected. Makridis et al.[95] developed a CFD model in ANSYS Fluent solving the RANS equations, assuming actuator disc model (based on Blade Element Theory) and considering complex terrain and neutral atmospheric wind flow. A validation was performed against wake data over flat

terrain. Neutral atmospheric flow conditions over a hill were tested and validated. AbdelSalam et al.[96] modeled the near and far wake study using RANS rotating reference frame, k-ε turbulence model. A full rotor and actuator disc were compared, and two additional k-ε previously studied in literature. Wake results were validated against 180kW Danwin (three-bladed), showing good agreement. AbdelSalam et al.[97] performed experimental procedure and numerical simulation considering a full rotor model, RANS k-ε modified for atmospheric flows, 2MW wind turbine SODAR upstream measurements, wake LIDAR measurements at downstream distances from 2 to 7 diameters. Boudreau et al[98] studied the axial-flow and cross-flow configurations operating at respective optimal efficiency, with Reynolds number around 10^7, 3D DDES, and Unsteady RANS. Ammara et al[99] developed a RANS steady (CVFEM) model, considering two-rows periodic wind farm in neutral atmospheric boundary layer. Frau et al[100] developed an unsteady CFD (ANSYS CFX) k-ω SST model to compare downwind and upwind configurations for offshore applications, using 9 million to 25 million cells. They concluded that the downwind turbine configuration is better suited for multimegawatt offshore wind turbines. Rosenberg et al[101] extended efforts of the vortex lattice method (VLM) to analyze aerodynamics of dual-rotor wind turbines. Sreenivas et al[102] studied the interaction between two wind turbines (NREL S826 airfoils) operating in tandem for TSR of 2.5, 4 and 7m wind tunnel speed 10m/s. Esfahanian et al[103] developed a CFD models of the NREL Phase II using ANSYS Fluent and BEM improved methodology.

3.2.2.5 Gaps in Literature

Basically the gap existent in literature is related to CFD models capable of simulating a whole wind farm. The vast majority of the methods simulate single turbines,

and only a few of them simulate more than one rotor. The computational resources may be a limiting factor for that, however the gap related to lack of CFD models to simulate whole wind farms can be overcome in other ways. Section 3.3.3 shows a novel approach of this work as an attempt to overcome the main gap identified in literature. In regards to other aspects, there is no well stablished approach to computationally model wind farms. The choice for boundary conditions and turbulence models widely vary in research, and any pattern was identified. Moreover, lack of experimental data in controlled environments for the far wake do not allow researchers to validate their data and improve wake aerodynamics knowledge. Consequently, it is not possible to accurately evaluate wake CFD models found in literature. The majority of the experimental data for far wake characterization come from field experimental data, which are difficult to replicate in computational models.

3.3 Methods: Wind Farm CFD Modeling

3.3.1 Wake Effects

The wake of a wind turbine is characterized by decreased velocity and increased turbulence intensity. There are many analytical methods to estimate the velocity-deficit in the wake, but models based on Computational Fluid Dynamics (CFD) are robust and reliable. In this work, a CFD model was developed to determine the wake velocity deficit and consequently its influence in the wind farm output power. The TI profile in the wake is also characterized using a CFD solver.

3.3.2 CFD Model

The wind turbine modeled in this work was adapted from the previously validated wind turbine CFD model from chapter 1, the MEXICO rotor tested in wind tunnel. The wind turbine blade geometry including twist angle was built using SolidWorks, and then

imported to the ANSYS Design Modeler to build the other turbine components (tower, hub) and the physical domain (Fig. 3.1a). A rectangular physical domain was built, and it was broken into smaller pieces, allowing local wake mesh sizing. The largest rectangle in Fig.3.1a is an exterior part, and the first rectangle corresponds to the near wake until 2 diameters downstream of the rotor. The wake was first simulated with a domain extending 13 diameters downstream of the rotor, but the physical domain was reduced to 5 diameters downstream to use as input for the optimization routine. The numerical code for the optimization will solve each row separately, taking an output from the CFD solver (the velocity flow field) to calculate the objective function.

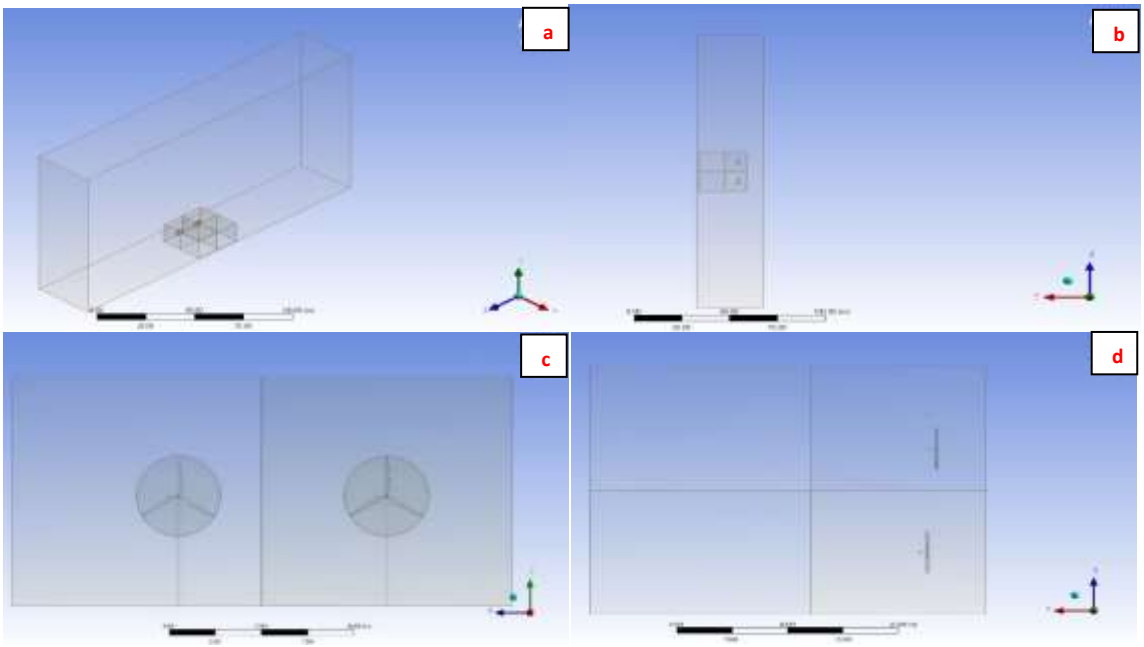

Figure 3.1 a – Physical domain with two rotors. Figure 3.1b – Top view of the physical domain. Figure 3.1c – Front view of the physical domain. Figure 3.1d – Top view of the physical domain.

The strategy for meshing (Fig.3.2) the physical domain is to build a sphere of influence surrounding each rotor, and break the physical domain into smaller rectangles

defining them as the same part in the ANSYS Design Modeler. The sphere of influence option allows for a better convergence of the flow field solution. The smaller rectangles allow the mesh element sizing of the near and far wake to be controlled locally, avoiding gradients in the mesh sizing in the interface of each sub-domain. A full mesh sensitivity study can be found in the Appendix D, showing the need to use 10 million cell elements. The flow field solution is determined using the CFD solver ANSYS Fluent 17, housed in two computers with 64GB RAM and 8 processes for each machine with the processor Intel Xeon CPU E5-1620 v2 3.7GHz. The computational time for each simulation was approximately 10 hours. The simulation was performed using a steady state Moving Reference Frame approach, and setting the rotational speed to match experimental conditions. The turbulence model selected was the k-ω SST, which is suitable for swirl flow, and it was used in the literature studies as their main turbulence modelling technique. Pressure-far-field boundaries, which requires the larger exterior rectangle to achieve convergence, were applied for the lateral and superior boundaries. We also apply pressure-outlet for the exit boundary, and a special type of wall with no shear for the inferior boundary.

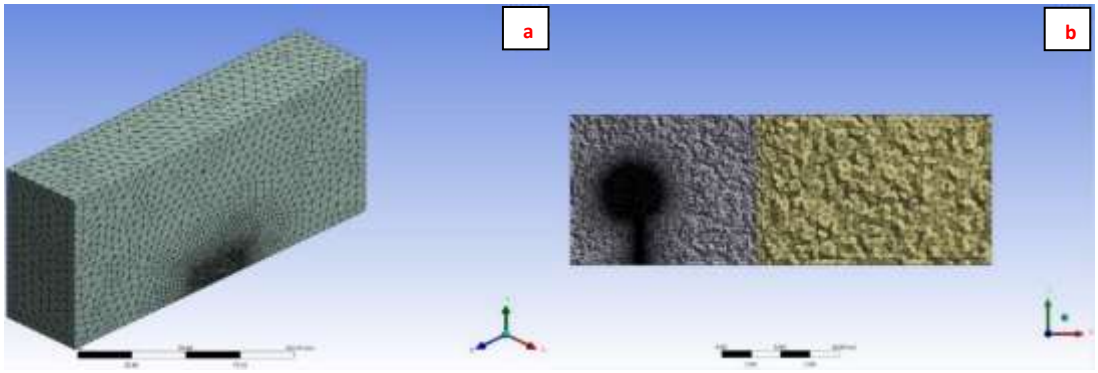

Figure 3.2a – Mesh of the physical domain; Figure 3.2b – Lateral view of the mesh showing internal details of the sphere of influence, and breaking the wake physical domain into smaller parts.

3.3.3 Second and Third Rows Simulation

In this work, we developed a new method to evaluate the second and third rows of turbines where the outlet of the first row becomes the inlet of the second row. This results in a significant reduction in the computational expenses, since there is no need to simulate multiple turbines at once. Multiple turbines would require a mesh with significant higher number of elements. For instance, the three first rows would require three times more elements in comparison with our approach.

3.4 Results

3.4.1 Wind turbine Wake in the 1st and 2nd Rows

3.4.1.1 Velocity and Turbulence Intensity Contours

The intensity of the velocity-deficit decays along the axial distance downstream of the rotor, however the velocity in the wake does not fully recover its free-stream value even after more than 10 diameters downstream of the rotor. Fig. 3.3 shows the velocity contours for the two-turbine case when considering the designed aerodynamic condition for this specific wind turbine ($U=15m.s^{-1}$, $\lambda=6.6$, $\omega=424.5rpm$, $\theta=-2.3°$). The region in red (15m/s)

represents the area where the velocity is not affected by wake effects. On the other hand, the velocity-deficit in the wake of the wind turbine is represented by green and yellow contours.

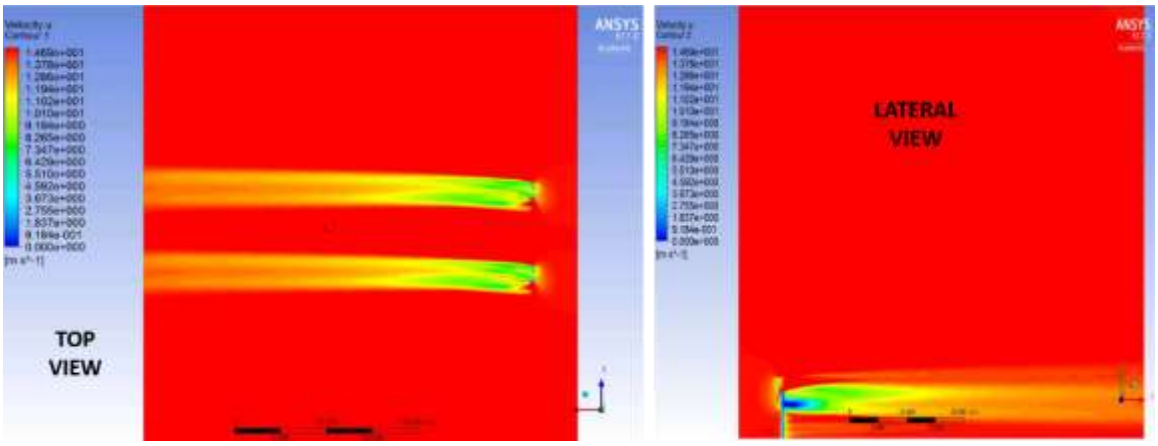

Figure 3.3 – Axial velocity contours for the two-turbine case, representing a first row of wind turbines. The left panel shows the top view, while the right panel shows the lateral view of the wake.

The region free of wake effects becomes smaller after each row of turbines. Fig.3.4 shows the velocity contours for a hypothetical second row of wind turbines, while Fig. 3.5 shows Turbulence Intensity contours. Instead of simulating 4 turbines, the methodology applied uses data from the previous simulation (Fig. 3.3) for the velocity inlet. Basically, the pressure-outlet of the Fig.3.3 became the velocity-inlet profile for the simulation from Fig.3.4. This procedure significantly improves the computational efficiency of the simulation with regards to computational time and convergence, since two turbines are simulated instead of four. The second row of wind turbines was staggered from the first row of turbines, but not completely out of the region affected by wake effects from the first row of turbines. The wake velocity contours in Fig.3.4 show a smaller region of unaffected

velocity (the red region) in comparison with Figure 3.3, meaning that the region free of wake effects becomes smaller after each row of turbines.

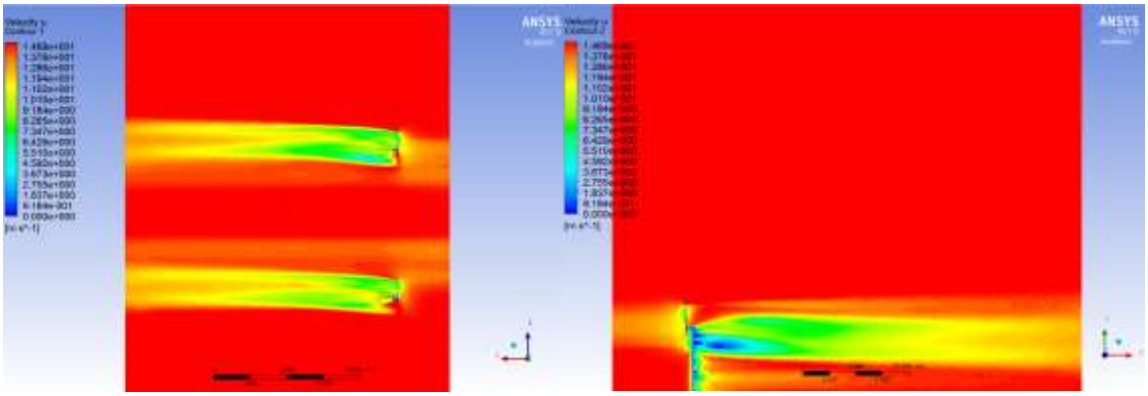

Figure 3.4 – Axial velocity contours for the two-turbine case in a hypothetical second row of wind turbines. The left panel shows the top view, while the right panel shows the lateral view of the wake.

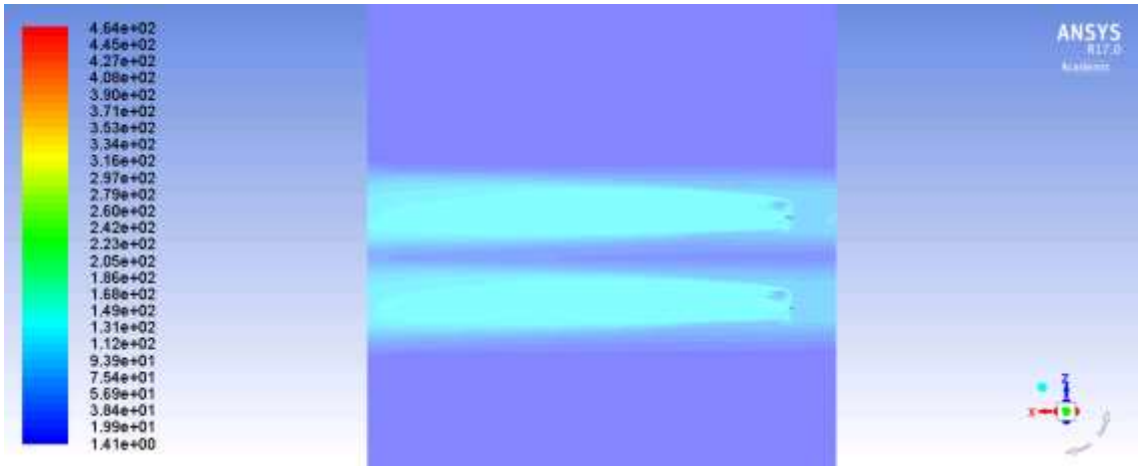

Figure 3.5 – Top view of the Turbulence Intensity contours for a second row of turbines, using a profile from a simulation from a first row of turbines.

Atmospheric stability is a major parameter in the determination of wake size and structure because it controls the size of eddies within the general wind flow, therefore the diffusion of turbulence in the wake. Since the simulations were performed assuming steady state and no perturbations were introduced into the model, the wake velocity contours do not considerably expand. Additionally, the steady state solution is not capable of

determining the blade tip vortex breakdown, which is supposed to happen at the end of the near wake. This potentially explains why the wake velocity field does not expand and does not become a totally conic shape, which would be similar to the Turbulence Intensity field.

3.4.1.2 Velocity and Turbulence Intensity Plots

Wake data plots for the wake of the first and second turbine rows are shown in Fig. 3.6, comparing the behavior of the Velocity Deficit and the Turbulence Intensity. The Velocity Deficit existing in the wake of the second row is slightly higher than the velocity deficit found in the wake of the first row. The Turbulence Intensity of the second row of turbines is considerably higher compared to the same downstream position (10D) of the first row.

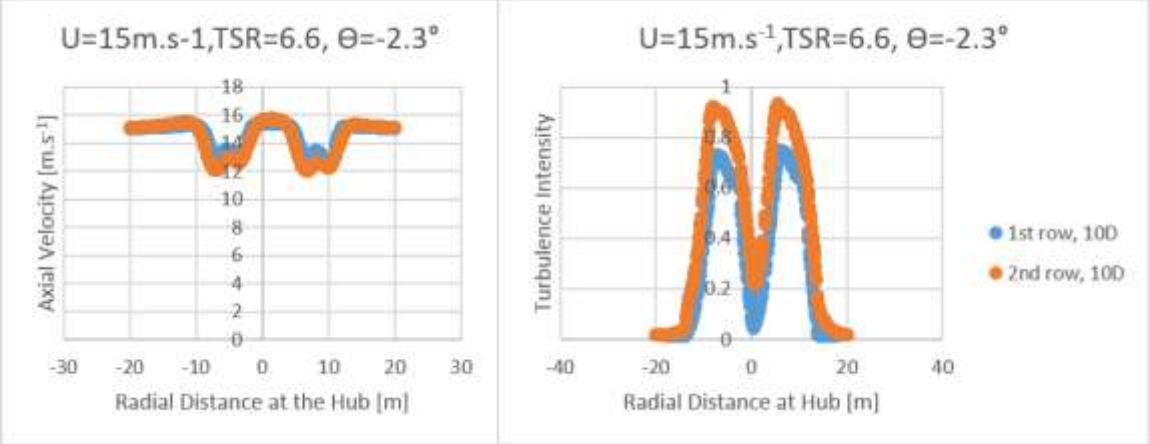

Figure 3.6 – Wake data plots for the Axial Velocity and Turbulence Intensity in the wake of the first and second rows.

The evolution of the wake of a single turbine is shown in Fig. 3.7 and Fig. 3.8 for two different free-stream and TSR values (U=10m.s-1, U=15m.s-1, TSR =4 and 6.6). The velocity-deficit increases as the TSR increases from 4 to 6.6 for all the positions considered in the wake. In regards to a TSR=4 and considering U=10m.s-^{1}, the wake velocity deficit has a peak of approximately 15% at x/D=3 in the near wake, and the velocity deficit

decreases at x/D=6 to approximately 11%. The case of TSR=6.6 and U=10m.s-1 presents a velocity deficit peak of 25% at x/D=3 and 17.25% at x/D=6, which is 9% and 6.25% smaller than the values for U=10m.s-1 and TSR=4. The values of velocity deficit for the case of U=15m.s-1 and TSR=4 are the same of the case U=10m.s-1 and TSR=4, and so are the other two cases (U=10 m.s-1 TSR=6.6, and U=15m.s-1 and TSR=6.6) as suggests the Self-Similar theory.

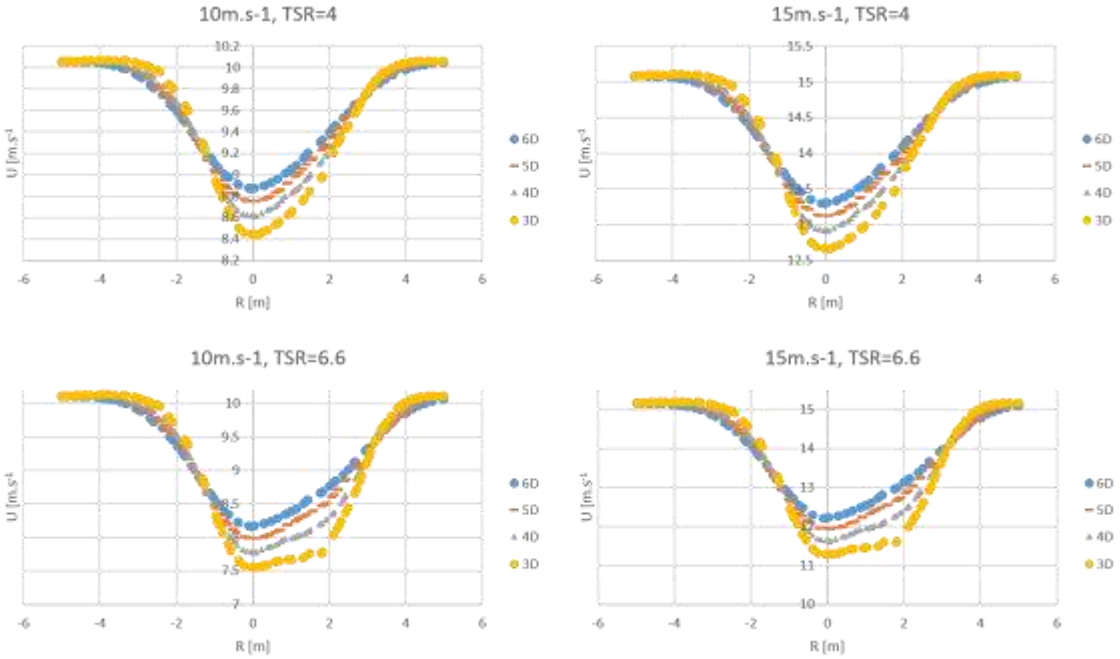

Figure 3.7 – Velocity Deficit for two different values of TSR and free-stream velocity.

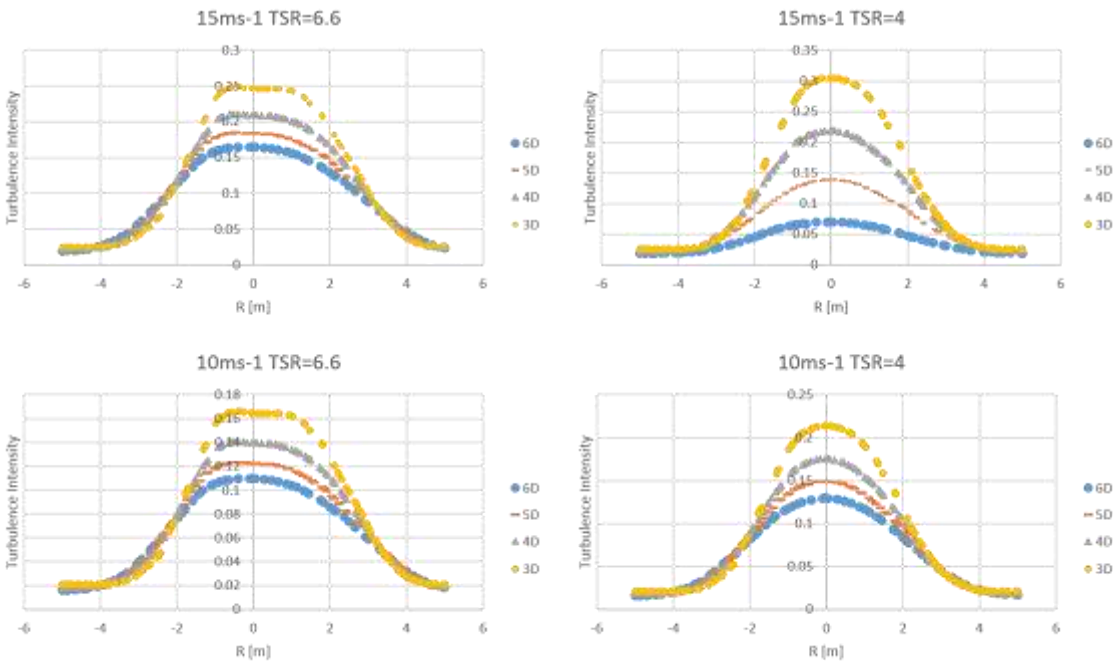

Figure 3.8 – Wake velocity data for several downstream radial positions and TSR, considering U=10m.s-1.

3.4.2 Influence of the Assumptions

The problem of optimizing a wind farm layout is very complex, so the assumptions described in section 1.4.2 are important to allow to find a solution to this type of problem. In this section, the influence of some important design parameters on the Velocity Deficit and the Turbulence Intensity profile in the far-wake development is analyzed including: TSR (Tip Speed Ratio), Pitch Angle (Θ), and Free-Stream Velocity (U). This is very important to verify the range of validity of the solution from the optimization routine to be implemented in chapter 3.

3.4.2.1 Influence of the TSR

The Tip Speed Ratio (TSR or λ) critically influences the far wake behavior. The velocity deficit increases as the TSR increases from 4 to 10, according to the plots from

Fig. 3.9 for axial velocity for lateral and vertical positions at different axial locations downstream the rotor. Comparing the two values of TSR from Fig. 3.9 the highest TSR value (λ=10) presented the highest velocity-deficit in the far wake behavior for all the downstream positions considered. Consequently, the TSR is a critical design parameter affecting the three-dimensional extension of the wake. This parameter must be considered to determine the minimal distances between rotors, since a wind farm experiences several different operational conditions with regards to TSR. The TSR (λ) also critically influences the Turbulence Intensity in the far wake (Fig. 3.9), increasing the TSR means that the Turbulence Intensity will increase too.

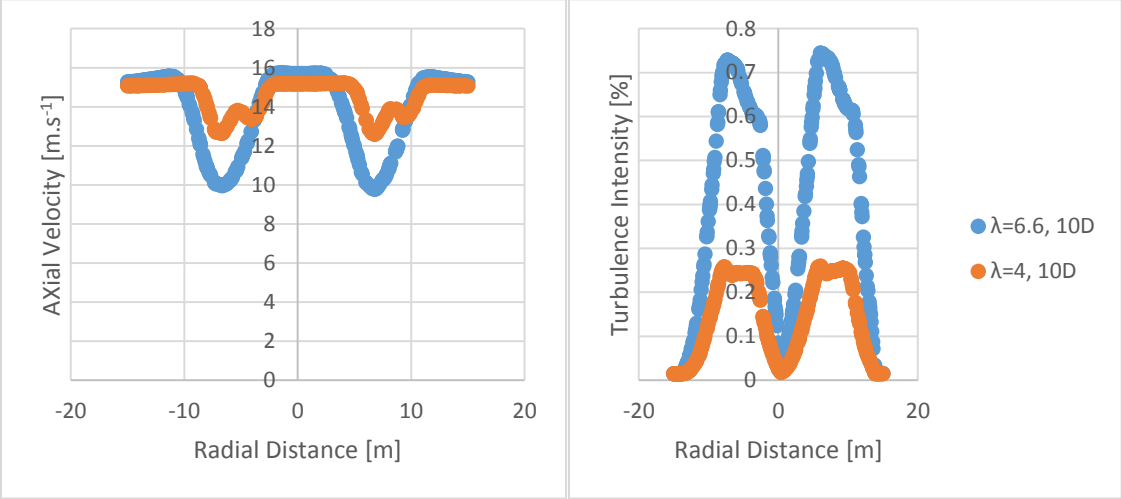

Figure 3.9 – Axial velocity profile (plots on left) profile and Turbulence Intensity (right) profile at one position donwstream the rotor in the wake:10D (diameters). Different line colors represent the Tip Speed Ratio (TSR or λ) of 4 (orange) or 10 (blue).

3.4.2.2 Influence of the Pitch Angle

The Pitch Angle (Θ) has little influence on the Velocity and Turbulence Intensity profile in the far wake. Three different values of pitch angle were tested (Fig. 3.10), considering the same Free-Stream Velocity and TSR conditions. The velocity remains the

same at 5 diameters and 10 diameters downstream the rotor, and the same situation happens for the Turbulence Intensity. This means that this parameter may be disregarded for this optimization routine.

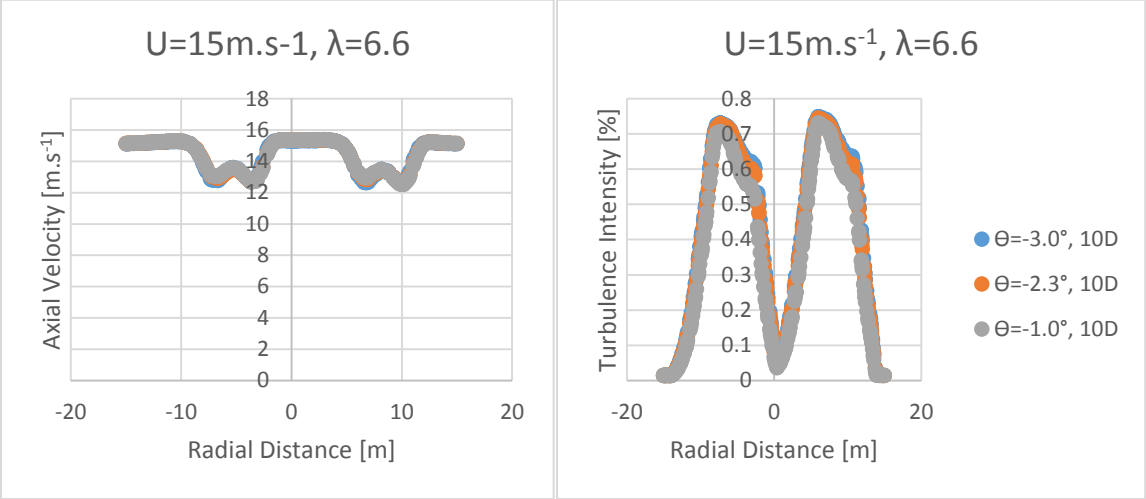

Figure 3.10 – Velocity profile in the far wake considering three different values of Pitch Angle. Influence of the Pitch Angle (Θ) on the Turbulence Intensity profile.

3.4.2.3 Influence of the Free-Stream Velocity

Increasing/decreasing the free-stream velocity value does not affect the magnitude of the velocity deficit (Fig. 3.11, right panel). On the other hand, increasing the free-stream velocity value greatly affects the magnitude of the Turbulence Intensity (Fig. 3.11, left panel). Consequently, it is important to consider variable Free-Stream velocity conditions to verify that the optimal wind farm layout solution is not sensitive to the variation of the velocity.

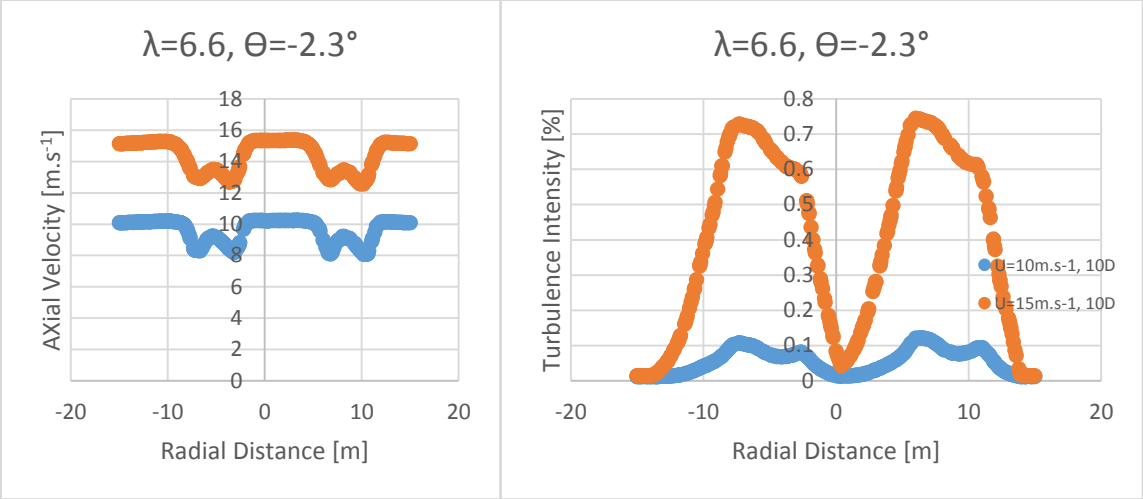

Figure 3.11 – Influence of the Free-Stream Velocity on the Velocity-Deficit and the Turbulence Intensity in the far-wake.

3.5 Discussion

Prospathopoulos et al.[80] considered a downstream spacing of 5D between the turbines, finding a velocity deficit in the wake of 40% at 2.5D and 30% at 3.5D for the stable stratification case of the ECN measurements. Those results are similar to the values found in this present work. Gundling et al.[35] modeled wake wind speed deficits for different wake models and compared them. The UWAKE model has a maximum velocity deficit of 67% at 4R for 5m.s-1, and a maximum velocity deficit of 81% at 7R for 10m.s-1. The FLOWYO LES has a maximum velocity deficit of 70% at 3R for 5ms-1, and a maximum velocity deficit of 83% at 6R for 10ms-1. The wake deficit is similar for the FLOWYO and UWAKE, but little diffusion of the wake was found when using FLOWYO RANS. The diffusion in the wake is similar using UWAKE and FLOWYO LES, while the FLOWYO RANS had not enough turbulent eddy-viscosity produced by the actuator disc to result in similar wake diffusion compared to FLOWYO LES and UWAKE. The HELIOS DES

model has a velocity deficit of 58% at 4R for 5m.s-1, and 65% at 9$ for 10m.s-1. All those values are within an acceptable range when compared to the values found in this work. Mo[36] determined velocity profiles at the wake for several downstream positions. A near-symmetrical but not completely at the blades location, the vertical wake velocity profile has a clear W shape at 1D and 2D, and overall the velocity deficit decreases as the free-stream velocity increases from 5m.s-1 to 15.1m/s. This was attributed to the state of the completed attached flow in the turbine blade for smaller velocities, and not for more extracted power from the incident wind. Wake shape not well defined for the further downstream positions. The W shape of the velocity deficit curves is similar to be curve shape found in this present work. Troldborg[66] analyzed different turbulent inflow conditions for a full rotor model, an actuator line and an actuator disc approach. Actuator Line and Actuator Disc showed the same results for velocity deficit in the wake. A maximum peak of approximately 60% was found at 2R, which remained almost constant in the same value up to the 10R analyzed. The full rotor modeling showed the same 60% of velocity deficit at 2R, but decreasing the peak value to approximately 50% at 10R. Those results are similar to the ones found in this research for the wake characteristics.

In regards to Turbulence behavior, the TKE for the full rotor model showed self-similar TKE curves profile, the minimum TKE peak is at the near wake and there is a constant peak increase for each of the far wake position analyzed. The AL and AD models only started to develop peaks in the curve after 6R, which was smaller than the full rotor model peak but comparable. The AL and AD model had a flat nearly null (zero) TKE curve from 0 up to 6R at the wake, which was not visibly comparable to the full rotor TKE curve. The TKE behavior for the AL and AD was not captured by the lack of solving the BL on

the blades. The results for the full rotor model using DES change compared to the RANS, where the velocity deficit becomes slightly smaller for the DES case. The TKE peak increases for the case of the full rotor DES compared to the full rotor RANS.

Wilson et al.[72] modeled AD, AL and FR. For single turbine case, the velocity deficit is slightly higher for ADM than ALM, and MRM presented the highest velocity deficit in the wake. The TI significantly higher for ADM and ALM when compared with FRM. The wake interaction case showed a strong interaction of wakes when spacing 5D. Mittal[81] analyzed operating conditions of TSR=6 at x/D=5, finding 40% of velocity deficit and not completely symmetrical radial curve profile. Asymmetry was attributed to interaction with tower. For off-design condition of TSR=3, the velocity deficit has a peak of 30% at x/D=5D. For off-design condition of TSR=10 shows a peak of 80% of the velocity deficit at x/D=1D, and 40% at x/D=5D. Those results are consistent with the results found in this work. Storey[90] found that as the free-stream velocity increases and the TSR decreases (rpm maintained constant), the overall velocity deficit decreases. The shape and magnitude of the velocity deficit vary significantly with the wind speed and TSR. The expansion of the wake varies with wind speed, confirming the trend observed in this work. Troldborg[91] analyzed the two turbines case for wake interaction; they found that a spacing of 7D is large enough to allow the wake profile to reach a steady state after the second turbine. AbdelSalam[96] found 65% velocity deficit peak for x/D=2, 60% velocity deficit peak at x/d=4, 50% peak velocity deficit at x/D=6; 30% velocity deficit peak at x/D=8. Those results are within acceptable agreement with the results found in this work.

In regards to field experimental data, Barthelmie et al.[104] studied the influence of the downstream spacing between the turbine rows in the normalized power for the case of

the Horns Rev. Considering 8m/s and the 2 degree sector and a downstream spacing of 7D, the ratio between the output power of the second and first turbine rows is approximately 58%. The output power ratio between the second and third rows is 56%. For a downstream spacing of 9.4D, the ratio between the output power of the second and first turbine rows is approximately 70%. The output power ratio between the second and third rows is 68%. For a downstream spacing of 10.5D, the ratio between the output power of the second and first turbine rows is approximately 75%. The output power ratio between the second and third rows is 70%. Considering 8m/s and the 30-degree sector, the downstream spacing of 7D has a ratio between the output power of the second and first turbine rows of approximately 80%. The output power ratio between the second and third rows is 79%. For a downstream spacing of 9.4D, the ratio between the output power of the second and first turbine rows is approximately 85%. The output power ratio between the second and third rows is 80%. For a downstream spacing of 10.5D, the ratio between the output power of the second and first turbine rows is approximately 88%. The output power ratio between the second and third rows is 83%.

3.6 Conclusions

In this work, a CFD model based on moving reference frame approach was developed to assess wind turbine far wake characteristics according to operating conditions typically experienced in commercial wind farms. The influence of the TSR and Free-stream wind speed on wake characteristics such as velocity deficit and Turbulence Intensity was discussed and compared with existing literature on this topic.

This paper reviewed most of the wind turbine wakes studies and wind farm CFD techniques from literature. We found that in overall the existing literature studies use

different turbulence modelling techniques, as well as CFD solvers with different assumptions. The wake results vary according to the approach adopted in each work. In regards to the velocity deficit assessment, the values found in this work is similar to other CFD wake studies in literature. This demonstrates the ability of the proposed CFD model in predicting wake characteristics, and this way the model is ready to apply for determining the optimal spacing between turbines in a wind farm. The capability of the proposed CFD model showed to be consistent when compared with field data and kinematical models results, showing similar ranges of wake deficit.

A FSI (Fluid Solid Interaction) model would be relevant to determine how the structural behavior of the blades is affected by variable wind conditions. Although the deformation of the blades will have an impact on the blade fatigue lifetime, no study has previously shown that far wake aerodynamics is significantly impacted by the level of blade deformation.

Further improvement of the model will include a transient approach modeling to determine wake characteristics according to variable rotor operating conditions. This will extend the capabilities of the proposed model by adding a more realistic modeling approach to derive the aerodynamic behavior of the turbine rows.

Chapter 4: Automated CFD Gradient-Based Optimization to Maximize Wind Farm Performance and Land-Use

Abstract

In this work, a CFD optimization routine automated in MATLAB was implemented to maximize wind farm land use. The use of land in wind farms was improved in 10% when a staggered configuration was implemented in comparison with aligned designs. Remarkable conclusions refer to the use of staggering: it is possible to have a significant improvement on the use of land and output power production by staggering the second row. The second part of this work approached the use of control strategies, which consists in slightly reducing the rotational speed of one of the wind turbine rows. Although a slight reduction in the output power of this row may happen, increased wake velocities for the next rows have the possibility to increase the total wind farm output. The two cases of study here showed improvements within 2.52% and 4.63% in the output power, consequently in the wind farm land use.

4.1 Introduction

A possible solution to reduce the amount of land used in wind farms is to improve the efficiency of the layout by rearranging the wind turbine rows. The understanding of wake aerodynamics behavior must be the guide for optimal wind turbines positioning decision in a wind farm, this way determining the areas more affected regarding velocity

deficit and turbulence intensity. Literature shows that the majority of the studies on wind farm optimization use analytical models to simplify the analysis of three-dimensional wake effects, but no work has been rigorously done to better model three-dimensional wake effects. The wind farm land-use and its footprint could be reduced if correctly designed taking into consideration the wake flow field characteristics according to variable operating conditions. A solution from a CFD (Computational Fluid Dynamics) solver coupled with a gradient-based optimization method is a powerful tool to optimize wind farm layout and utilized in this study to demonstrate the potential impact on design.

Literature shows that there are not many studies focused on a reduction of wind farm footprint. Currently, some of the efforts focus on the wind farm land use and footprint optimization includes landowner modelling with cost-economic analysis performed by Guirguis et al[105]. Land footprint is analyzed by Guirguis et al[106], including land-use constraint. A possible step towards optimization of wind farm-land use is the application of multiple hub locations. A comparison between a constant hub height wind farm and a multiple hub heights wind farms was performed by Vasel-Be-Hagh et al[107], showing that the multiple hub heights configuration achieved an improvement of 5.4% in the produced power, with both options using the same horizontal layout, turbine type and wind direction. Moreover, several efforts using different methodologies have been done to achieve layout optimization, focusing on finding optimal spacing between turbines in a wind farm. Park & Law[12] applied sequential convex programming to maximize wind farm output power by optimizing the placement of wind turbines of the Horns Rev 1 wind farm in Denmark. They found that the optimal spacing between wind turbines is dependent on the wind direction. Scattering the turbines helped to avoid wake chain effects, so that downstream rotors were

not significantly affected. Moreover, the same study considered wind statistical data to optimize the wind farm power production over a long period, resulting in a 7.3% power increase. Son et al.[13] found that the total wind farm output power is strongly related to the distance between the first and second wind turbine rows. When the referred distance became larger, the output power considerably dropped in comparison to smaller distances. This means that the increase of the spacing between the first and second rows is ineffective in improving output power. On the other hand, decreased distances made the second wind turbine row much less efficient. They discovered the importance of keeping turbines as close as possible, but with enough space so that the second row can have guaranteed output power. Longer distances did not contribute to increase the total output power. Further, increasing the space between the fourth and the fifth rows has a better contribution than increasing the space between the first and second rows. Wu & Porté-Agel[14] investigated two layout configurations in the same area with 30 turbines either arranged in aligned or staggered conditions. In comparison to the aligned configuration, the staggered one allows better wake recovery. This exposes the downstream turbines to higher local wind speeds (consequently higher performance) and lower turbulence intensity. Stevens[15] found that the distance of 10 diameters (or higher) would minimize the cost per unit of energy production, and the same is true for a distance of 15 diameters if the objective function was evaluated using dimensionless parameters. Those value are significantly higher than applied values in wind farms (6-10 turbine diameters). Meyers[16] found that the current wind farms layout solutions in literature have characteristics with considerably lower spacing than computationally optimized layout solutions. Furthermore, other efforts have attempted to achieve wind farm optimization using control strategies to mitigate wake effects, applying

sub-optimal operating conditions. This means that each rotor will not necessarily deliver the best aerodynamic performance, but the goal is to find the best solution that avoids wake interaction effects, increasing the total wind farm output power. Park[17] studied control strategies for wake effects mitigation, showing that control techniques can be applied for each individual rotor to improve overall wind farm efficiency. González[18] proposed the individual selection of an operating point on each wind turbine in order to maximize the overall wind farm output power. This is performed by studying the optimal pitch angle and tip speed ratio of each rotor in regards to the total wind farm output power. Additionally, the methodology also allows decreased turbulence intensity levels in the produced wakes. The results showed increased power production when the wind speed is lower than the rated wind speed, and for non-prevailing wind directions. Lee[19] found an increase of 4.5% in the total output power by applying pitch angle control for the Horns Rev wind farm. Kazda[20] applied weakened wake conditions for upstream turbines by using sub-optimal operations through control strategies. They found that a 12.5% reduction for the upstream turbines resulted in a 2.5% increase in the sum of the upstream and downstream turbines. This could be achieved by either a change of 3.5° in the pitch angle or by a 24% reduction in TSR compared to optimum TSR. For the case of two upstream turbines operating at 87.5% of optimal conditions, the sum of total power of the upstream and downstream turbines increased by 9.7%. Gil[21] applied control strategies, achieving from 1.86% up to 6.24% in energy captured by using sub-optimal operating points. Chowdhurry[22] found that using variable rotor diameters improved efficiency, achieving 30% increase in the total power generation. Churchfield et al[108] analyzed yaw misalignment measurements at the Scaled Wind Farm Technology facility (Sandia Laboratory), measuring the impact of wake

deflection on the wind plant operation. Fleeming et al[109] studied wake mitigation strategies such as yaw and tilt angles control, and Fleeming et al[110] developed wind plant control strategies and position layout optimization in order to improve the cost of energy. Gebraad et al[111] studied yaw wake effects using a model called FLORIS (Flow Redirection and Induction in Steady-State), which predicts wake locations and flow velocities at each turbine, and the electrical energy production levels are monitored as function of the axial induction factor and the yaw angle. Gebraad et al[112] developed a wind-plant modeling and optimization tool for improving wind plant annual energy production (AEP) based on yaw-based wake and layout control. A study demonstrated enhancement of 5% in AEP for a wind farm by combining wake steering control and layout optimization.

All these efforts in the literature described above provided relevant contributions to wind farm optimization and turbine spacing research. However, they did not consider a rigorous evaluation of three-dimensional wake effects, which this study will achieve. The necessity for improving wake models has become more apparent over the last decade with the continuous growth of the wind energy market. Literature shows that there are several analytical wake models, but analytical models do not consider variation on wake characteristics according to variable operating conditions. In this sense, Computational Fluid Dynamics (CFD) models have the capabilities to model wake velocity deficit and Turbulence Intensity (TI) according to variable operating conditions. Although computationally expensive, CFD models are powerful tools that can be applied to solve some of the most complex problems in engineering. In the context of science applied to wind farm optimization, this work proposes an effective automated gradient-based optimization tool that allows for multiple hub locations is developed and shown in this

work. The tool is coupled with a CFD solver, being able to rigorously evaluate three-dimensional wake effects influencing on the wind farm output power and Turbulence Intensity. The goal of this research is to propose an optimal wind farm layout configuration to maximize the ratio between instantaneous output power and wind farm area. The optimization routine is automated using MATLAB functions and journal files for the CFD solver. The problem formulation and the assumptions assumed in this work are discussed in section 4.2. The description of the automated gradient-based optimization routine implemented in MATLAB and ANSYS Fluent will be discussed in section 4.2.4. The optimal solution from automated optimization routine is presented and discussed in the section 4.3.

4.2 Methods: Wind Farm CFD Modelling

4.2.1 Wake Effects

The wake of a wind turbine is characterized by slowed velocity, and increased turbulence intensity. There are many analytical methods to estimate the velocity-deficit in the wake, but models based on Computational Fluid Dynamics (CFD) are robust and trustable. In this work, a CFD model was developed to determine the wake velocity deficit and consequently its influence in the wind farm output power. The Turbulence Intensity profile in the wake is also characterized using a CFD solver. Section 3.2.2 describes the CFD model developed in this work to simulate wake variable conditions. Section 3.2.3 shows in details the analytical method based on Blade Element Method (BEM) theory applied to estimate the output power each wind turbine according to incident wind conditions, and the rotor geometry. Section 3.2.4 fully describes the CFD automated gradient-based optimization routine implemented in this work.

4.2.2 Wind Turbine Wake CFD Model

The wind turbine modeled in this work was adapted from the previously validated wind turbine CFD model of the MEXICO rotor from chapters 1 and 2. The wind turbine blade geometry including twist angle was built using SolidWorks, and then imported to ANSYS Design Modeler to build the other turbine components (tower, hub) and the physical domain (Fig. 4.1a). A rectangular physical domain is built, and it is broken into smaller pieces, allowing local wake mesh sizing. The largest rectangle in Fig.4.1a is an exterior part, and the first rectangle corresponds to the near wake until 2 diameters downstream of the rotor. The wake was first simulated with a domain extending 13 diameters downstream of the rotor, but the physical domain was reduced to 5 diameters downstream to use as input for the optimization routine. The numerical code for the optimization will solve each row separately, taking an output from the CFD solver (the velocity deficit) to calculate the objective function. In order to optimize the use of the computational resources, the outlet of the 1st row becomes the inlet of the 2nd row though the definition of a profile function. The same happens for the 3rd row, which uses the outlet from the 2nd row simulation.

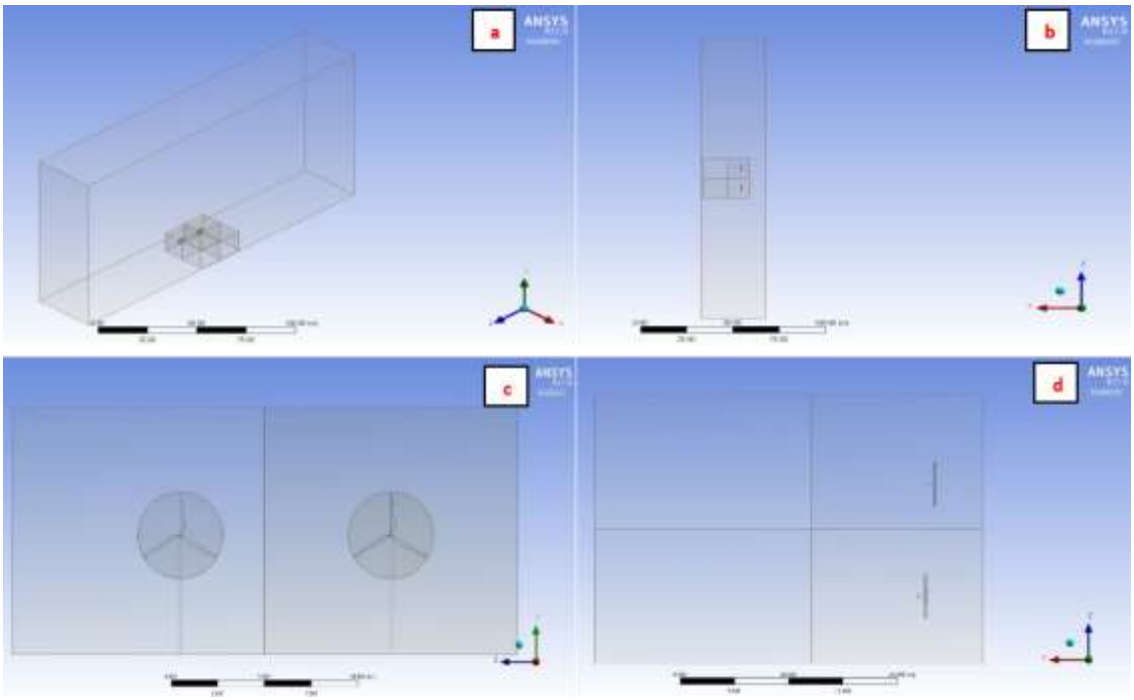

Figure 4.1a – Physical domain with two rotors. Figure 4.1b – Top view of the physical domain. Figure 4.1c – Front view of the physical domain. Figure 4.1d – Top view of the physical domain.

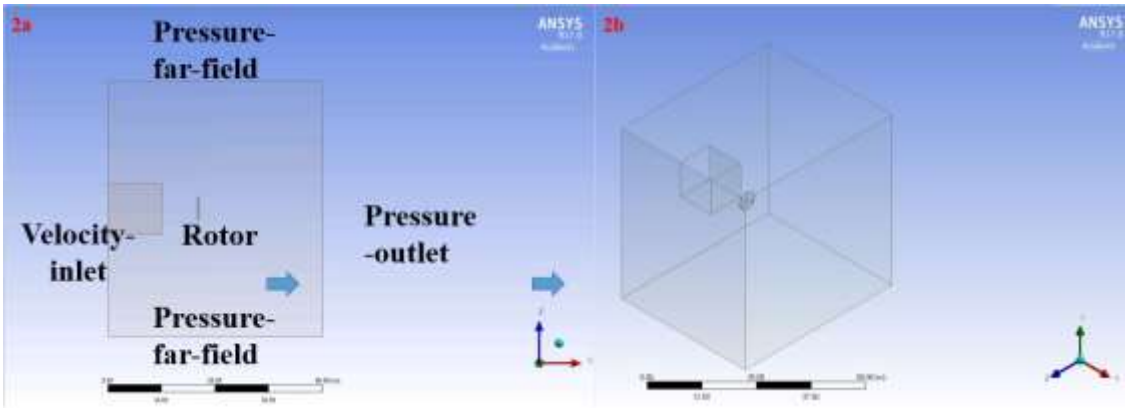

Figure 4.2 – Three-bladed wind turbine (Mexico Rotor) geometry, including twist angle and variable chord length.

The strategy for meshing (Fig.4.3) the physical domain is to build a sphere of influence surrounding each rotor, and break the physical domain into smaller rectangles defining them as the same part in ANSYS Design Modeler. The sphere of influence option

allows for a better convergence of the flow field solution. The smaller rectangles allow the mesh element sizing of the near and far wake to be controlled locally, avoiding gradients in the mesh sizing in the interface of each sub-domain. The mesh sensitivity study was presented in chapter 1. The flow field solution is determined using the CFD solver ANSYS Fluent17, two computers with 64GB RAM/ 8 processes for each machine with the processor Intel Xeon CPU E5-1620 v2 3.7GHz. The computational time for each simulation was approximately 10 hours. The simulation was performed using a steady state Moving Reference Frame approach, and setting the rotational speed to match experimental conditions. The turbulence model selected was the k-ω SST, which is suitable for swirl flow, and it was used in the literature studies as their main turbulence modelling technique. Pressure-far-field boundaries are applied for the lateral and superior boundaries (which requires the larger exterior rectangle to achieve convergence), pressure-outlet for the exit and a special type of wall with no shear for the inferior boundary.

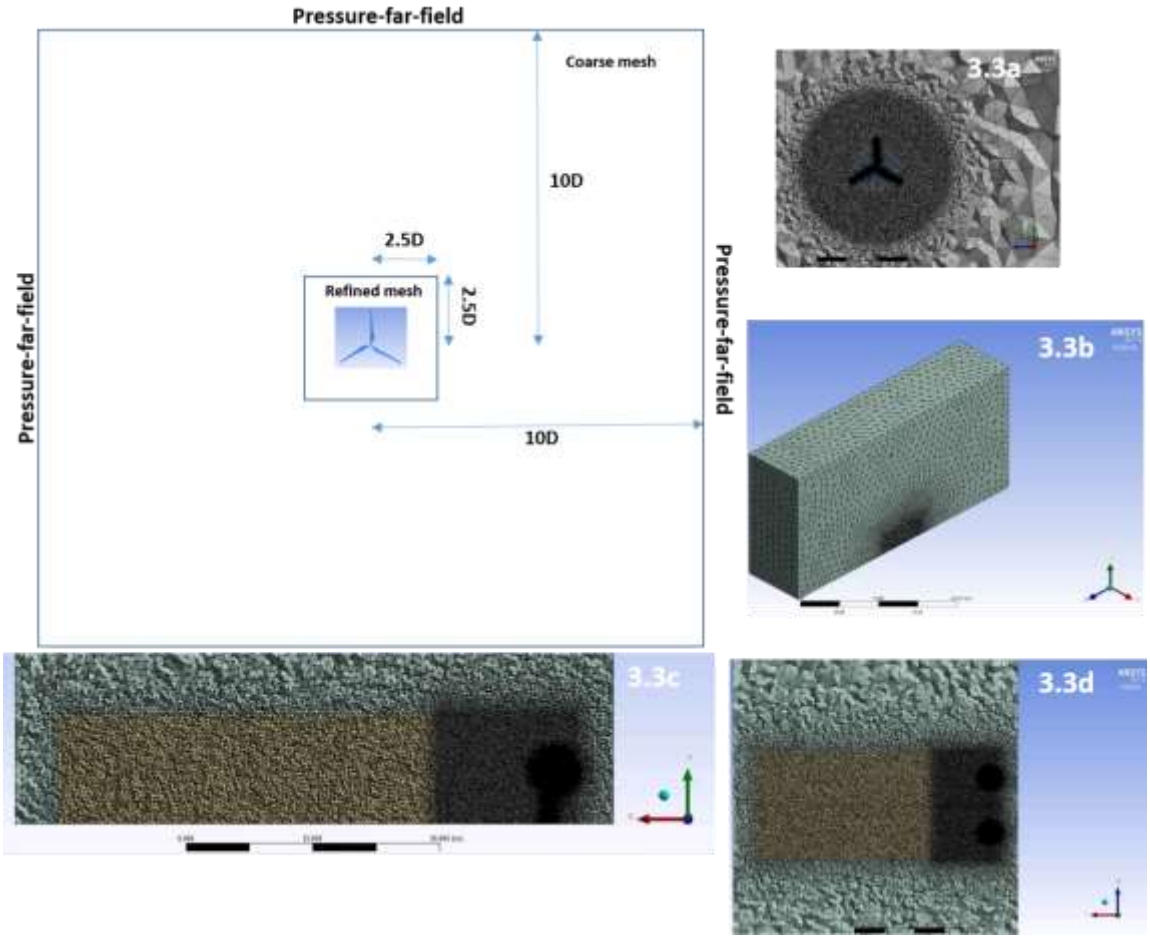

Figure 4.3a – Central rotational disc showing the sphere of influence. Figure 4.3.b – Mesh of the physical domain. Figure 4.3c – Lateral view of the mesh showing internal details of the sphere of influence, and breaking the wake physical domain into smaller parts. Figure 4.3d – Top view showing the mesh of the wake.

4.2.3 Blade Element Model to Estimate Output Power

In this work, the output power of each rotor is estimated using the Blade Element Momentum Theory (BEMT). The wind turbine blade is broken into smaller pieces, which are assumed to behave independently. Eq. 4.7 represents the mechanical output power production from each segment, and the total mechanical output power is the sum of the contribution of each blade segment multiplied by the rotational speed. The relative velocity

in Eq. 4.8, 4.9 and 4.10 is a function of the axial (a) and tangential induction factors (a'), which are dependent on the local velocity in each blade segment. Another set of equations is utilized to estimate the induction factors (Eq. 4.1 to Eq. 4.10), and the 7 steps iterative methodology described by Hansen[113] was applied in this work (Fig. 4.5). The 7 steps described by Hansen[113] include initialization typically with a=a`=0, and Eq. 4.1 to Eq. 4.10 are iteratively solved according to a tolerance. Lift and Drag data were consulted in literature (Bertagnolio et al[114]). Fig. 4.4 shows the aerodynamic conventions adopted in this work. Fig. B1 (Appendix B) shows an example of the excel spreadsheet implemented to calculate the output power in this work using the BEMT theory.

$$\tan\phi = \frac{U(1-a)}{\omega r(1+a')} \tag{4.1}$$

$$\alpha = \phi - \theta \tag{4.2}$$

$$C_n = C_l \cos\phi + C_d \sin\phi \tag{4.3}$$

$$C_t = C_l \sin\phi + C_d \sin\phi \tag{4.4}$$

$$a = \frac{1}{\frac{4(\sin\phi)^2}{\sigma C_n}+1} \tag{4.5}$$

$$a' = \frac{1}{\frac{4\sin\phi\cos\phi}{\sigma C_t}+1} \tag{4.6}$$

$$dP = 0.5.\rho B U_{rel}^2 C_n c r dr \tag{4.7}$$

$$U_{rel} = \frac{U(1-a)}{\sin \phi} \tag{4.8}$$

$$U_{rel} = \frac{\omega r(1+a')}{\cos \phi} \tag{4.9}$$

$$U_{rel} = \frac{U(1-a)}{\omega r(1+a')} \tag{4.10}$$

Where a: axial induction factor; a': tangential induction factor, ϕ: flow angle; ω: rotor rotational speed; r: local radius; U: free-stream velocity; σ: blade solidity; B: number of blades, P: Mechanical Power.

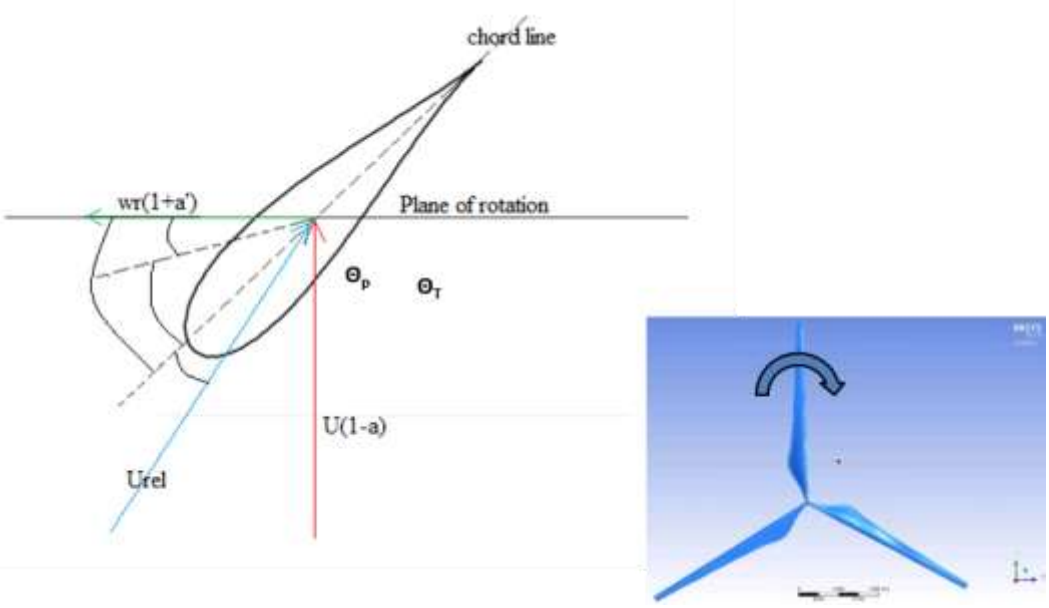

Figure 4.4 – Aerodynamics definitions and signal convention to develop the numerical code based on Blade Element Theory.

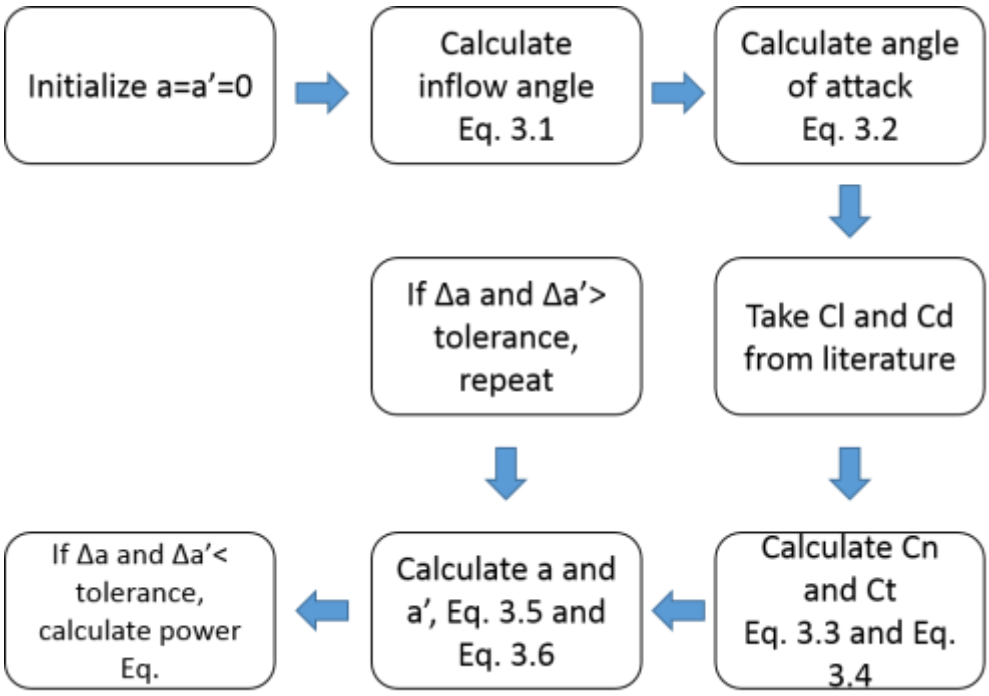

Figure 4.5 – Workflow of the 7 steps iterative process proposed by Hansen.

4.2.4 CFD Automated Gradient-Based Optimization

A gradient-based optimization framework automated in MATLAB will determine the optimal position of the second and third rows of turbine, considering a pre-determined condition for the first row. Previous works have shown fmincon is a suitable MATLAB optimization function to optimize complex fluid systems[115, 116]. The optimization function applied in this work is the fmincon function, which is a MATLAB nonlinear programming solver tool that finds the minimum of constrained nonlinear multivariable functions. The fmincon function has five algorithms options: interior-point (default), trust-region-reflective, sqp, sqp-legacy, and active-set. The fmincon provides a local solution according to an initial guess, and a choice of lower and upper boundaries. The choices for the lateral

boundaries in this work are shown in Figs. 4.6a, 4.6b and and 4.6c, and the downstream distance between rows is also set to vary with the sqp algorithm.

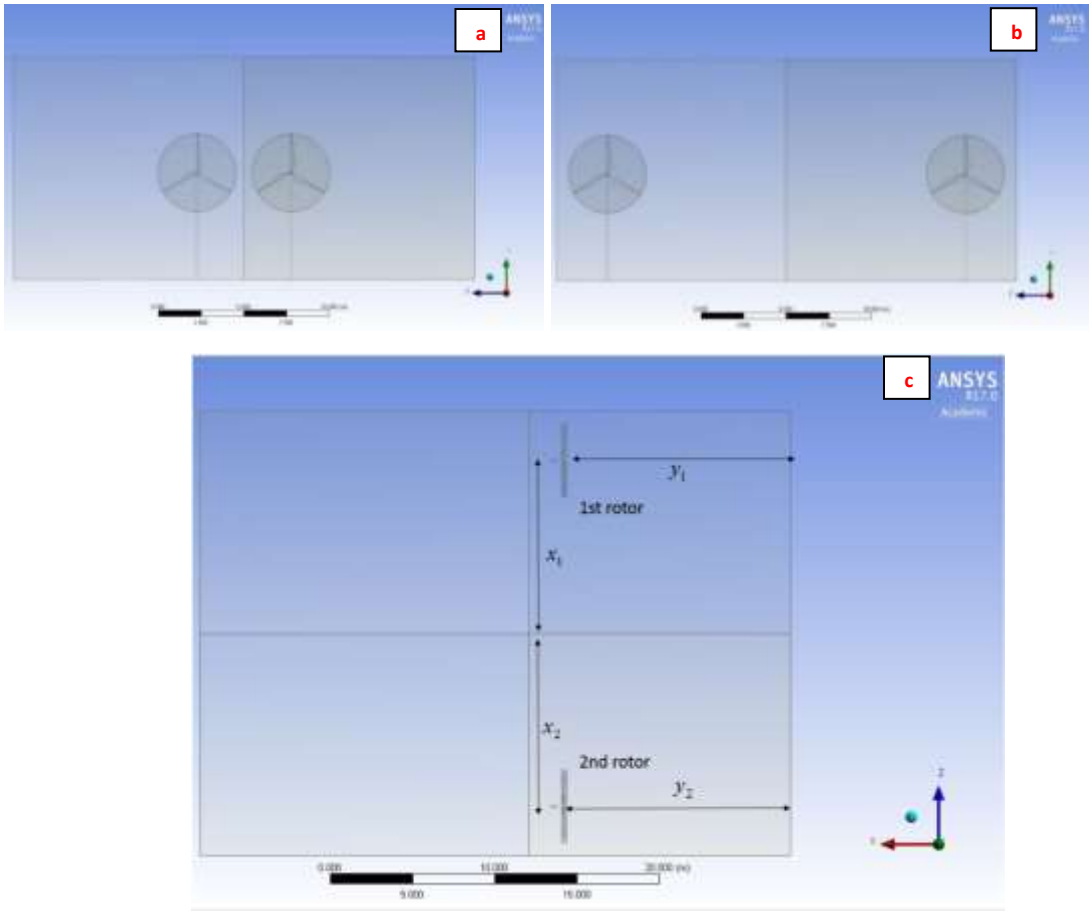

Figure 4.6a and 4.6b: Front view of the lower boundaries for the optimization function; Figure 4.6c: Top view of the physical domain showing each rotor location, and the area occupied by each of them as a function of x and y coordinates.

4.2.4.1 Land Footprint and Objective Function

A MATLAB scripting code was developed to automate the optimization routine, allowing for the use of the CFD solver Ansys Fluent in batch mode (Appendix C). The MATLAB code includes journal (.jou extension) files to access ANSYS Fluent, string replacement MATLAB functions (.m extension) and workbench journal files (.wbjn extension) to update geometry of the second and third row of turbines (Fig. 4.7). The

objective function is set to minimize the ratio m^2 (superficial area of the wind farm row) / kW (instantaneous mechanical output power) /, thus the fmincon function algorithm sqp minimizes the ratio m^2/kW for the two rotors in the physical domain (Eq. 4.11). The objective function accounts for the output power of two rotors in each of the three turbine rows, according to area occupied by each of them as a function of x and y coordinates (Fig. 4.4c).

$$\boldsymbol{f = \sum_{i=1}^{i=6} \frac{kW_i}{x_i y_i}} \tag{4.11}$$

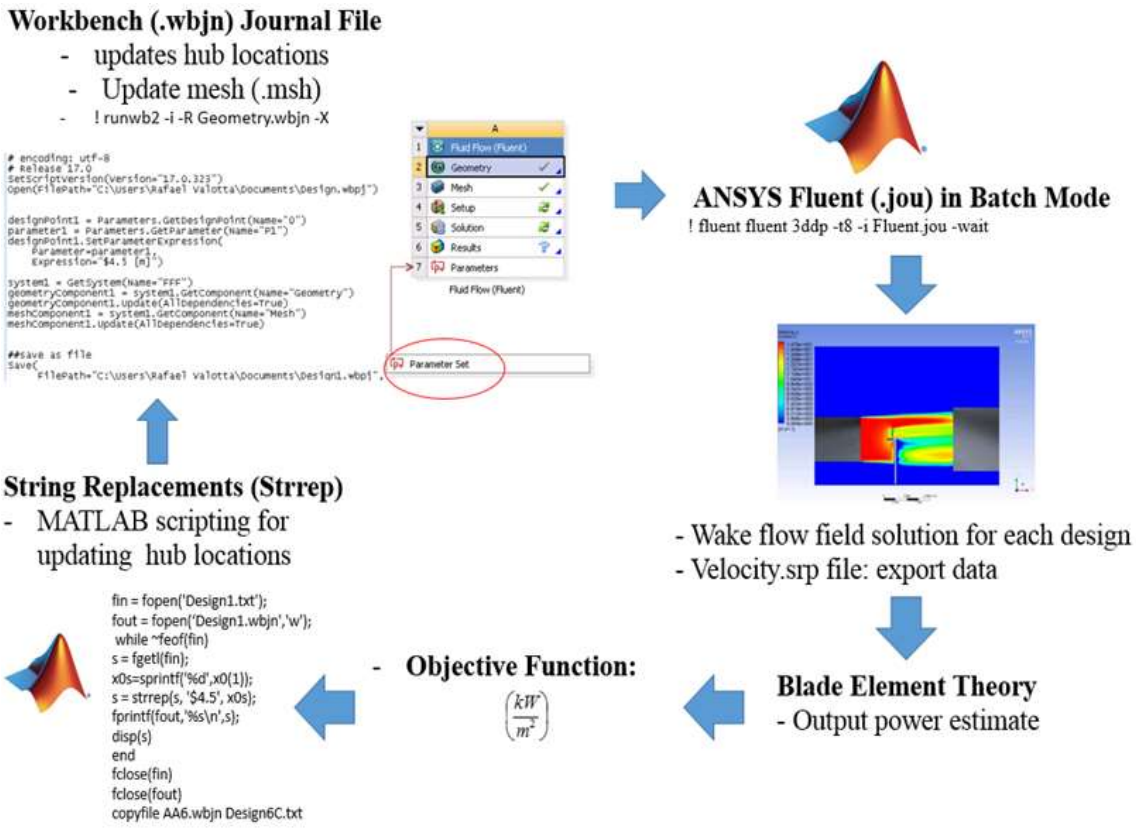

Figure 4.7 – CFD automated gradient-based workflow: Automated optimization routine to optimize wind farm land use.

4.2.4.2 Optimization Assumptions

The wind farm layout optimization problem is complex, and some assumptions were made in this work to simplify the analysis:

1) The wind turbine used in this work is the MEXICO rotor, a small wind turbine prototype recently developed in a consortium with more than ten research centers in Europe, and NREL (National Renewable Energy Laboratory). The near wake data for this rotor was previously validated against wind tunnel experimental data from literature by Rodrigues and Lengsfeld[117, 118], however there is no experimental far wake data available for comparison in literature.
2) The steady state approach for the CFD solver (Moving Reference Frame) allows the user to setup a rotational speed value for the wind turbine to analyze off-design conditions. The wind resource incident on the first row of wind turbines and the rotational speed for all rotors is set in the CFD solver to the match the same experimental conditions (ω=424.5rpm, U=15m/s and Θ=-2.3°). There is no velocity gradient in any direction. The pitch angle is set to be constant Θ=-2.3°, since chapter 3 demonstrated that there is no significant influence of the Pitch Angle on the wake development
3) In the control strategies section, the rotational speed of each row of turbines is set differently aiming to analyze how control strategies can influence on the total output power of a wind farm.
4) The first, second and third rows of turbines are modeled with 2 rotors in each row. Initially, the lateral distance between the two rotors in the first row of turbines is

assumed to be one diameter and a half. The position of each of the two rotors in the second and third rows is the optimization parameters that will be varying in the optimization routine implemented in MATLAB.

5) Flat terrain condition is assumed.
6) The problem was initially assumed three-dimensional: multiple hub locations possible, as well as lateral and horizontal positions for the turbines. The complexity of the problem led us to assume only two dimensional variation for the turbines position.

4.3 Wind Farm Optimization Results

4.3.1 Land Use Optimization

Fig. 4.8 shows the plots from the optimization routine implemented using the work flow previously described in MATLAB and ANSYS Fluent. The position of the 1st row was set to not vary, and the fmincon sqp algorithm varies the position of each individual rotor for the 2nd and 3rd rows searching for an optimal solution. The initial guess assumed for this case is a totally aligned configuration for the three rows. Comparing the worst and the best layout configuration from a total of 40 different wind farm configurations, an improvement of 6.63% has been achieved in regards to the objective function defined in optimization routine. In terms of the total output torque produced by all the turbines, the improvement was 3.34%.

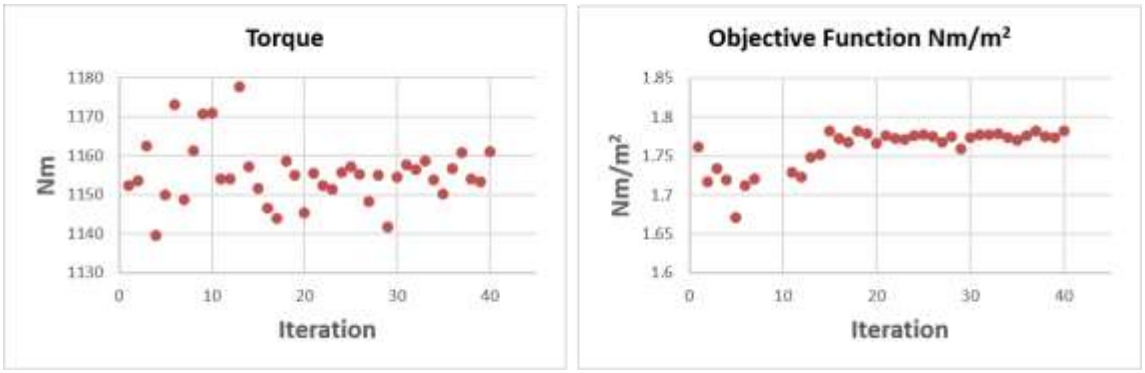

Figure 4.8 – Torque (Fig.Z1) and Objective Function (Z2), considering an initial guess of totally aligned rows.

The optimization results from Fig. 4.8 show an important conclusion: for aligned configurations, there is no significant improvement in the use of land (ratio output power by area) by only varying the position of individual rotors in the rows. This happens because as the individual rotor increases the output power production by moving to areas less affected by wake effects, the area of the row increases too. This does not represent enough increase for the sqp algorithm to keep on attempting to improve the objective function, since varying any of the design parameters produces approximately the same outcome. The optimization routine implemented in this work seeks to find a local minima optimized solution by varying the position of each individual rotor in the rows, meaning that originally the wind farm was allowed to have any sort of layout. The initial guess was set to test a design configuration where the turbines are in totally aligned positions in the 1st, 2nd and 3rd rows. For totally aligned wind farm configurations, the results from Fig. 4.8 show that there is no improvement more than 6.63% in the objective function and 3.34% in the output power by only varying the position of each individual rotor in each of the rows.

On the other hand, staggering the entire 2nd row totally away from the wake effects from the 1st row would certainly have an impact on the output power. Although the total area of the wind farm is going to increase by doing that, the effect on the total output power can equalize or even overcome the ratio kW/m^2. Therefore, this research focused on comparing staggered and aligned configurations in regards to output power, area and ratio output power over the area. A comparison between staggered and aligned configurations show that the effect of staggering can have a positive impact on the total output power and on the ratio between output power and wind farm area (which corresponds to the objective function defined in this work). Fig. 4.9 shows an example of a comparison between a staggered and an aligned configuration. The staggered configuration has 33.3% more area than the aligned one, but the ratio output power over the area is 10% greater than the aligned configuration. The output power of the staggered design is 46.7% higher than the power production of the aligned design, what explain the extra gain in the use of land by using staggered configurations. Although it would be possible to have a larger spacing for the aligned configuration to reduce wake effects, this would bring an extra cost in terms of area. Future work should address the impact of increasing the spacing between the rows in totally aligned configurations, and compare with staggered designs to check if there can be any gain on land use by doing that. However, Son et al[13] demonstrated that longer distances between the rows did not contribute to increase the total output power.

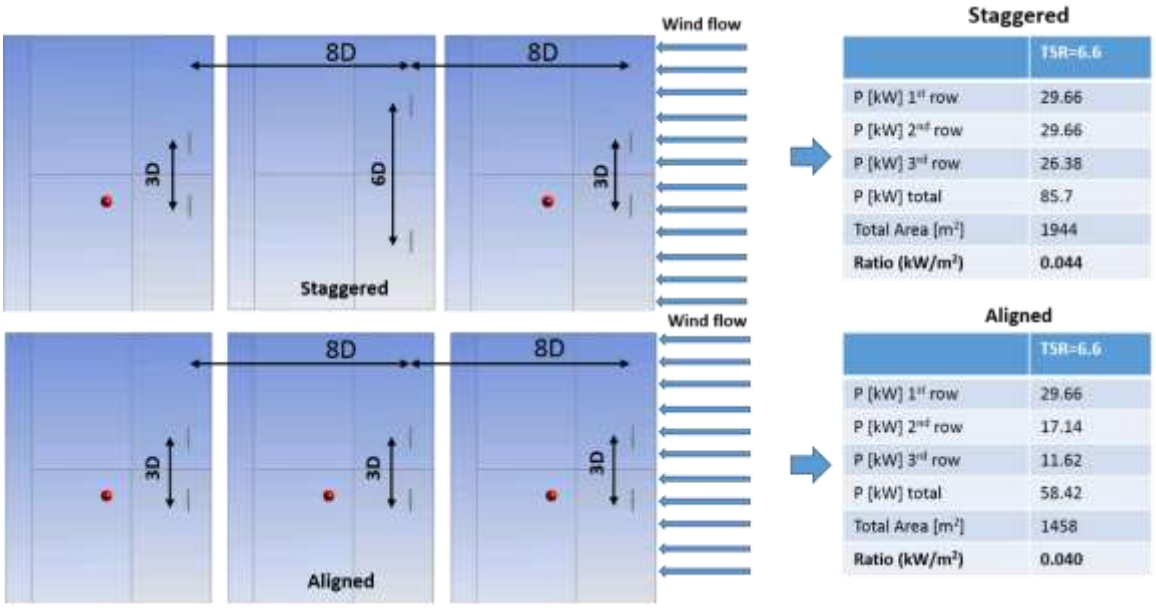

Staggered

	TSR=6.6
P [kW] 1st row	29.66
P [kW] 2nd row	29.66
P [kW] 3rd row	26.38
P [kW] total	85.7
Total Area [m²]	1944
Ratio (kW/m²)	**0.044**

Aligned

	TSR=6.6
P [kW] 1st row	29.66
P [kW] 2nd row	17.14
P [kW] 3rd row	11.62
P [kW] total	58.42
Total Area [m²]	1458
Ratio (kW/m²)	**0.040**

Figure 4.9 - Comparison between staggered and aligned configurations.

As discussed in the previous paragraph, staggering a wind turbine row from upstream rotors increases the available power by avoiding exposure to downstream rows to wake effects from upstream rotors. The velocity and TI contours of Fig. 4.10 show a second row staggered away from the wake of the first row, producing more output power but occupying more area of land. The Fig. 4.10 shows a third row in which the rotors are experiencing the combined wake effects from the first and second rows. The rotors are positioned in the same position of the rotors from the first row, aiming to stagger the third row away from the second row affected area. Another option of staggering would be to position the rotors in the third row away from the wake affected area, which would require moving them further away this way dramatically increasing the area of land occupied by the wind farm.

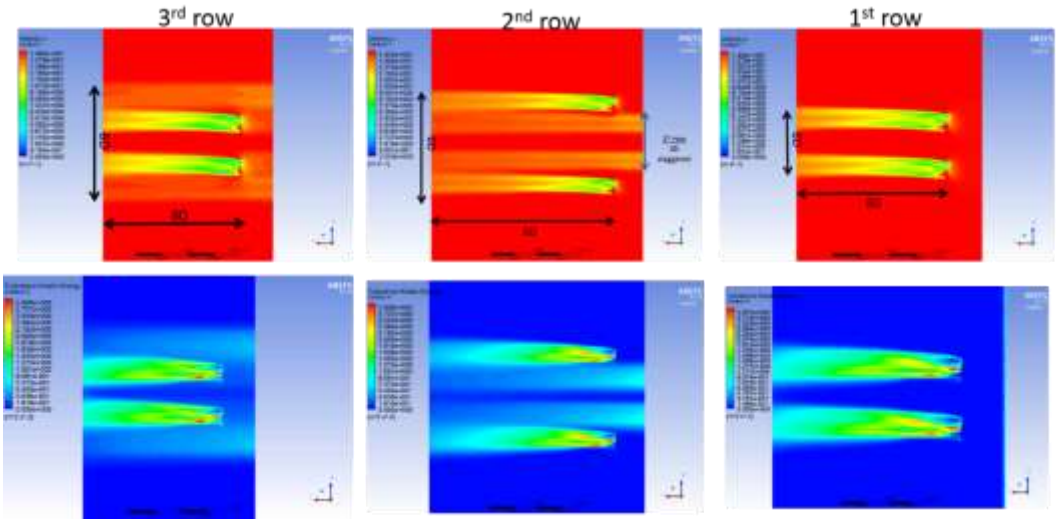

Figure 4.10 – Velocity and Turbulence Intensity Contours.

4.3.2 Control Strategies

Analytical methods do not quantify wake characteristics according to instantaneous operating conditions. The CFD model implemented in this work is capable of evaluating wake velocity according to TSR and Pitch Angle conditions. Table 4.1 shows how wake velocity decreases as the TSR increases, which is explained by the fact that the rotor is extracting more energy from the incident wind. The difference becomes much more significant when it comes to available wind power, for instance a downstream position at 8D would have 9.27% more available wind power for TSR=4 in comparison to TSR=6.6. Moreover, the influence of the spacing between rows can be very significant and influence the total wind farm output power. In order to help doing this analysis, Fig. 4.11 shows velocity contours showing several downstream positions in the wake. Considering upstream conditions for the first row of U=15ms-1 and TSR=6.6, a comparison in terms of the output power shows that P_{8D}/P_{7D}=1.02, P_{8D}/P_{6D}=1.04, and P_{8D}/P_{5D}=1.06.

Table 4.1 - Comparison of velocity values at several downstream positions

TSR	U_{5D} [m.s^{-1}]	U_{6D} [m.s^{-1}]	U_{7D} [m.s^{-1}]	U_{8D} [m.s^{-1}]
4	13.385	13.19	13.14	13.07
6.6	13	12.65	12.25	11.87

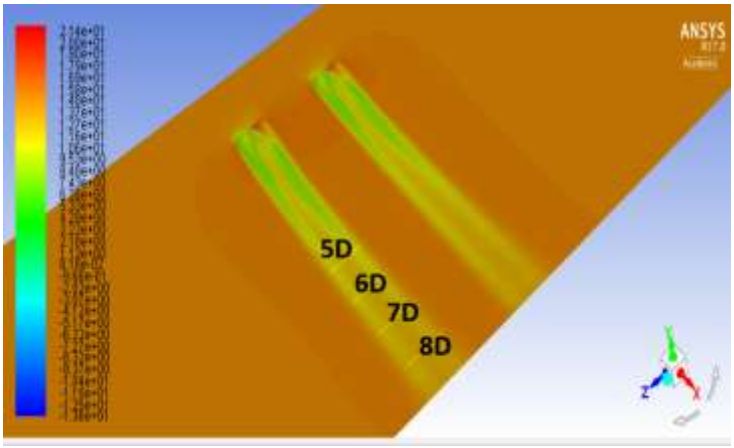

Figure 4.11 – Velocity contours at the wake, showing several downstream positions in the wake.

The introduction section of this chapter showed some of the benefits that could be possible achieved on the total output power by controlling the rotational speed of a specific row of turbines. Therefore, the final part of this research focused on analyzing two different cases to approach the effect of rotational speed control on the total output power. In the first case, we compare two design configuration. For the first case, we compare two configurations under the same free-stream velocity conditions of 15m/s: 1) rpm control: the 1st row of turbine have a slightly reduced rotational speed (424.5rpm), and all the other are forced to have 510 rpm. 2) no rpm control: the three rows of turbines are kept with the same rotational speed of 510 rpm. The results of Table 4.2 show that rpm control resulted in a 4.63% in the total output power. Basically, a reduced rotational speed in the first row (by using rpm control) resulted in increased velocity in the wake of the 1st row. Thus, the

second row of turbines experienced increased incident wake, and the extra output power production in the second row compensates (and overcomes) the total output power in comparison with no rpm control configuration. The second case of study is shown at Table 4.2, and this time considering the same free-stream velocity of 15m/s but 424.5rpm for all the rows. The controlled configuration has a reduced rotational speed of 318rpm in the 1st row. In this case, the rpm control strategy resulted in 2.52% increase in the total output power.

Table 4.2 - Cases study for rpm control strategy and staggered configurations.

	P [kW] 1st row	P [kW] 2nd row	P [kW] 3rd row	Total P [kW]	Area [m²]	kW/m²
rpm control (case 1)	29.66	16.84	7.64	54.14	1458	0.037
No rpm control (case 1)	31.12	12.92	7.71	51.74	1458	0.0355
rpm control (case 2)	25.66	21.64	12.84	59.9	1458	0.041
No rpm control (case 2)	29.66	17.14	11.62	58.42	1458	0.04
Staggered	29.66	29.66	26.38	85.7	1944	0.044

4.4 Discussion

In this work, the first improvements on the objective function achieved by the optimization routine is in the order of 6.63%. The level of improvement is similar to the levels found in literature. For instance, the study carried out by Park et al[12] considering the offshore Horns Rev 1 wind farm achieved an increase on the wind farm power efficiency from 83.6% to 89.8% by slightly shifting the turbines from their initial location. Moreover, the idea in this work of setting the lateral and downstream spacing between rows as the design parameters to vary in the optimization routine was inspired by the findings by Stevens et al[15] and Meyers[16]. Stevens[15] found that the distance of 10 diameters (or higher) between wind turbine rows would minimize the cost per unit of energy production, and

Meyers[16] found that the current wind farms layout solutions in literature have characteristics with considerably lower spacing than computationally optimized layout solutions. In the current work, two of the iterations attempted by the sqp optimization algorithm during the optimization routine to minimize the objective function were related to changing the downstream distance between the first and second rows with a 0.5D value, and the other one changing the same mentioned distance but between the second and third rows again with half diameter. The objective function value evaluated at the mentioned points were 1.762 and 1.7395, respectively, showing that changing the downstream distance from the first and second rows resulted in a better contribution to improve the objective function. Moreover, the effect of varying the lateral spacing between turbines is much more significant and expected, since basically the same torque would be produced by quite different areas. The objective function would vary from 1.42 for 3D lateral spacing, and 0.714 when considering 6D. This leads to the obvious conclusion that the best solution to maximize torque produced over the area is to keep the turbines as close as possible in terms of the lateral spacing. In regards to the downstream distance between rows, the analysis is more complex but the findings of this work supports the idea that the distance between the first and second rows have a more significant impact compared with the distance between the second and third rows. A similar result was found by the study conducted by Son et al[13], in which the distance between the first and second rows was found to have a more significant impact on the objective function (defined by cost over output power) compared with the distance between the fourth and fifth rows. The sqp algorithm implemented in this work attempted to vary each individual rotor position laterally, but no benefits were found to improve the objective function. Although the output

power varies when individual rotors laterally change position, the ratio of output power over the area remains the same or becomes worst in comparison with the totally aligned position simulate in this work (which was set as initial guess).

Optimized operation strategies (OOS) through individual selection of operating point have been demonstrated to be more efficient than Conventional Operation Strategies (COS), in which each individual rotor is set to operate in its maximum performance. The basic idea of OOS is to select individual operating point for each rotor so that the whole wind power plant production is maximized rather than each individual rotor. In this work, the two cases of study from section 4.3.2 showed achieved 4.63% and 2.52%, respectively, on the output power. Because both configurations were in the same area (control and no control), this represents improvements for use of land. These results were consistent with data from literature. Some examples in literature showed benefits on reducing output power from upstream turbines to enhance the whole farm output power due to the effect of increasing the amount of available power for downstream rotors. For instance, the optimization of Pitch Angle performed by Lee[19] resulted in 4.5% improvement, whereas the optimization of both the TSR and Pitch Angle performed by González[18] resulted in 7.55%. Other studies have found similar ranges of improvement in the percentage of total produced output power. Kazda[20] achieved 2.5% increase in the sum of the upstream and downstream turbines by applying sub-optimal operation for the upstream rotor, which was set to operate with a 12.5% reduction in output power production. Gil[21] achieved up to 6.24% in energy captured by using sub-optimal operating points. These examples show that benefits of controlling wake conditions should be explored in the future, opening new

possibilities of control strategies to suggest better solutions for the wind farm optimization problem.

In regards to the dimensions tested in this work (6D x 8D configuration), there is no well stablished universal standards for wind farm for these dimensions. For instance, typical dense arrays in California have up to 6 to 7 hectares (15 to 18 acres) per megawatt of installed capacity, while typical European wind farms generally occupy 13 to 20 hectares (30 to 50 acres) per megawatt of installed capacity[121]. A map showing the placement and the location of all wind turbines in USA can be found in the literature[131], and it is clear and easy to recognize that there neither standardized spacing distance between the turbines nor are the layouts predominantly symmetrical. Moreover, several other parameters must be taken into consideration when discussing the use of land in wind farms, which can cause some uncertainty to the level of improvement of 10% achieved in this work. Major land use issues include actual land required per energy output or capacity per unit of land area; the amount of land disturbed by a wind farm; non-exclusive land use and compatibility; rural preservation; turbine density; access roads and erosion or dust emission. Some other land use issues include government regulations and permitting (zoning, building permits, and approval of aviation authorities), others include public acceptance[121].

Furthermore, wind energy systems have been limited to areas with consistent wind resources over a long period of time. In USA, the development of wind farms has occurred primarily on open areas or rural fields. These areas are often used for agriculture, recreation, scenic areas, wild life habitat, and forest management. Wind farm facilities in USA may occupy only 3-5% of the total acreage, leaving the rest available for other uses. European wind farms are more efficient in that regards, usually occupying 1-3% of the

land. In UK, 1% of the land is typically covered by turbines and access roads. Farm lands (crops) are cultivated up to the base of the tower, and temporary roads are designed for heavier equipment when needed. Examples of variables that may determine land use impacts include site topography; size, number, output, and spacing of turbines; location and design of the roads; location of supporting facilities; location of electrical lines[121].

Actions for mitigating land use in wind farms include the use of equipment with minimal structural support; electrical lines placed underground; maintenance off-site; consolidating equipment on the turbine tower or foundation pad; consolidating structures within a wind farm area; requiring use of more efficient or larger turbines; optimize turbine spacing to reduce density; roadless construction; restricting most vehicle travel to existing access roads; limiting number of new access roads; and avoiding and minimizing cut and fill. Permitting agencies usually evaluate cost associated with a particular strategy; type and level of impact; land use-objectives of the community; significance of any potential land-use inconsistency or incompatibility; and available alternatives[121].

A geological map from USGS[131] shows that some wind farms may have more than 4 rows of turbines, and the typical range found in that map shows a typical range within 4 to 7 turbines. In this work, the effect of only 4 rows of turbines was considered for exploring better layout designs. In the staggered configuration, the third row experiences the wake effects from the first row, and the fourth row experiences wake effects from the second row. The spacing between these rows (1^{st} and 3^{rd}, and 2^{nd} and 4^{th}) is large enough to dissipate wake effects, meaning that there is no significant velocity deficit from wake effects. The spacing between the 2^{nd} and 4^{th} rows as well as the spacing between 2^{nd} and 4^{th} is large enough to allow the velocity to almost recover its free-stream value, and the

same would be true for eventual additional staggered rows. For aligned designs, this work simulated the effect of 4 rows, which is reasonably enough to reflect the range found in wind farms. Each new additional row could potentially influence the ratio kW/m^2 of the whole wind farm, however some of the examples showed in the literature review showed that the most significant effects are found in the first rows of turbines (citation). The majority of the manuscripts in literature considered three up to five rows of turbines.

In regards to the achievements of this work, additional sources of uncertainties can be pointed out. For instance, The uncertainty of the level of improvement achieved by the staggered configuration (10%) can be related to: 1) operational conditions implemented: the level of improvement is variable according to the instantaneous operational conditions (rpm, wind speed); 2) type of turbine: different types of turbine can vary the level of the aerodynamic performance, however wake characteristics are not significantly influenced by blade geometry at larger downstream distances.

4.5 Conclusions

In this work, the use of land in wind farms was improved in 10% as section 4.3.1 shows. Remarkable conclusions refer to the use of staggering: it is possible to have a significant improvement on the use of land and output power production by staggering the second row. The staggered configuration achieved 10% improvement compared with an aligned configuration, both of them working under the same operational conditions. Additionally, control strategies can result in benefits for the wind farm: two cases of study showed improvements within 2.52% and 4.63% in the output power. This improvement was achieved by controlling the rotational speed of the first row. A slight reduction in the

first row of turbines increases the production of the second row, which will have incident winds under increased wake velocities.

Chapter 5: A CFD Mesoscale Model for Wind Farms

Abstract

Mesoscale models (or limited area models) can be used in forecasting mode to produce short-term predictions of the weather. The High-Resolution Rapid Refresh (HRRR) is a real-time 3km resolution hourly updated atmospheric model. The model utilizes radar data assimilated every 15 minutes over one hour period adding further details to the one provided by 13km hourly assimilation radar enhanced Rapid Refresh (RAP). The Atmospheric Boundary Layer (ABL) modeling for wind farms is important to determine the effect of site conditions in a short or medium term, and analyzing the effect of wake interaction. The variation of the horizontal wind speed with height above the ground is called the vertical wind shear. In wind engineering, the determination of vertical wind shear is an important design parameter because it directly determines the productivity of a wind turbine on a certain height, and it can strongly influence the lifetime of turbine blades. The objective of this work is to analyze how ABL conditions can influence wind turbine wake characteristics such as velocity decay and turbulence intensity. In order to do that, the wake of a wind turbine was modeled using CFD (Computational Fluid Dynamics) taking into account ABL effects such as vertical velocity gradients (wind shear) and velocity fluctuations. Simulations were performed considering atmospheric neutral stability conditions and meteorological data for a summer day with extremely unstable conditions.

5.1 Introduction

Wind Assessment Modeling (WAM) is especially important to predict how the variability of local wind conditions affect wind farm performance. While climate modeling allows the assessment of scales in the order of 105 m resolution for domains of 107 m, mesoscale modeling is an existing tool to predict regional climate and atmospheric boundary layer conditions. Microscale modeling is applicable to wind farms for numerical modeling of wind turbine arrays, allowing evaluation of the power losses and the effect of the array on the useful lifetime of the turbine components. The Atmospheric Boundary Layer (ABL) modeling for wind farms is important to determine the effect of site conditions in a short or medium term, and analyzing the effect of wake interaction. Numerical Weather Prediction (NWP) models are applicable for characterization of regional wind climate[119, 120]. Computational fluid dynamics (CFD) can be coupled with NWP mesoscale models to analyze and predict mesoscale or microscale effects of a specific wind condition.

The atmospheric boundary layer, also known as the planetary boundary layer, is the lowest part of the atmosphere and its characteristics are directly influenced by contact with the earth's surface. Physical quantities such as velocity, temperature and relative humidity can change rapidly in space and time. The variation of the horizontal wind speed with height above the ground is called the vertical wind shear. In wind engineering, the determination of vertical wind shear is an important design parameter because it directly determines the productivity of a wind turbine on a certain height, and it can strongly influence the lifetime of turbine blades. Stability of the ABL is the tendency to resist vertical motion or to suppress existing turbulence. The stability of the ABL is a determining

factor for the vertical wind shear experienced in the first few hundred meters above the ground. Atmospheric stability is classified as stable, neutrally stable, or unstable. The stability of the earth's atmosphere is governed by the vertical temperature distribution resulting from the radiative heating or cooling of its surface and the subsequent convective mixing of the air adjacent to the surface[121].

Mesoscale models (or limited area models) can be used in forecasting mode to produce short-term predictions of the weather, or in historical integration mode using decades of data with reanalysis to characterize long term wind climate. Microscale models are tools for the design space for wind energy developers, considering wind farm layout, topographical site conditions, and typically 10-20km horizontally. The mesoscale to microscale chain includes approximations of the governing equations, physical subsystems, incorporate large-scale meteorological, topographic and wind data and apply for the boundaries, parametrization of sub grid physics, and numerical implementation and solution methods. The ECMWF - WRF (Weather Research Forecast) model is the most widely use open source mesoscale model. Another mesoscale model is the High-Resolution Rapid Refresh (HRRR) [120]. The HRRR is a real-time 3km resolution hourly updated atmospheric model. The model utilizes radar data assimilated every 15 minutes over one hour period adding further details to the one provided by 13km hourly assimilation radar enhanced Rapid Refresh (RAP). RAP is a NOAA (National Oceanic and Atmospheric Administration) hourly updated modeling system (operational at NCEP) that covers North America. The system is comprised of a numerical forecast model and an analysis system to initialize the model, and RAP is complemented by the 3km HRRR model [122]. Accurate CFD simulations of ABL flow over complex terrains are essential for optimization of wind

farm micro-siting effects[123]. ABL modeling techniques include Low Fidelity Models and High Fidelity Models. Low Fidelity Models consider stronger assumptions in the numerical modeling approach, and usually has lower computational cost and eventually lower performance compared to high fidelity models. High Fidelity Models predict the variability of the wind conditions solving microscale turbulence and mesoscale fluctuations[120]. Reynolds Averaged Navier-Stokes (RANS) simulations have been widely used in literature to models wind turbine wake models with the advantage of low computational cost in comparison with transient models, but steady state simulations do not account for velocity fluctuations. Transient unsteady models such as Large-Eddy Simulation (LES) can account velocity fluctuations by setting perturbation components by Reynolds-stress components. This is important to model the fluctuations inherently present at the atmospheric wind, and several studies have developed LES models to simulate wind turbines operating in the ABL[124-129]. A full review of LES simulations of wind farm aerodynamics can be found in literature[4]. According to Rodrigo et al[2], challenges for ABL modeling include relation between enhanced mixing in operational models, role of land surface heterogeneity, development of LES models with interactive land-surface, and climatology of boundary-layer parameters such as stability.

5.1.1 Objectives and Scope of the Work

The objective of this work is to analyze how ABL conditions can influence wind turbine wake characteristics such as velocity decay and turbulence intensity. In order to do that, the wake of a wind turbine was modeled taking into account ABL effects such as vertical velocity gradients (wind shear) and velocity fluctuations. Simulations were performed considering atmospheric neutral stability conditions and meteorological data for

a summer day with extremely unstable conditions. The neutral conditions were approximated using the wind log-law equation, which are an approximation for the vertical velocity gradient, while the extremely unstable conditions were implemented using meteorological data from the mesoscale model HRRR.

5.2 Material and Methods

5.2.1 ABL Modeling

The ABL was modeled using a Log-Law wind profile and the mesoscale model HRRR, and the two different approaches implemented in this work were compared in terms of wake velocity decay. Section 5.2.1.1 explains the Log-Law profile assumptions and define the relevant equations, and section 5.2.1.2 provides a detailed overview of the methodology implemented for the HRRR mesoscale model.

5.2.1.1 Log-Law Wind Profile

Wind shear influences both the assessment of wind resources and the design of wind turbines. In wind energy studies, two mathematical models or laws have generally been used to model the vertical profile of wind speed over regions of homogeneous flat terrain (e.g., fields, deserts, and prairies). The first approach is the log-law, which is based on a combination of theoretical and empirical research. The second approach is the power law. Eq. 5.1 is the standard way to calculate a Log-Law Wind profile as a function of vertical height and surface roughness. The log-law plot of Fig.5.1 was done using Eq.1 assuming neutral stability conditions (α=0.17) and z0=0.1m.

$$U(z) = \frac{u^*}{k} ln \frac{z}{z0} \tag{5.1}$$

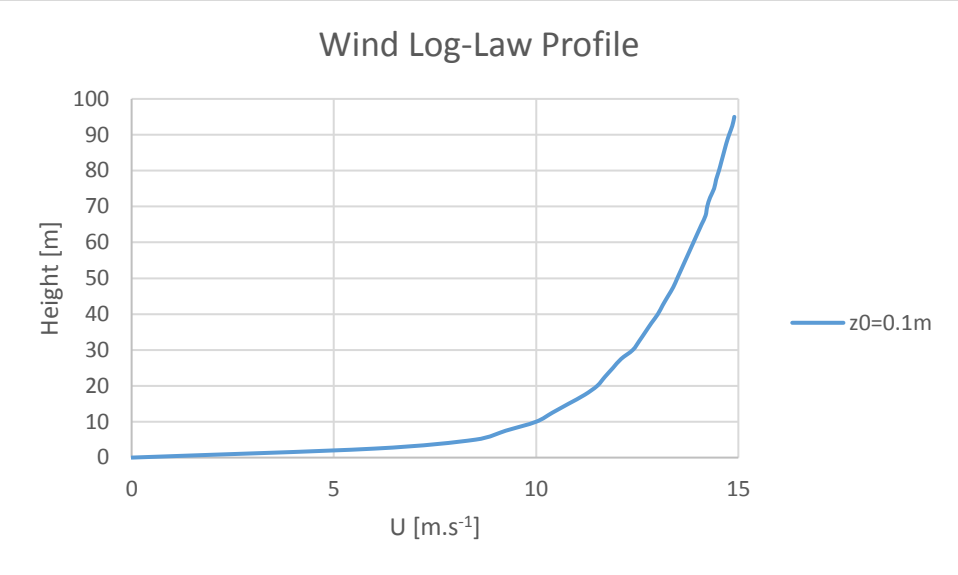

Figure 5.1 – Log-Law wind profile.

5.2.1.2 HRRR (Mesoscale Model)

In this work, the High-Resolution Rapid Refresh (HRRR) [4] model was implemented to derive the velocity flow field under different atmospheric conditions. The location of the simulated data in this work corresponds to the same location of the Lamar wind farm in Colorado State, and the range of data considered for the simulation was a summer day (07/01/2015). Fig. 5.2 shows the profile simulated in this work corresponding to an extremely unstable day (nocturnal jet), and the curve fit to create a wind speed function that varies with the vertical height z. The HRRR data were interpreted and queried to derive the extremely unstable wind profile. A polynomial function was utilized to generate a wind profile for the inlet of the CFD model.

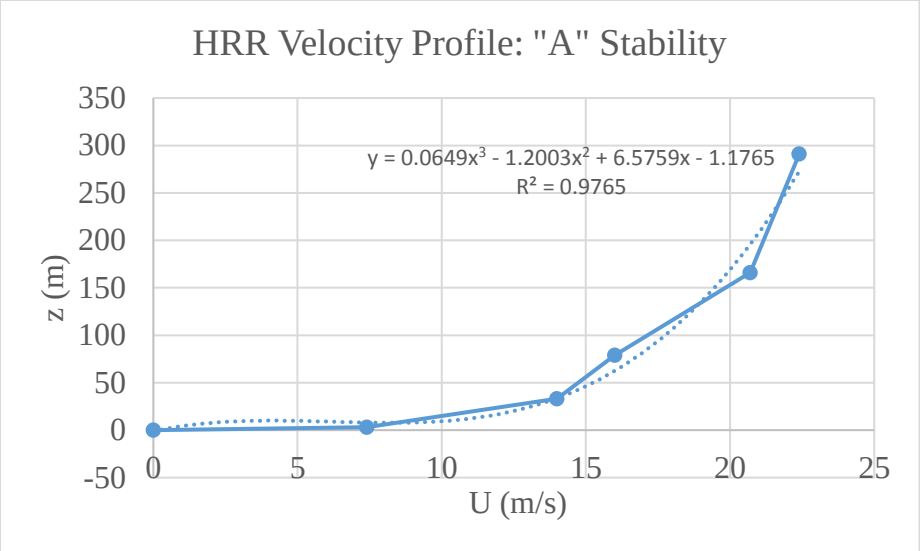

Figure 5.2 – Polynomial function to fit wind profile using HRRR model for a summer day with extremely unstable conditions, corresponding to very turbulent and fast wind speed (nocturnal jet).

5.2.2 Wind Turbine Wake CFD Model

In this work, a RANS model was implemented aiming to check the wake velocity behavior for different inlet profile conditions including a log law, a mesoscale HRRR, and a constant velocity inlet. Additionally, a transient CFD model was implemented using a LES turbulence model to characterize wake unsteady behavior under wind velocity fluctuations. The goal of the transient simulation is to qualitatively compare velocity contours for wind turbine wakes under steady state (RANS model, no fluctuations) and unsteady transient (LES CFD model with fluctuations) conditions. By running a transient CFD model, it is possible to verify how velocity fluctuations inherently present in the atmospheric wind can influence wake shape and development.

5.2.2.1 RANS Steady-Steady Simulation

The computational physical domain and the boundaries applied for the RANS model were previously implemented to simulate the MEXICO rotor in previous works[117, 118] in the context of developing a computational tool based on a steady state RANS model to optimize wind farm layout and land use (Fig.5.3). Pressure-far-field boundaries are applied for the lateral and superior boundaries (which requires the larger exterior rectangle to achieve convergence), pressure-outlet for the exit and a no-slip walls for the inferior boundary and the blades. A detailed overview of the mesh sizing is found in Fig. 5.4. The strategy for meshing the physical domain is to build a sphere of influence surrounding each rotor, and break the physical domain into smaller rectangles defining them as the same part in ANSYS Design Modeler. The sphere of influence option allows for a better convergence of the flow field solution. The smaller rectangles allow the mesh element sizing of the near and far wake to be controlled locally, avoiding gradients in the mesh sizing in the interface of each sub-domain.

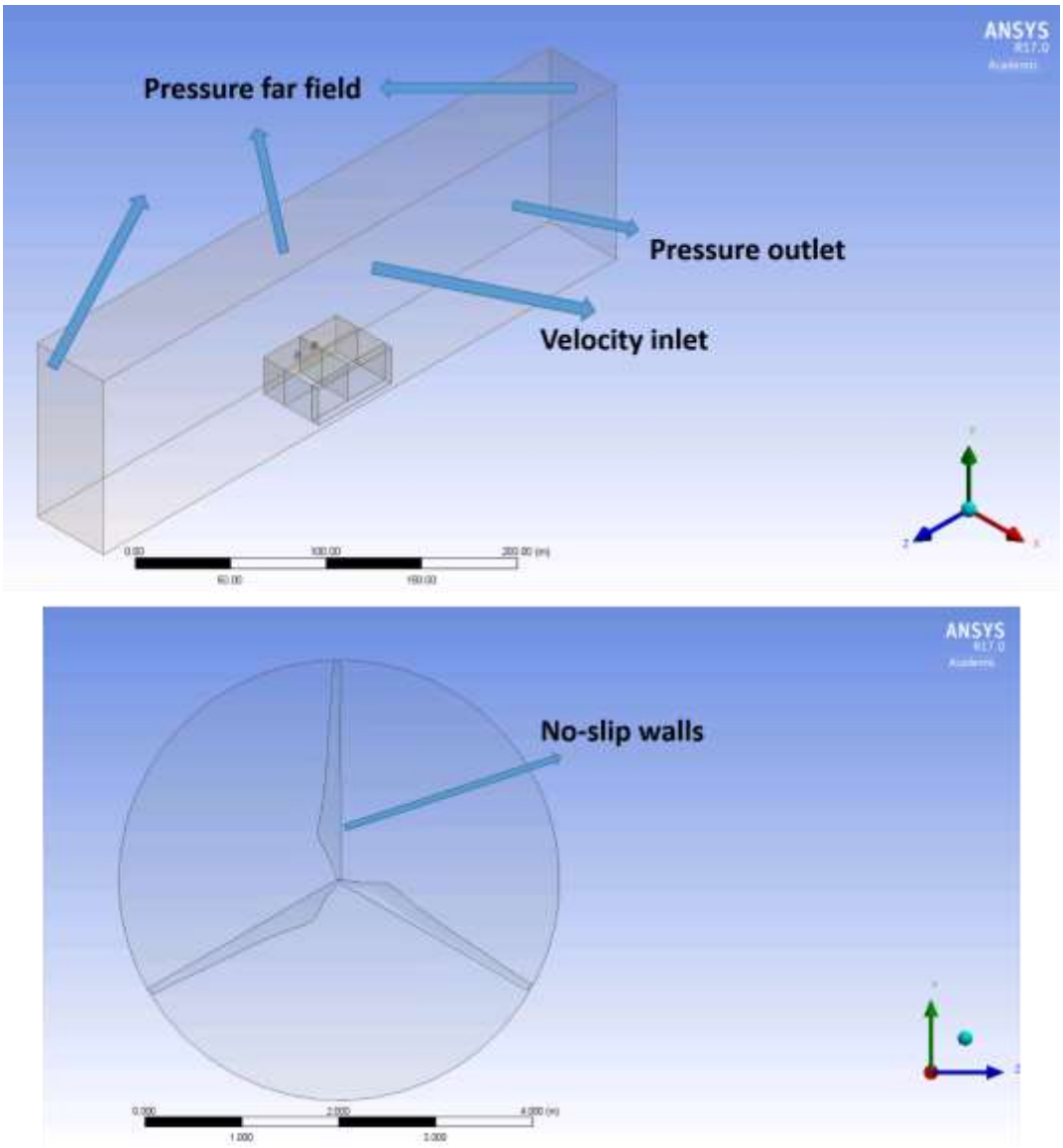

Figure 5.3 – Physical domain implemented for the RANS steady state model.

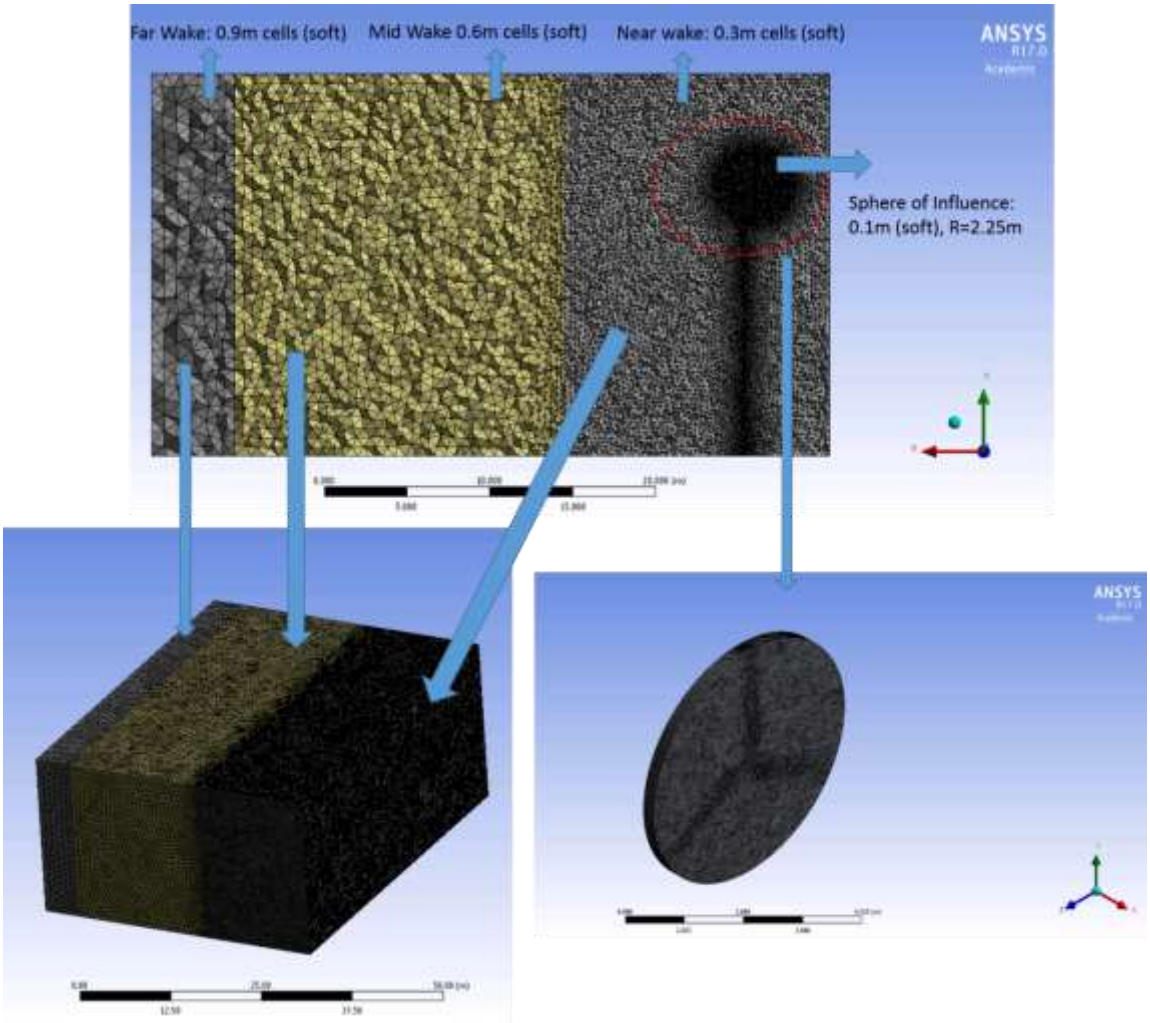

Figure 5.4 – Detailed overview of the mesh sizing procedure.

The flow field solution is determined using the CFD solver ANSYS Fluent17, and two computers with 64GB RAM/ 8 processers for each machine with the processor Intel Xeon CPU E5-1620 v2 3.7GHz. The computational time for each simulation was approximately 10 hours. The simulation was performed using a steady state Moving Reference Frame (MRF) approach, which is a type of steady state approach also known as the frozen rotor approach. In the MRF approach, only the frame rotates instead of the body

itself. The turbulence model selected was the k-ω SST, which is suitable for swirl flow, and it was used in the literature studies as their main turbulence modelling technique.

5.2.2.2 Large Eddy Simulation (LES)

5.2.2.2.1 Velocity Fluctuations

LES models have the capabilities to account the influence of inlet fluctuations in the fluid flow. The perturbations can be modeled in two different ways: 1) Vortex Method; and 2) Spectral Synthesizer. The Spectral Synthesizer is a method for synthetically generating turbulence for inlets by introducing stochastic components of the flow at the velocity-specified inlet boundaries. In ANSYS Fluent, this is performed through the selection of Reynolds-stress components uu, vv, ww, uv, uw, and vw. The Vortex Method is a methodology similar to the Spectral Synthesizer, but only the components uu, vv and ww are introduced in the inlet. In this work, the Vortex Method was implemented in the velocity-inlet profile in ANSYS Fluent aiming to check the effect of velocity fluctuations on the wind turbine wake profile. The default value of $1m^2/s^2$ for the Reynolds-stress components uu, vv and ww was implemented in this simulation. The stress components were first determined using the default values from Fluent ($uu=vv=ww=1m^2/s^2$). Then, a sensitivity analysis was performed, followed by a visual inspection of the velocity contours to confirm if each generated perturbed profiles can reasonably reflects typical atmospheric conditions. The default values of the Reynolds stress components produced perturbations consistent with velocity fluctuations found in atmospheric field conditions. When the Reynolds stress components are too high, there are excessive fluctuations because the profile becomes too much turbulent. On the other hand, low values of Reynolds stress components do not even produce fluctuations to the inlet.

5.2.2.2.2 Layout of the Physical Domain and Boundary Conditions

The layout of the physical domain and the boundary conditions implemented in ANSYS Fluent for the LES model are shown in Fig.5.5, which is smaller than the layout of Fig. 5.3 and only comprises one turbine with no tower. The reduction in the physical domain sizing and the deletion of the tower were performed to reduce the computational expenses, since RANS models require less computational resources in comparison with LES models. Moreover, the lateral boundaries of the physical domain were switched to walls with null shear components. This was performed because pressure-far-field would require a larger physical domain to keep the lateral boundaries with a straight streamline so that the solution could achieve convergence. Alternatively, periodic boundaries or symmetry could have been implemented instead the null shear walls resulting in the same solution. The same mesh sizing setup implemented for the RANS model was implemented for the LES model, except that only one turbine was simulated. The LES simulation implemented in this work utilizes the RANS steady state solution as the initial guess, and then the Sliding Mesh procedure is setup to run a transient simulation. A total of 28,600 time steps of 0.005 seconds were completed to account for a total of 6 seconds of simulation. The rotational speed implemented was 220 rpm, and the velocity at the hub height was 6 $m.s^{-1}$. The computational time for the transient simulation was approximately 170 hours.

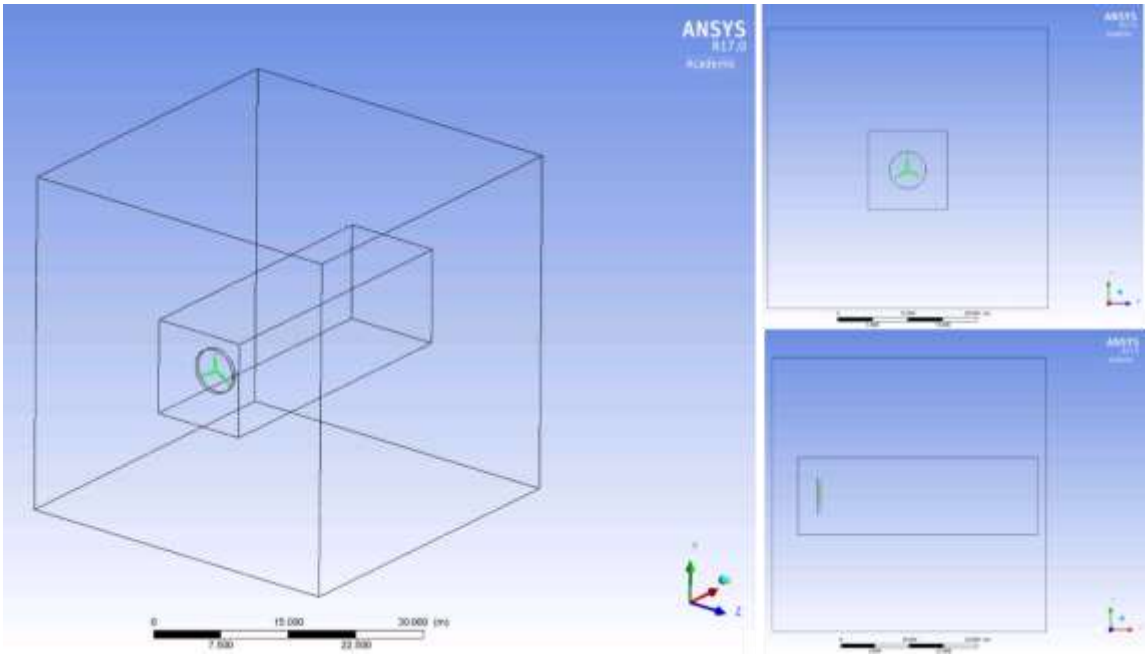

Figure 5.5 – Layout of the physical domain and boundary conditions implemented in the CFD Solver.

5.3 Results

5.3.1 Wake Profile Comparison

A comparison between different inlet profiles is shown in Fig. 5.6, where the left panel shows a lateral view of the wake and the right panel shows a top view. The rotor rotational speed implemented in these simulations were ω=220rpm, and the rotor hub height was 16.25m. The choice for a λ=5.2 is related to the fact that this value is typically found in commercially operating wind farms. The wake profile for an inlet with a log-law wind profile with U=10m.s^{-1} at H=10m and surface roughness z0=0.1m is shown in Fig. 5.6. In the left side, the velocity varies in the vertical direction according to the log-law, reaching a velocity of U=11m.s^{-1} at the hub height. Fig. 5.6 also shows a simulation for a constant velocity inlet profile assuming U=11m.s^{-1}, this way allowing a comparison

between the wake profile for the log law and the constant inlet profile. The wind profile obtained from the queried HRRR mesoscale model for a summer day (07.01.2015) at Lamar location (described in section 2.1.2) with extremely unstable conditions (Fig. 5.2) is shown in Fig. 5.6. The hub velocity is approximately the same of the other profiles configuration ($U=11m.s^{-1}$). Comparing the wake profiles for the three simulations, the wake velocity decay is almost coincident similar for the Log-Law and the constant velocity inlet (Fig. 5.7). The HRRR model shows a slightly lower velocity deficit of approximately 10% in both the horizontal (radial traverse) and the vertical direction. This means that the wake under the very unstable atmospheric profile resulted in the smallest wake decay, but the difference was more significant in the radial (or horizontal) direction than the vertical. Even though the differences between the profiles are small, this could mean considerable power losses in the context of a whole wind farm.

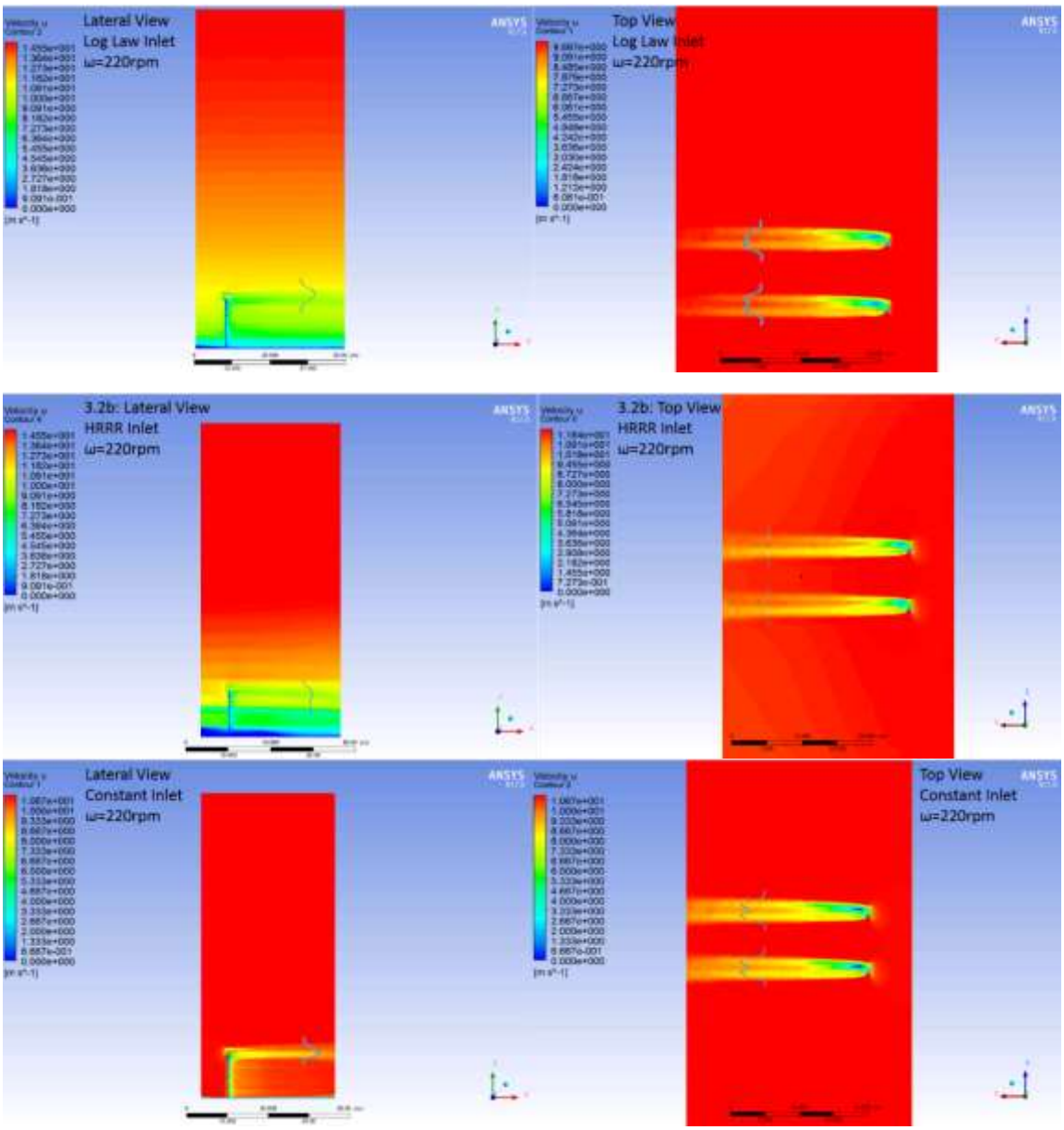

Figure 5.6 – Wake Velocity Contours for a Log-Law wind profile, a mesoscale model (HRRR) inlet profile and a constant velocity inlet profile.

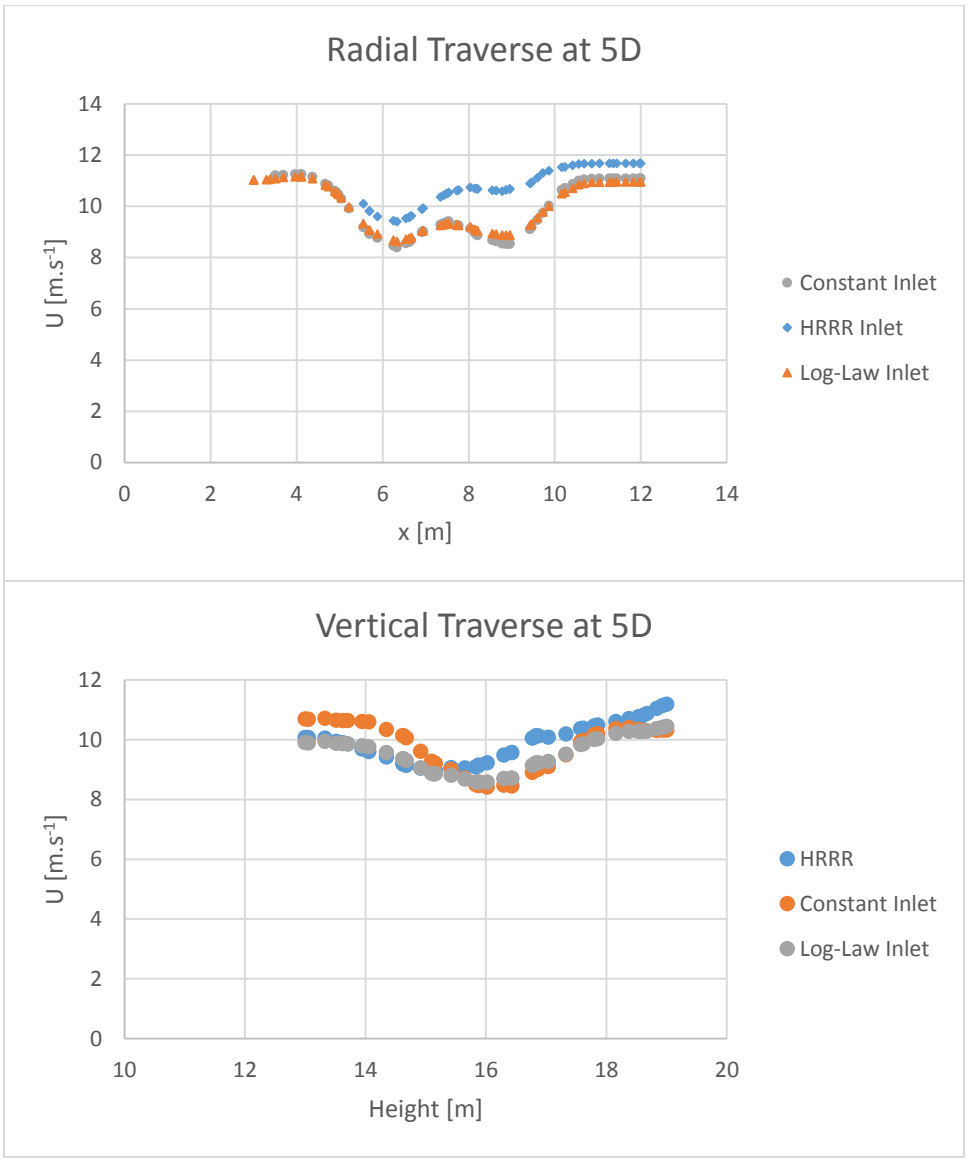

Figure 5.7 – Velocity decay for the different inlet profiles simulated using the RANS model.

5.3.2 Wake Profile Comparison: Constant Inlet vs Perturbed Inlet

Fig. 5.8 shows wake velocity contours for a wind profile with variable velocity in the vertical direction. The simulation considered a LES model with perturbation using the vortex method and setting perturbations by using Reynolds stress components for uu, vv and ww directions. The perturbations were created to simulate velocity fluctuations present

in atmospheric conditions, aiming to check the effect of such fluctuations on the wake profile. Additionally, Fig. 5.8 shows the differences in regards to wake behavior between an inlet profile not perturbed (constant velocity) and a perturbed inlet profile. The lateral view shows a velocity profile varying in the vertical direction, while the top view shows a plane at the hub height with a constant velocity at that height. The non perturbed case shows an axysimmetric wake, while oscilations and fluctuations are present for the perturbed case. In despite of that, the ammount of velocity deficit remains similar for both approaches. The main difference is related to the direction in which the wakes are going to develop: the non perturbed wake develops straight forward behind the turbine, while the wake under perturbed inlet seems to assume a meandering that is guiding its direction.

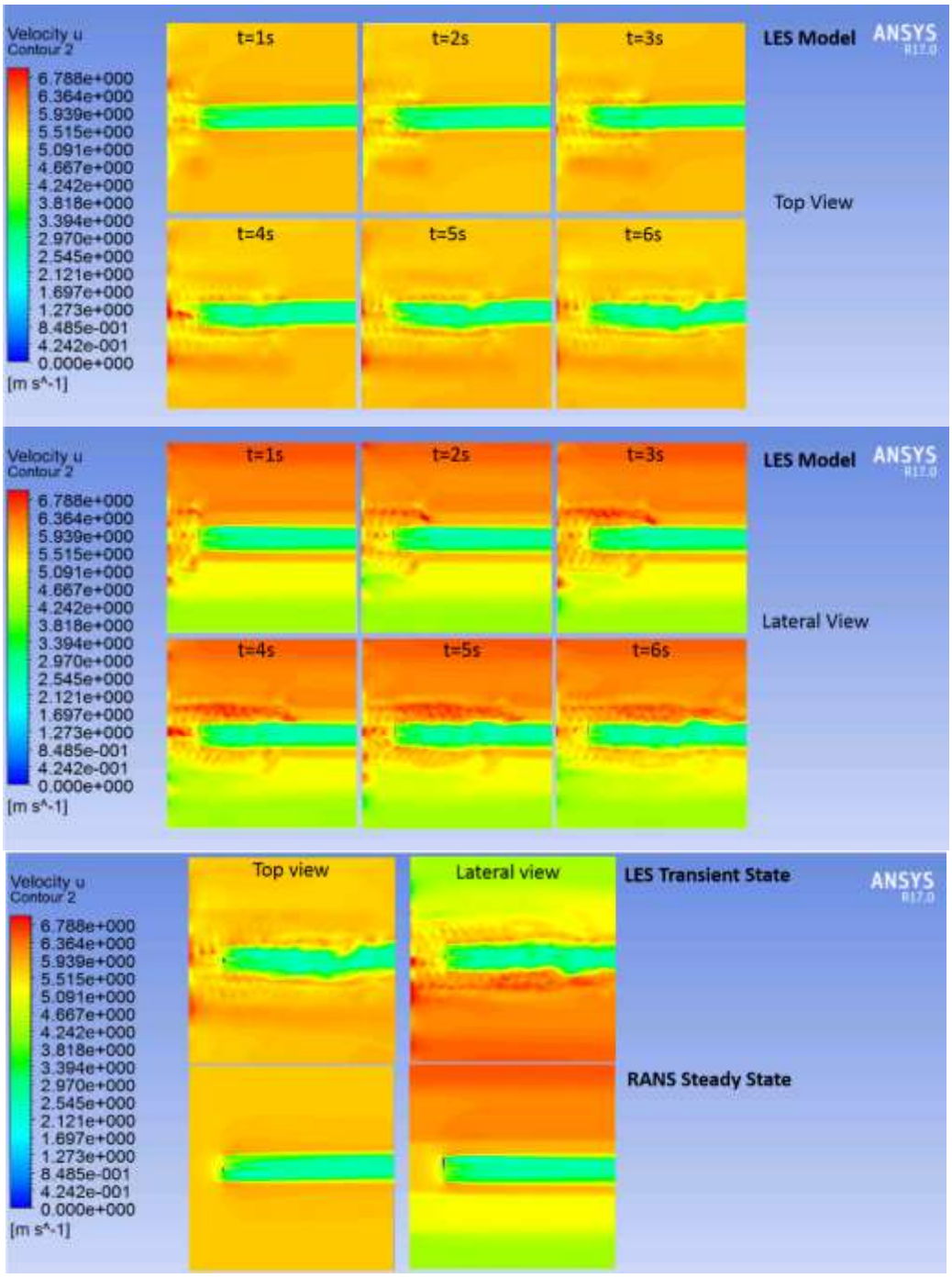

Figure 5.8 – Wake velocity contours showing the transient (LES model) evolution in the vertical and horizontal direction, and comparison between perturbed inlet and constant velocity inlet showing different shapes for the wake.

5.4 Discussion

The LES model implemented in this work utilized the vortex method to introduce perturbations by Reynolds stress components uu, vv and ww, this way generating atmospheric turbulence to simulate velocity fluctuations. LES models have been widely applied to wind turbine wakes models. For instance, Nilson et al.[128] generated the atmospheric turbulence using the synthetic turbulence model of Mann using LES simulations, finding good agreement with measurements for the Lillgrund wind farm. Rodrigo et al.[120] argues that only high-fidelity models such as LES can characterize the turbulent aerodynamic behavior of wind turbine wakes interaction. On the other hand, Moriarty et al.[13] presented an comprehensive analysis of data from both steady and unsteady CFD wake models, showing that there is no winner between unsteady and steady state CFD models in regards to accuracy because the level of errors found in literature significantly varies, and there is no relationship with the implemented approach. More importantly, Moriarty et al[130] reinforces the need for more precise and delineated observations of wind farms under different operating and atmospheric conditions. This approach would achieve better validation data compared to data averaged over long periods of time, helping to quantify uncertainties and the most useful quantities for model validation. In the case of the transient simulation performed in this present work, the wake slightly deviated from the standard straight way that the steady wake develops. This meandering in the wake has been studied by other authors in literature, and the Wake Meandering Model (WMM) has been studied in literature for some researchers. This change of wake direction may have consequences on wind farm layout optimization, since

the wake region with the greatest ammounts of velocity deficit and turbulence intensity slightly deviates from the standard straight way right behind the turbine.

5.5 Conclusions

At the heights analyzed here in this work, the use of different velocity inlet profiles did not results in significant changes to the wake of the wind turbine. The velocity deficit remained approximately the same for the three approaches (log law, HRRR and constant inlet) implemented in this work. The vertical wind shear might be more significant at higher altitude and for greater wind turbine diameters, therefore future research could scale the same CFD model implemented in this work to explore the effect of higher altitudes and greater diameters on the wake development. In regards to the LES model, the results showed similar results for the velocity deficit but the main difference was in the direction of propagation of the wake. The wake seems to deviate from the standard straight way of development when the perturbations from the LES simulation are introduced in the model. Future work should explore the development of the wake under velocity fluctuations.

Chapter 6: Conclusions

In the first study (chapter 2) of this dissertation, a computational system was designed to analyze and optimize the operational conditions of a wind turbine and the flow field surrounding the rotor wake region. The model was validated against near wake velocity data, and the level of agreement is very similar in comparison to other studies found in literature. The CFD simulation demonstrated that the TSR and the Pitch Angle greatly influence the near wake behavior, affecting the velocity deficit and the turbulence intensity profile in this region.

From this first model, a second model (study 2 or chapter 3) was developed to analyze the far wake aerodynamics behavior. The second study demonstrated that the TSR critically influences the far wake aerodynamics behavior, but the same is not true for the Pitch Angle. Additionally, an extensive comprehensive review on CFD models revealed the main gap in literature: although there are many CFD models for wind turbines, there is a lack of CFD models to simulate the whole wind farm. Most studies focus on single turbine modeling, and there is need for more technological development in this area. In this sense, this work provided a novel contribution to the literature: a method to evaluate wind farm rows by using the outlet from previous simulation. Such technique can provide significant advances in wind farm modeling techniques using CFD models. At the end of the second study, a computational tool was developed to tackle the wind farm layout optimization problem.

In study 3 (chapter 4), the use of land in wind farms was improved by 10% using staggered configurations. The study concludes that it is possible to have a significant improvement on the use of land and output power production by staggering the second row of turbines away from the wake effects from the first row. The staggered configuration achieved 10% improvement in the use of land compared with an aligned configuration, both of them working under the same operational conditions. Additionally, control strategies can result in benefits for the wind farm: two cases of study showed improvements between 2.52% and 4.63% in the output power. This improvement was achieved by controlling the rotational speed of the turbine blades in the first row. A slight reduction in the first row of turbines increases the production of the second row, which will have incident winds under increased wake velocities. This shows the importance of developing better control techniques, and more possibilities can be studied in a near future.

The last study (study 4 or chapter 5) implemented different inlet velocity profiles to evaluate the impact of vertical wind shear on wake profiles. At the heights analyzed, different velocity inlet profiles did not result in significant changes to the wake of the wind turbines. The velocity deficit remained approximately the same for the three approaches (log law, HRRR and constant inlet) implemented in this work. The vertical wind shear might be more significant at higher altitudes and for greater wind turbine diameters, therefore future research could scale the same CFD model implemented in this work to explore the effect of higher altitudes and greater diameters on the wake development. A transient model based on LES theory showed that there can be changes in the direction of propagation of the wake when velocity fluctuations are introduced to the model. The wake seems to deviate from the standard straight way of development/propagation when the

perturbations from the LES simulation are introduced in the model. Future work should explore the development of the wake under velocity fluctuations.

In regards to the influence of the number of cells on the computational time and accuracy of the results, the Appendix D shows how the size of the cells influence the results of the wake flow field. When the number of cells go beyond 10 million, it is extremely difficult to obtain results in a reasonable amount of time. The results from Appendix D do not show a great influence on the results when the number of cells increase from 10 million to 20 million cells, however the computational time considerably increases. The Appendix D also shows that the results are relatively influenced when increasing the number of cells from 4 million to 10 million cells. The level of influence is within 10%, which could have produced margin of error beyond the improvement achieved at the chapter 4 (study 3). This is why we did not use 4 million cells instead of 10 million, otherwise a considerable reduction on the computational time could be achieved.

References

[1] GWEC - GLOBAL WIND ENERGY COUNCIL. **Global Wind Report: Annual Market Update 2016.** May 2016. Available in:< http://gwec.net/publications/global-wind-report-2/>. Access in Nov. 8th 2016.

[2] P. M. Pardalos et al. (eds.), **Handbook of Wind Power Systems, Energy Systems,** DOI: 10.1007/978-3-642-41080-2_2, Springer-Verlag Berlin Heidelberg 2013.

[3] A. Crespo, J. Hernández, S. Frandsen. Survey of Modelling Methods for Wind Turbine Wakes and Wind Farms, **Wind Energy**, v.2, p.1-24, Madrid (Spain), 1999.

[4] D. Mehta, A.H. van Zuijlen, B. Koren, J. G. Holierhoek, H. Bijl. Large Eddy Simulation of wind farm aerodynamics: A review, **Journal of Wind Engineering and Industrial Aerodynamics**, v.133, p. 1-17, The Netherlands, 2014.

[5] Spera, D.A.. **Wind Turbine Technology:** Fundamental concepts of wind turbine engineering, 2nd ed., ASME PRESS, 2009. 835p.

[6] M. S. Adamarola, P. –A. Krogstad. Experimental investigation of wake effects on wind turbine performance, **Renewable Energy**, v.36, p. 2078-2086, Trondheim (Norway), 2011.

[7] Ammonit – Measuring wind and solar power. Available in https://www.ammonit.com Accessed in 11/02/2015.

[8] IEC – INTERNATIONAL ELETROTECHNICAL COMISSION. **IEC 61400-12-1:** Power Performance measurements of electricity producing wind turbines, Edition 1.0, Switzerland, 2005, 101p.

[9] NASA – National Aeronautics and Space Administration. Available in http://www.nasa.gov/ Accessed in 11/02/2015.

[10] NREL – NATIONAL RENEWABLE ENERGY LABORATORY.. Unsteady Aerodynamics Experiment Phases II–IV Test Configurations and Available Data Campaigns. **Technical Report**, Jul. 1999, 177p.

[11] J.G. Schepers, K. Boorsma, T. Cho, S. Gomez-Iradi, P. Schaffarczyk, A. Jeromin, W.Z. Shen, T. Lutz, K.Meister, B. Stoevesandt, S. Schreck, D. Micallef, R. Pereira, T. Sant, H.A. Madsen, N. Sorensen. Final Report of IEA Task 29, Mexnet (Phase 1): Analysis of Mexico Wind Tunnel Measurements, Technical Report, 312p., Netherlands, 2012.

[12] Jinkyoo Park, Kincho H. Law. Layout optimization for maximizing wind farm power production using sequential convex programming, **Applied Energy**, v.151, p.320-334, USA, 2015.

[13] Eunkuk Son, Seungmin Lee, Byeongho Hwang, Soogab Lee. Characteristics of turbine spacing in a wind farm using an optimal design process, **Renewable Energy**, v.65, p.245-249, Republic of Korea, 2014.

[14] Yu-Ting Wu, Fernando Porté-Agel. Simulation of Turbulent Flow Inside and Above Wind Farms: Model Validation and Layout Effects, **Boundary-Layer Meteorology**, v.146, p.181-205, Switzerland, 2012.a

[15] Richard J. A. M. Stevens, Benjamin F. Hobbs, André Ramos, Charles Meneveau. Combining economic and fluid dynamic models to determine the optimal spacing in very large wind farms, **Wind Energy**, v.20, p.466-477, The Netherlands, 2017.

[16] Johan Meyers, Charles Meneveau. Optimal turbine spacing in fully developed wind farm boundary layers, **Wind Energy**, v.15, p.305-317, Belgium, 2012.

[17] Jinkyoo Park, Kincho H. Law. A data-driven, cooperative wind farm control to maximize the total production, **Applied Energy**, v.165, p.151-165, USA, 2016.

[18] Javier Serrano González, Manuel Burgos Payán, Jesús Riquelme Santos, Ángel Gaspar González Rodríguez. Maximizing the overall production of wind farms by setting the individual operating point of wind turbines. **Renewable Energy**, v.80, 219-229, Spain, 2015.

[19] Jaejoon Lee, Eunkuk Son, Byungho Hwang, Soogab Lee. Blade pitch angle control for aerodynamic performance optimization of a wind farm, **Renewable Energy**, v.54, p.124-130, Republic of Korea, 2013.

[20] J. Kazda, M. Zendehbad, S. Jafari, N. Chokani, R. S. Abhari. Mitigating adverse wake effects in a wind farm using non-optimum operational conditions, **Journal of Wind Engineering and Industrial Aerodynamics**, v.154, p.76-83, Switzerland, 2016.

[21] Mikel De-Prada-Gil, César Guillén Alías, Oriol Gomis-Bellmunt, Andreas Sumper. Maximum wind power plant generation by reducing the wake effect. **Energy Conversion and Management**, v.101, p.73-84, Spain, 2015.

[22] Souma Chowdhurry, Jie Zhang Messac, Luciano Castillo. Unrestricted wind farm layout optimization (UWFLO): Investigating key factors influencing the maximum power generation, **Renewable Energy**, v.38, p.16-30, United States, 2012.

[23] M. S. Adamarola, P. –A. Krogstad. Experimental investigation of wake effects on wind turbine performance, **Renewable Energy**, v.36, p. 2078-2086, Trondheim (Norway), 2011.

[24] L.P. Chamorro, F. Porté-Agel. A Wind-Tunnel Investigation of Wind-Turbine Wakes: Boundary-Layer Turbulence Effects, **Boundary-Layer Meteorology**, v.132, p. 129-149, Monnesota (USA), 2009.

[25] Jang-Oh Mo, Amanullah Choudhry, Maziar Arjomandi, Young-Ho Lee. Large eddy simulation of the wind turbine wake characteristics in the numerical wind tunnel model, **Journal of Wind Engineering and Industrial Aerodynamics**, v. 112, p. 11-24, Australia, 2013.

[26] D. Sturge, D. Sobotta, R. Howell, A. While, J. Lou. A hybrid actuator disc – Full rotor CFD methodology for modelling the effects of wind turbine wake interactions on performance, **Renewable Energy**, v. 80, p. 525-537, Sheffield (UK), 2015.

[27] H. Sarlak, C. Meneaveau, J.N. Sorensen. Role of subgrid-scal modeling in large eddy simulation of wind turbine wake interactions, **Renewable Energy**, v.77, p. 386-399, Denmark, 2015.

[28] M. Z. Houssain, H. Hirahara, Y. Nonomura, M. Kawahashi. The wake structure in a 2D grid installation of the horizontal axis micro wind turbines, **Renewable Energy**, v. 32, p. 2247-2267, Japan, 2007.

[29] L. J. Vermeer, J. N. Sorensen, A. Crespo. Wind turbine wake aerodynamics. **Progress in Aerospace Sciences**, v. 39, p. 467-510, The Netherlands, 2003.

[30] D. Medici and P. H. Alfredsson. Measurements on a Wind Turbine Wake: 3D Effects and Bluff Body Vortex Shedding, **Wind Energy**, v. 9, p. 219-236, Stockholm (Sweden), 2006.

[31] P. -Å. Krogstadl, J. A. Lund. An experimental and numerical study of the performance of a model turbine, **Wind Energy**, 2011, v. 15, p. 443-457, Norway, 2011.

[32] B. Sanderse, S. P. van der Pijl, B. Koren. Review of computational fluid dynamics for wind turbine wake aerodynamics, **Wind Energy**, v. 14, p. 799-819, The Netherlands, 2011.

[33] Nina Zhou, Ju Chen, Douglas E. Adams, Sanford Fleeter. Influence of inflow conditions on turbine loading and wake structures predicted by large eddy simulations using exact geometry, **Wind Energy**, p.803-824, United States, 2016.

[34] Ming-Chen Hsu, Ido Akkerman, Yuri Bazilevs. Finite element simulation of wind turbine aerodynamics: validation study using NREL Phase VI experiment, **Wind Energy**, v.17, p.461-481, United States, 2014.

[35] Chris Gundling, Jay Sitaraman, Beatrice Roget, Pierangelo Masarati. Application and validation of incrementally complex models for wind turbine aerodynamics, isolated

wind turbine in uniform inflow conditions, **Wind Energy**, v.18, p.1893-1916, United States, 2015.

[36] Jang-Oh Mo, Amanullah Choudhry, Maziar Arjomandi, Richard Kelso, Young-Ho Lee. Effects of wind speed changes on wake instability of a wind turbine in a virtual wind tunnel using large eddy simulation, **Journal of Wind Engineering and Industrial Aerodynamics**, v.117, p.38-56, Australia, 2013.

[37] Amanullah Choudhry, Jang-Oh Mo, Maziar Arjomandi, Richard Kelso. Effects of wake interaction on Downstream wind turbines, **Wind Engineering**, v.38, p.535-548, Australia, 2014.

[38] Hua Yang, Wen Zhong Shen, Jens Norkaer Sorensen, Wei Jun Zhu. Extraction of airfoil data using PIV and pressure measurements, **Wind Energy,** v.14, p.539-556, China, 2011.

[39] Wang Xudong, Wen Zhong Shen, Chen Jin. Shape optimization of wind turbine blades, **Wind Energy**, v.12, p.781-803, China, 2009.

[40] Bechmann, N. N. Sørensen and F. Zahle. CFD simulations of the MEXICO rotor, **Wind Energy**, v.14, p.677-689, Denmark, 2011. DOI: 10.1002/we.450

[41] Daniel Micallef, Gerard van Bussel, Carlos Simão Ferreira, Tonio Sant. An investigation of radial velocities for a horizontal axis wind turbine in axial and yawed flows, **Wind Energy**, v.16, p.529-544, Netherlands, 2012.

[42] M. Carrión, R. Steijl, M. Woodgate, G. Barakos, X. Munduate, S. Gomez-Iradi. Computational fluid dynamics analysis of the wake behind the MEXICO rotor in axial flow conditions, **Wind Energy**, v.18, p.1023-1045, Liverpool, 2015.

[43] I.Herraez, W.Medjroubi, B.Stoevesandt, J.Peinke. Aerodynamic Simulation of the MEXICO Rotor, **Journal of Physics: Conference Series,** 555 (2014) p.012051, Germany, 2012. doi:10.1088/1742-6596/555/1/012051.

[44] Wen Zhong Shen, Wei Jun Zhu and Jens Nørkær Sørensen. Actuator line/Navier–Stokes computations for the MEXICO rotor: comparison with detailed measurements, **Wind Energy**, v.15, p.811-825, Denmark, 2012.

[45] Néstor Ramos-García, Mads Mølholm Hejlesen, Jens Nørkær Sørensen and Jens Honoré Walther. Hybrid vortex simulations of wind turbines using a three-dimensional viscous-inviscid panel method, **Wind Energy**, v.20, p.1871-1889, Denmark, 2017

[46] Karl Nilsson, Wen Z. Shen, Jens N. Sørensen, Simon-Philippe Breton and Stefan Ivanell. Validation of the actuator line method using near wake measurements of the MEXICO rotor, **Wind Energy**, v.18, p.499-514, Sweden, 2015.

[47] A. Wimshurst and R. H. J. Willden. Extracting lift and drag polars from blade-resolved computational fluid dynamics for use in actuator line modelling of horizontal axis turbines, **Wind Energy**, v.20, p.815-833, UK, 2017.

[48] Hongmin Zhong, Pingan Du, Fangning Tang, Li Wang. Lagrangian dynamic large-eddy simulation of wind turbine near wakes combined with an actuator line method, **Applied Energy**, 144 (2015) 224-233, China.

[49] Srinivas Guntur, Niels N. Sørensen. A study on rotational augmentation using CFD analysis of flow in the inboard region of the MEXICO rotor blades, **Wind Energy**, v.18, p.745-756, Denmark, 2015.

[50] Niels N. Sorensen, A. Bechmann, P-E. Rethore, F. Zahle. Near wake Reynolds-averaged Navier-Stokes predictions of the wake behind the MEXICO rotor in axial and yawed flow conditions, **Wind Energy**, v.17, p.75-86, Denmark, 2012.

[51] Christina Tsalicoglou, Samira Jafari, Ndaona Chokani, Reza S. Abhari. RANS Computations of MEXICO Rotor in Uniform and Yawed Inflow, **Journal of Engineering for Gas Turbines and Power**, v.136, p.1-8, Zurich.

[52] F. Grasso, A. van Garrel. Near Wake Simulation of Mexico rotor in Axial and Yawed Flow Conditions with Lifting Line Free Wake Code, **Wake Conference**, Sweden, 2011. Ok

[53] Wen Zhong Shen, Wei Jun Zhu, Hua Yang. Validation of the Actuator Line Model for Simulating Flows past Yawed Wind Turbine Rotors, **Journal of Power and Energy Engineering**, 3: 7-13, Denmark, 2015.

[54] Réthoré, P-E. M., Zahle, F., Sørensen, N. N., & Bechmann, A. (2011). CFD Simulations of the Mexico Wind Tunnel and Wind Turbine. In Proceedings European Wind Energy Association (EWEA).

[55] Per-Åge Krogstad, Muyiwa S. Adaramola. Performance and near wake measurements of a model horizontal axis wind turbine, **Wind Energy, v.**15, p.743–756, Norway, 2012.

[56] P. Hashemi Tari, K. Siddiqui, H. Hangan. Flow characterization in the near-wake region of a horizontal axis wind turbine, **Wind Energy**, v.19, p.1249-1267, Canada, 2016.

[57] Michael Shives, Curran Crawford. Adaped two-equation turbulence closures for actuator disk RANS simulations of wind & tidal turbine wakes, **Renewable Energy**, v.92, p.273-292, Canada, 2016.

[58] Leonardo P. Chamorro, R. E. A Arndt and F. Sotiropoulos. Reynolds number dependence of turbulence statistics in the wake of wind turbines, **Wind Energy**, v.15, p.733-712, United States, 2012.

[59] Shengbai Xie and Cristina Archer. Self-similarity and turbulence characteristics of wind turbine wakes via large-eddy simulation, **Wind Energy**, v.18, p.1815-1838, United States, 2015.

[60] Nina Zhou, Jun Chen, Douglas E. Adams, Sanford Fleeter. Influence of inflow conditions on turbine loading and wake structures predicted by large eddy simulations using exact geometry, **Wind Energy**, v.19, p.803-824, United States, 2016.

[61] Helen Markou, Peter Bjørn Andersen and Gunner Chr. Larsen. Potential load reductions on megawatt turbines exposed to wakes using individual-pitch wake compensator and trailing-edge flaps, **Wind Energy**, v.14, p.841-857, 2011, Denmark.

[62] S.K. Kanev F.J. Savenije W.P. Engels. Active wake control: An approach to optimize the lifetime operation of wind farms, **Wind Energy**, p.1-14, 2018, The Netherlands.

[63] Rabia Shakoor, Mohammad Yusri Hassan, Abdur Raheem, and Yuan-Kang Wu. Wake effect modeling: A review of wind farm layout optimization using Jensen's model, **Renewable and Sustainable Energy Reviews**, v.58, p.1048-1059, Malaysia, 2016.

[64] B. Sanderse, S. P. van der Pijl, B. Koren. Review of computational fluid dynamics for wind turbine wake aerodynamics, **Wind Energy**, v.14, p. 799-819, 2011.

[65] J.F. Ainslie. Calculating the flow field in the wake of wind turbines, **Journal of Wind Engineering and Industrial Aerodynamics**, v.27, p.213-224, The Netherlands, 1988.

[66] Niels Troldborg, Frederik Zahle, Puerre-Elouan Réthoré, Niels N. Sorensen. Comparison of wind turbine wake properties in non-sheared inflow predicted by different computational fluid dynamics rotors models, **Wind Energy**, v.18, p.1239-1250, Denmark, 2015.

[67] R. C. Storey, S. E. Norris, J. E. Cater. An actuator sector method for efficient transient wind turbine simulation, **Wind Energy,** v.18, p.699-711, New Zeland, 2015.

[68] Joseph Seydel and Alberto Aliseda. Wind turbine performance in shear flow and in the wake of another turbine through high fidelity numerical simulations with moving mesh technique, **Wind Energy, v.16, p.123-138, United States, 2013.**

[69] Pierre-Elouan Réthoré, Paul van der Laan, Niels Troldborg, Frederik Zahle, Niels N. Sørensen. Verification and validation of an actuator disc model, **Wind Energy**, v.17, p.919-937, Denmark, 2014.

[70] Joachim C. Heinz, Niels N. Sørensen, Frederik Zahle. Fluid–structure interaction computations for geometrically resolved rotor simulations using CFD, **Wind Energy**, v.19, p.2205-2221, Denmark, 2016.

[71] Weipao Miao, Chun Li, Giorgio Pavesi, Jun Yang, Xiaoyun Xie. Investigation of wake characteristics of a yawed HAWT and its impacts on the inline downstream wind turbine using unsteady CFD, **Journal of Wind Engineering and Industrial Aerodynamics**, v.168, p.60-71, China, 2017.

[72] Jordan M. Wilson, Cole J. Davis, Subhas K. Venayagamoorthy, Paul R. Heyliger. Comparisons of Horizontal-Axis Wind Turbine Wake Interaction Models, **Journal of Solar Energy Engineering**, v.137, p.3-8, United States, 2015.

[73] Miao Weipao, Li Chun, Yang Jun, Yang Yang, Xie Xiaoyun. Numerical Investigation of Wake Control Strategies for Maximizing the Power Generation of Wind Farm, **Journal of Solar Energy Engineering**, v.138, p. 034501-1 – p.034501-7, China, 2016.

[74] Chih-Hua Keni Wu, Vinh-Tan Nguyen. Aerodynamic simulations of offshore floating wind turbine in platform-induced pitching motion, **Wind Energy**, v.20, p.835-858, Singapore, 2017.

[75] Raf Theunissen, Paul Housley, Christian B. Allen and Charles Carey. Experimental verification of computational predictions in power generation variation with layout of offshore wind farms, **Wind Energy**, v.18, p.1739-1757, UK, 2015.

[76] Thanh Toan Tran, Dong-Hyun Kim, Ba Hieu Nguyen. Aerodynamic Interference Effect of Huge Wind Turbine Blades With Periodic Surge Motions Using Overset Grid-Based Computational Fluid Dynamics Approach, **Journal of Solar Energy Engineering,** v.137, p.061003-1 – p.061003-16, South Korea, 2015.

[77] Frederik Zahle, Niels N. Sorensen. Charactertization of the unsteady flow in the nacelle region of a modern wind turbine, **Wind Energy**, v.14, p.271-283, Denmark, 2011.

[78] Christoph Schulz, Patrick Letzgus, Thorsten Lutz, Ewald Krämer. CFD study on the impact of yawed inflow on loads, power and near wake of a generic wind turbine, **Wind Energy**, v.20, p.253-268, Germany, 2017.

[79] Sasan Sarmast, Antonio Segalini, Robert F. Mikkelsen, Stefan Ivanell. Comparison of the near-wake between actuator-line simulations and a simplified vortex model of a horizontal-axis wind turbine, **Wind Energy**, v.19, p.471-481, Denmark, 2016.

[80] J. M. Prospathopoulos, E. S. Politis, K. G. Rados, P. K. Chaviaropoulos. Evaluation of the effects of turbulence model enhancements on wind turbine wake predictions, **Wind Energy**, v.14, p.285-300, Greece, 2011.

[81] Anshul Mittal, Kidambi Sreenivas, Lafayette K. Taylor, Levi Hereth and Christopher B. Hilbert. Blade-resolved simulations of a model wind turbine: effect of temporal convergence, **Wind Energy**, v.19, p.1761-1783, Tennessee, 2016.

[82] M. Paul van der Laan, Mark C. Kelly, Niels N. Sørensen. A new k-epsilon model consistent with Monin–Obukhov similarity theory, **Wind Energy**, v.20, p.479-489, Denmark, 2017.

[83] M. Paul van der Laan, Niels N. Sørensen1, Pierre-Elouan Réthoré1, Jakob Mann1, Mark C. Kelly1, Niels Troldborg1, Kurt S. Hansen2 and Juan P. Murcia. The k-ε-fP model applied to wind farms, **Wind Energy,** v.18, p.2065-2084, Denmark, 2015.

[84] M. Paul van der Laan, Niels N. Sørensen1, Pierre-Elouan Réthoré1, Jakob Mann1, Mark C. Kelly1, Niels Troldborg1, Kurt S. Hansen2 and Juan P. Murcia. The k-ε-fP model applied to wind farms, **Wind Energy,** v.18, p.2065-2084, Denmark, 2015.

[85] Stefan Ivanell, Robert Mikkelsen, Jens N. Sørensen, Dan Henningson. Stability analysis of the tip vortices of a wind turbine, **Wind Energy**, v.13, p.705-715, Sweden, 2010.

[86] Stefan Ivanell, Jens N. Sørensen, Robert Mikkelsen, Dan Henningson. Analysis of Numerically Generated Wake Structures, **Wind Energy**, v.12, p.63-80, Sweden, 2009.

[87] Gunner C. Larsen, Antonio Crespo. Wind turbine wakes for wind energy, **Wind Energy**, v.14, p.797-798, 2011.

[88] Marc Bromm, Lukas Vollmer, Martin Kühn. Numerical investigation of wind turbine wake development in directionally sheared inflow, **Wind Energy**, v.20, p.381-395, Germany, 2017.

[89] Christian Masson, Arezki Smaïli. Numerical Study of Turbulent Flow around a Wind Turbine Nacelle, **Wind Energy**, v.9, p.281-298, Canada, 2006.

[90] R. C. Storey, S. E. Norris, K. A. Stol, J. E. Cater. Large eddy simulation of dynamically controlled wind turbines in an offshore environment, **Wind Energy**, v.16, p.845-864, New Zealand, 2013.

[91] Niels Troldborg, Jens N. Sorensen, Robert Mikkelsen. Numerical simulations of wake characteristics of a wind turbine in uniform inflow, **Wind Energy**, v.13, p.86-99, Denmark, 2010.

[92] Niels Troldborg, Gunner C. Larsen, Helge A. Madsen, Kurt S. Hansen, Jens N. Sørensen, Robert Mikkelsen. Numerical simulations of wake interaction between two wind turbines at various inflow conditions, **Wind Energy**, v.14, p.859-876, Denmark, 2011.

[93] Harish Gopalana, Christopher Gundlinga, Kevin Brown, Beatrice Roget, Jayanarayanan Sitaraman, Jefferey D. Mirocha, Wayne O. Miller. A coupled mesoscale–microscale framework for wind resource estimation and farm aerodynamics, **Journal of Wind Engineering and Industrial Aerodynamics**, v.132, p.13-26, United States, 2014.

[94] Nak Joon Choi, Sang Hyun Nam, Jong Hyun Jeong, Kyung Chun Kim. Numerical study on the horizontal axis turbines arrangement in a wind farm: Effect of separation distance on the turbine aerodynamic power output, **Journal of Wind Engineering and Industrial Aerodynamics**, v.117, p.11-17, Republic of Korea, 2013.

[95] Alexandros Makridis, John Chick. Validation of a CFD model of wind turbine wakes with terrain effects. **Journal of Wind Engineering and Industrial Aerodynamics**, v.123, p.12-29, United Kingdom, 2013.

[96] Ali M. AbdelSalam, Velraj Ramalingamn. Wake prediction of horizontal-axis wind turbine using full-rotor modeling, **Journal of Wind Engineering and Industrial Aerodynamics,** v.124, p.7-19, India, 2014.

[97] Ali M. Abdelsalam, K. Boopathi, S. Gomathinayagam, S.S. Hari Krishnan Kumar, Velraj Ramalingam. Experimental and numerical studies on the wake behavior of a horizontal axis wind turbine, **Journal of Wind Engineering and Industrial Aerodynamics**, v.128, p.54-65, India, 2014.

[98] Matthieu Boudreau, Guy Dumas. Comparison of the wake recovery of the axial-flow and cross-flow turbine concepts, **Journal of Wind Engineering and Industrial Aerodynamics,** v.165, p.137-152, Canada, 2017.

[99] Idriss Ammara, Christophe Leclerc, Christian Masson. A viscous three-dimensional differential/Actuator-Disk Method for the Aerodynamic Analysis of Wind Farms, **Journal of Solar Energy Engineering**, v.124, p.345-356, Canada, 2002.

[100] Edoardo Frau, Christian Kress, Ndaona Chokani, Reza S. Abhari. Comparison of Performance and Unsteady Loads of Multimegawatt Downwind and Upwind Turbines, **Journal of Solar Energy Engineering**, v.137, p. 041004-1 - 041004-8, Switzerland, 2015.

[101] Aaron Rosenberg, Anupam Sharma. A Prescribed-Wake Vortex Lattice Method for Preliminary Design of Co-Axial, Dual-Rotor Wind Turbines, **Journal of Solar Energy Engineering**, p.061002-1 – p. 061002-9, United States, 2016.

[102] Kidambi Sreenivas, Anshul Mittal, Levi Hereth, Lafayette K. Taylor, C. Bruce Hilbert. Numerical Simulation of the interaction between tandem wind turbines, **Journal**

of Wind Engineering and Industrial Aerodynamics, v.157, p/145-157, United States, 2016.

[103] V. Esfahanian, A. Salavati Pour, I. Harsini, A. Haghani, R. Pasandeh, A. Shahbazi, G. Ahmadi. Numerical analysis of flow field around NREL Phase II wind turbine by a hybrid CFD/BEM method, **Journal of Wind Engineering and Industrial Aerodynamics**, v.120, p.29-36, Iran, 2013.

[104] R. J. Barthelmie, K. Hansen, S. T. Frandsen, O. Rathmann, J. G. Schepers, W. Schlez, J. Phillips, K. Rados, A. Zervos, E. S. Politis, P. K. Chaviaropoulos. Modelling and measuring flow and wind turbine wakes in large wind farms offshore. **Wind Energy**, v.12, p. 431-444, United States, 2009.

[105] David Guirguis, David A. Romero, Cristina H. Amon. Toward efficient optimization of wind farm layouts: Utilizing exact gradient information, **Applied Energy**, v.179, p.110-123, Toronto, Canada, 2016.

[106] David Guirguis, David A. Romero, Cristina H. Amon. Gradient-based multidisciplinary design of wind farms with continuous-variable formulations, **Applied Energy**, v.197, p.279-291, Toronto, Canada, 2017.

[107] Ahmareza Vasel-Be-Hagh, Cristina L. Archer. Wind farm hub height optimization, **Applied Energy**, v.195, p.905-921, Delaware, USA, 2017.

[108] M Churchfield[1], Q Wang[1], A Scholbrock[1], T Herges[2], T Mikkelsen[3] and M Sj¨oholm[3]. **Using High-Fidelity Computational Fluid Dynamics to Help Design a Wind Turbine Wake Measurement Experiment.** 2016 The Science of Making Wind From Torque.

[109] Paul Fleming[1], Pieter M.O. Gebraad[2], Sang Lee[1], Jan-Willem van Wingerden[2], Kathryn Johnson[1], Matt Churchfield[1], John Michalakes[1], Philippe Spalart[3] and Patrick Moriarty[1]. Simulation comparison of wake mitigation control strategies for a two-turbine case, **Wind Energy**, v.18, p. 2135-2143, United States, 2015.

[110] Paul Fleming[1], Andrew Ning[1], Pieter M. O. Gebraad[2], Katherine Dykes[1]. Wind plant system engineering through optimization of layout and yaw control, **Wind Energy**, v.19, p.329-344, United States, 2016.

[111] P. M. O. Gebraad[1], F. W. Teeuwisse[1], J. W. van Wingerden[1], P. A. Fleming [2], S. D. Ruben[3], J. R. Marden[3] and L. Y. Pao[3]. Wind plant power optimization through yaw control using a parametric model for wake effects—a CFD simulation study, **Wind Energy**, v.19, p.95-114, United States, 2016.

[112] Pieter Gebraad[1], Jared J. Thomas[2], Andrew Ning[2], Paul Fleming [1] and Katherine Dykes[1]. Maximization of the annual energy production of wind power plants by

optimization of layout and yaw-based wake control, **Wind Energy**, v.20, p.97-107, United States, 2017.

[113] Hansen, M. O. L. **Aerodynamics of Wind Turbines**. 2nd ed., London: Earthscan, 2008. 181p.

[114] Bertagnolio, F., Sørensen, N. N., Johansen, J., & Fuglsang, P. (2001). Wind turbine airfoil catalogue. (Denmark. Forskningscenter Risoe. Risoe-R; No. 1280(EN)). Technical report, August 2001, 151p.

[115] Sederstrom, Donn R., "Methods and Implementation of Fluid-Structure Interaction Modeling into an Industry-Accepted Design Tool" (2016).Electronic Theses and Dissertations. 1197.

[116] Sederstrom, Donn, "Cavitation in Pharmaceutical Manufacturing and Shipping" (2013). Electronic Theses and Dissertations. 586.

[117] Rafael V. Rodrigues and Corinne Lengsfeld. "Development of a Computational System to Optimize Wind Farm Layout", 35th AIAA Applied Aerodynamics Conference, AIAA AVIATION Forum, (AIAA 2017-4212). https://doi.org/10.2514/6.2017-4212

[118] Rafael V. Rodrigues and Corinne Lengsfeld. "Automated Gradient-Based Optimization to Maximize Wind Farms Land-Use", 2018 Applied Aerodynamics Conference, AIAA AVIATION Forum, (AIAA 2018-3826) https://doi.org/10.2514/6.2018-3826

[119] Sultan Al-Yahyai, Yassine Charabi , Adel Gastli. Review of the use of Numerical Weather Prediction (NWP) Models for wind energy assessment, **Renewable and Sustainable Energy Reviews**, v.14, p.3192-3198, Oman, 2010.

[120] Javier Sanz Rodrigo, Roberto Aurelio Chávez Arroyo, Patrick Moriarty, Matthew Churchfield, Branko Kosovic, Pierre-Elouan Réthoré, Kurt Schaldemose Hansen, Andrea Hahmann, Jeffrey D. Mirocha and Daran Rife. Mesoscale to microscale wind farm flow modeling and evaluation**, WIREs Energy Environ** 2017, 6:e214. doi: 10.1002/wene.214.

[121] J. F. Manwell, J. F., J. McGowan, A. Rogers. Wind energy explained: theory, design, and application. 2nd ed., 677p. , 2009.

[122] EARTH SYSTEM RESEARCH LABORATORY – High Resolution Rapid Refresh. Available in https://rapidrefresh.noaa.gov/hrrr/

[123] Zhang, X. (2009). CFD simulation of neutral ABL flows. Roskilde: Danmarks Tekniske Universitet, Risø Nationallaboratoriet for Bæredygtig Energi. (Denmark. Forskningscenter Risoe. Risoe-R; No. 1688(EN)).

[124] Mahdi Abkar, Fernando Porté-Agel. The Effect of Free-Atmosphere Stratification on Boundary-Layer Flow and Power Output from Very Large Wind Farms, **Energies**, v.6, p.2338-2361, Switzerland, 2013. doi:10.3390/en6052338

[125] Cristina L. Archer, Sina Mirzaeisefat, Sang Lee. Quantifying the sensitivity of wind farm performance to array layout options using large-eddy simulation**, Geophysical Research Letters**, v. 40, p.4963–4970, United States, 2013. doi:10.1002/grl.50911

[126] Marc Calaf, Charles Meneaveau, Johan Meyers. Large eddy simulation study of fully developed wind-turbine array boundary layers, **Physics of Fluids** 22, 015110, Switzerland, 2010.

[127] Mirocha, J. D., Churchfield, M. J., Muñoz-Esparza, D., Rai, R. K., Feng, Y., Kosović, B., Haupt, S. E., Brown, B., Ennis, B. L., Draxl, C., Sanz Rodrigo, J., Shaw, W. J., Berg, L. K., Moriarty, P. J., Linn, R. R., Kotamarthi, V. R., Balakrishnan, R., Cline, J. W., Robinson, M. C., and Ananthan, S.: Large-eddy simulation sensitivities to variations of configuration and forcing parameters in canonical boundary-layer flows for wind energy applications, Wind Energ. Sci., 3, 589-613, https://doi.org/10.5194/wes-3-589-2018, 2018.

[128] Karl Nilsson, Stefan Ivanell, Kurt S. Hansen, Robert Mikkelsen, Jens N. Sørensen, Simon-Philippe Breton, Dan Henningson. Large-eddy simulations of the Lillgrund wind farm, **Wind Energy,** 18:449–467, Sweden, 2015.

[129] Yu- Ting Wu, Fernando Porté-Agel. Large-Eddy Simulation of Wind-Turbine Wakes: Evaluation of Turbine Parametrisations, **Boundary-Layer Meteorology**, v.138, p.345-366, Switzerland, 2011.

[130] Patrick Moriarty et al 2014 J. Phys.: Conf. Ser. 524 012185.

[131] USGS – United States Geological Survey: The US Wind Turbine Database. Available in <https://eerscmap.usgs.gov/uswtdb/viewer/#5.08/36.5/-98.23>.

Appendix A

Table A.1: Required velocity adjustment to promote Reynolds number similarity.

Vf [m/s]	Cf/Cp	Vp [m/s]	Vf [m/s]	Cf/Cp	Vp [m/s]	Vf [m/s]	Cf/Cp	Vp [m/s]
25	5	125	25	10	250	25	15	375
24	5	120	24	10	240	24	15	360
23	5	115	23	10	230	23	15	345
22	5	110	22	10	220	22	15	330
21	5	105	21	10	210	21	15	315
20	5	100	20	10	200	20	15	300
19	5	95	19	10	190	19	15	285
18	5	90	18	10	180	18	15	270
17	5	85	17	10	170	17	15	255
16	5	80	16	10	160	16	15	240
15	5	75	15	10	150	15	15	225
14	5	70	14	10	140	14	15	210
13	5	65	13	10	130	13	15	195
12	5	60	12	10	120	12	15	180
11	5	55	11	10	110	11	15	165
10	5	50	10	10	100	10	15	150
9	5	45	9	10	90	9	15	135
8	5	40	8	10	80	8	15	120
7	5	35	7	10	70	7	15	105
6	5	30	6	10	60	6	15	90
5	5	25	5	10	50	5	15	75
4	5	20	4	10	40	4	15	60
3	5	15	3	10	30	3	15	45

Table A.2: Blockage ratio as a function of the rotor diameter and the wind-tunnel dimensions.

LH (m)	LV (m)	Area LH*LV (m^2)	d prot (m)
5	7.5	37.5	2.19
6	9	54	2.62
7	10.5	73.5	3.06
8	12	96	3.50
9	13.5	121.5	3.93
10	15	150	4.37
11	16.5	181.5	4.81
12	18	216	5.24
13	19.5	253.5	5.68
14	21	294	6.12
15	22.5	337.5	6.56
16	24	384	6.99
17	25.5	433.5	7.43
18	27	486	7.87
19	28.5	541.5	8.30
20	30	600	8.74
21	31.5	661.5	9.18
22	33	726	9.61
23	34.5	793.5	10.05
24	36	864	10.49

Appendix B – Blade Element Theory Code

2nd iteration			Eq 6.7	Eq 6.8				Eq. 6.12	Eq. 6.13		Eq. 6.23	Eq. 6.24				
	r/R	c (r) [m]	ϕ	α (rad)	α (degrees)	Cl(α)	Cd(α)	Cn	Ct	σ	a	a'	Δα	Δa'	β	
DU91-W2-250	0.2	0.24	0.58752	0.273367	15.6628015	1.2	0.12	1.065297	0.56528	0.254648	0.18081885	0.084602	0.044515	0.003852	16	0.279252622
DU91-W2-250	0.3	0.21	0.425567	0.181228	10.3836078	1.4	0.02	1.283383	0.559757	0.148545	0.2183284	0.058518	0.070343	0.014475	12	0.209439467
DU91-W2-250	0.4	0.18	0.330228	0.164429	9.421077	1.350266	0.02	1.283794	0.418917	0.095493	0.22570011	0.033703	0.070932	0.006281	7.5	0.150899667
DU91-W2-250	0.46	0.165	0.281967	0.133621	7.65591728	1.160511	0.02	1.120247	0.303697	0.076118	0.21590031	0.022102	0.03686	-0.0047	6.5	0.113446378
Riso A1-21	0.54	0.15	0.240907	0.118741	6.80335705	1.070226	0.018	1.043615	0.237858	0.058946	0.21271051	0.015361	0.025437	-0.00565	5	0.087266444
Riso A1-21	0.66	0.135	0.201066	0.105079	6.02060046	0.989524	0.0175	0.973084	0.180474	0.043406	0.20932517	0.010109	0.027289	-0.00332	3.5	0.061086511
Naca64-418	0.74	0.125	0.182522	0.095262	5.45810145	0.906691	0.006865	0.892877	0.157823	0.035846	0.19540852	0.007987	0.023294	-0.00223	3	0.052359867
Naca64-418	0.8	0.11	0.171223	0.097926	5.61074566	0.924707	0.007077	0.912391	0.150585	0.029178	0.18649468	0.006586	0.023265	-0.00157	2.2	0.038397236
Naca64-418	0.9	0.1	0.153614	0.092534	5.3017941	0.888079	0.006651	0.878639	0.129313	0.023579	0.18114737	0.005067	0.022434	-0.00114	1.5	0.026179933
Naca64-418	0.96	0.09	0.144499	0.100873	5.77957618	0.944425	0.007315	0.935636	0.128755	0.019894	0.18329005	0.004514	0.025946	-0.00085	0.5	0.008726644

3rd iteration			Eq 6.7	Eq 6.8				Eq. 6.12	Eq. 6.13		Eq. 6.23	Eq. 6.24				
	r/R	c (r) [m]	ϕ	α (rad)	α (degrees)	Cl(α)	Cd(α)	Cn	Ct	σ	a	a'	Δα	Δa'	β	
DU91-W2-250	0.2	0.24	0.561759	0.247606	14.1867937	1.2	0.09	1.063524	0.563042	0.254648	0.19264827	0.086378	0.011829	0.001776	16	0.279252622
DU91-W2-250	0.3	0.21	0.389225	0.144886	8.30135942	1.229896	0.02	1.145493	0.448207	0.148545	0.22804575	0.049768	0.009517	-0.00875	12	0.209439467
DU91-W2-250	0.4	0.18	0.302526	0.136726	7.83384706	1.179639	0.02	1.132026	0.332361	0.095493	0.23340017	0.0287	0.0077	-0.005	7.5	0.150899667
DU91-W2-250	0.46	0.165	0.271108	0.122761	7.03370109	1.093623	0.02	1.059034	0.273601	0.076118	0.21936457	0.020594	0.003484	-0.00151	6.5	0.113446378
Riso A1-21	0.54	0.15	0.234897	0.11273	6.45897206	1.03472	0.018	1.010494	0.223318	0.058946	0.21562639	0.014754	0.002916	-0.00061	5	0.087266444
Riso A1-21	0.66	0.135	0.195151	0.099165	5.68171739	0.954362	0.0175	0.939861	0.167941	0.043406	0.21335695	0.009672	0.004032	-0.00044	3.5	0.061086511
Naca64-418	0.74	0.125	0.177878	0.090618	5.19205897	0.874924	0.006503	0.862269	0.14841	0.035846	0.197952	0.007696	0.002543	-0.00029	3	0.052359867
Naca64-418	0.8	0.11	0.166807	0.09351	5.35771517	0.894756	0.006727	0.883453	0.141927	0.029178	0.18947619	0.006363	0.002982	-0.00022	2.2	0.038397236
Naca64-418	0.9	0.1	0.149746	0.088666	5.08016928	0.861444	0.006355	0.852752	0.122232	0.023579	0.18423951	0.004908	0.003092	-0.00016	1.5	0.026179933
Naca64-418	0.96	0.09	0.140226	0.0966	5.53475855	0.91576	0.006971	0.907745	0.121091	0.019894	0.18772863	0.004371	0.004437	-0.00014	0.5	0.008726644

4th iteration			Eq 6.7	Eq 6.8				Eq. 6.12	Eq. 6.13		Eq. 6.23	Eq. 6.24				
	r/R	c (r) [m]	ϕ	α (rad)	α (degrees)	Cl(α)	Cd(α)	Cn	Ct	σ	a	a'	Δα	Δa'	β	
DU91-W2-250	0.2	0.24	0.554489	0.240337	13.7702874	1.2	0.08	1.062324	0.563797	0.254648	0.19611808	0.087175	0.00347	0.000797	16	0.279252622
DU91-W2-250	0.3	0.21	0.387839	0.1435	8.22195198	1.22136	0.02	1.138211	0.443391	0.148545	0.22811511	0.049353	6.94E-05	-0.00042	12	0.209439467
DU91-W2-250	0.4	0.18	0.301067	0.135267	7.75022603	1.170649	0.02	1.123925	0.328043	0.095493	0.23379304	0.02844	0.000393	-0.00026	7.5	0.150899667
DU91-W2-250	0.46	0.165	0.270347	0.122	6.99011795	1.088938	0.02	1.054727	0.271544	0.076118	0.21960545	0.020489	0.000241	-0.00011	6.5	0.113446378
Riso A1-21	0.54	0.15	0.234193	0.112027	6.41866705	1.030565	0.018	1.006609	0.221642	0.058946	0.21597092	0.014683	0.000345	-7.1E-05	5	0.087266444
Riso A1-21	0.66	0.135	0.194263	0.098277	5.63083636	0.949328	0.0175	0.934861	0.166093	0.043406	0.21397445	0.009607	0.000617	-6.6E-05	3.5	0.061086511
Naca64-418	0.74	0.125	0.177378	0.090118	5.16338795	0.871476	0.006465	0.858943	0.147408	0.035846	0.19822358	0.007664	0.000272	-3.2E-05	3	0.052359867
Naca64-418	0.8	0.11	0.166243	0.092946	5.32539355	0.890899	0.006683	0.879722	0.140833	0.029178	0.18985741	0.006335	0.000381	-2.9E-05	2.2	0.038397236
Naca64-418	0.9	0.1	0.149212	0.088132	5.04957682	0.857748	0.006315	0.849156	0.121267	0.023579	0.18467052	0.004886	0.000431	-2.2E-05	1.5	0.026179933
Naca64-418	0.96	0.09	0.139494	0.095867	5.49280637	0.910802	0.006913	0.902916	0.119794	0.019894	0.18850063	0.004346	0.000774	-2.5E-05	0.5	0.008726644

Fig. B1 – Blade Element Theory code to estimate mechanical output power.

Appendix C – MATLAB Scripts for the fmincon optimization function coupled with a CFD Solver.

C1 – Fmincon MATLAB Optimization Script

```
clc
clear all
close all
global gnum
gnum =1;
global A;
global B;
global C;
global velocity;
 lb=[2,4.5,4.5,4.5,4.5,2];
ub=[20,22.5,22.5,22.5,22.5,20];
x0=[10,13.49,13.48,13.47,13.46,11];
options =
optimset('algorithm','sqp','DiffMinChange',2.25,'display','iter','TolFun',0.005);
[x,fval]=fmincon(@myfun1_B_jan18th_B_1ABCDE_2,x0,[],[],[],[],lb,ub,[],option
s)
```

C2 – MATLAB Script to automate the workflow

```
function f=myfun1_B_jan18th_B_1ABCDE_2(x0)
global gnum;
global A;
global B;
global C;
global D;
global E;
global F;
global G;
global H;
global I;
global J;
global K;
global L;
global M;
global N;
global Q;
global R;
global velocity;
global velocity2;
global velocity_A;
global velocity_A2;
global P;
global S;
global T;
global U;
dir='C:\Users\Rafael Rodrigues\Documents\Rafael\Winter 2018\Week 5\';
cd(dir);
file='Design-';
filename = sprintf('%s%0.2i', file, gnum);
mkdir(filename);
pathfile = sprintf('%s%s', dir, filename);


%copy a folder (with the journal files) to this new folder (2nd row)
copyfile('C:\Users\Rafael Rodrigues\Documents\Rafael\Winter 2018\Week 5\Fluent7FF.jou',pathfile)
copyfile('C:\Users\Rafael Rodrigues\Documents\Rafael\Winter 2018\Week 5\AA7.wbjn',pathfile)
```

```
        copyfile('C:\Users\Rafael Rodrigues\Documents\Rafael\Winter 2018\Week 5\Design7.txt',pathfile)
        copyfile('C:\Users\Rafael Rodrigues\Documents\Rafael\Winter 2018\Week 5\Fluent4FF.jou',pathfile)
        copyfile('C:\Users\Rafael Rodrigues\Documents\Rafael\Winter 2018\Week 5\Design6.txt',pathfile)
        copyfile('C:\Users\Rafael Rodrigues\Documents\Rafael\Winter 2018\Week 5\AA6.wbjn',pathfile)
        copyfile('C:\Users\Rafael Rodrigues\Documents\Rafael\Winter 2018\Week 5\Design6A.txt',pathfile)
        copyfile('C:\Users\Rafael Rodrigues\Documents\Rafael\Winter 2018\Week 5\myExample2.xlsx',pathfile)
        copyfile('C:\Users\Rafael Rodrigues\Documents\Rafael\Winter 2018\Week 5\myExample2A.xlsx',pathfile)
        %copyfile('C:\Users\Rafael Rodrigues\Documents\Rafael\Winter 2018\Week 1\back_wall.prof',pathfile)

        %copy a folder (with the journal files) to this new folder (3rd row)
        copyfile('C:\Users\Rafael Rodrigues\Documents\Rafael\Winter 2018\Week 5\Fluent5FF.jou',pathfile)
        copyfile('C:\Users\Rafael Rodrigues\Documents\Rafael\Winter 2018\Week 5\Design5.txt',pathfile)
        copyfile('C:\Users\Rafael Rodrigues\Documents\Rafael\Winter 2018\Week 5\AA5.wbjn',pathfile)
        copyfile('C:\Users\Rafael Rodrigues\Documents\Rafael\Winter 2018\Week 5\Design5A.txt',pathfile)
        copyfile('C:\Users\Rafael Rodrigues\Documents\Rafael\Winter 2018\Week 5\myExample5.xlsx',pathfile)
        copyfile('C:\Users\Rafael Rodrigues\Documents\Rafael\Winter 2018\Week 5\myExample5A.xlsx',pathfile)

        %copyfile('C:\Users\Rafael Rodrigues\Documents\Rafael\Fall Quarter 2017\Week 7\velocity1.srp',pathfile)
        %copyfile('C:\Users\Rafael Rodrigues\Documents\Rafael\Fall Quarter 2017\Week 7\velocity2.srp',pathfile)

        %change matlab directory to the new folder
        cd(pathfile)

        % 1st row
        % updating distance between 1st and 2nd rows

        % string replacement to update geometry (horizontally) of the first turbine

        fin = fopen('Design7.txt');
```

```
fout = fopen('AA7.wbjn','w');
 while ~feof(fin)
   s = fgetl(fin);
   x0s=sprintf('%d',x0(1));
   s = strrep(s, '$4.5', x0s);
   fprintf(fout,'%s\n',s);
   disp(s)

  end
  fclose(fin)
  fclose(fout)


%2nd row
% string replacement to update geometry (horizontally) of the first turbine
% (second row)

fin = fopen('Design6.txt');
fout = fopen('AA6.wbjn','w');
 while ~feof(fin)
   s = fgetl(fin);
 %  x0s=sprintf('%d',x0(2));
 x0s=sprintf('%d',x0(3));
 s = strrep(s, '$3.5', x0s);
   fprintf(fout,'%s\n',s);
   disp(s)

  end
  fclose(fin)
  fclose(fout)

copyfile AA6.wbjn Design6C.txt

% string replacement to update geometry (horizontally) of the second turbine
fin = fopen('Design6C.txt');
fout = fopen('AA6.wbjn','w');
 while ~feof(fin)
   w = fgetl(fin);
   %w0w=sprintf('%d',x0(1));
   w0w=sprintf('%d',x0(2));
   w = strrep(w, '$4.5', w0w);
   fprintf(fout,'%s\n',w);
   disp(w)

  end
```

```
  fclose(fin)
  fclose(fout)

copyfile AA6.wbjn Design6C1.txt
% string replacement to update geometry: horizontal distance bet the 1st
% and 2nd turbine

fin = fopen('Design6C1.txt');
fout = fopen('AA6.wbjn','w');
 while ~feof(fin)
   w = fgetl(fin);
  % w0w=sprintf('%d',x0(5));
    w0w=sprintf('%d',x0(6));
    w = strrep(w, '$5', w0w);
   fprintf(fout,'%s\n',w);
   disp(w)

  end
  fclose(fin)
  fclose(fout)


% string replacement to update the line in front of the hub1 (in fluent)
%A=-(x0(2)-2.25);
%B=-(x0(2)+2.25);
A=-(x0(3)-2.25);
B=-(x0(3)+2.25);


fin = fopen('Design6A.txt');
fout = fopen('Fluent4FF.jou','w');
while ~feof(fin)
   v = fgetl(fin);
   y0v=sprintf('%d',A);
   v = strrep(v, '$4.5',y0v);
   fprintf(fout,'%s\n',v);
   disp(v)

  end
  fclose(fin)
  fclose(fout)

copyfile Fluent4FF.jou Design6B.txt

fin = fopen('Design6B.txt');
```

```
fout = fopen('Fluent4FF.jou','w');
while ~feof(fin)

 u = fgetl(fin);
   y0u=sprintf('%d',B);
   u = strrep(u, '$9', y0u);
   fprintf(fout,'%s\n',u);
   disp(u)
  end
  fclose(fin)
  fclose(fout)

copyfile Fluent4FF.jou Design6B_A.txt

% string replacement to update the line in front of the hub2 (in fluent)
% D=x0(1)-2.25;
% E=x0(1)+2.25;

 D=x0(2)-2.25;
 E=x0(2)+2.25;

fin = fopen('Design6B_A.txt');
fout = fopen('Fluent4FF.jou','w');
while ~feof(fin)
   v = fgetl(fin);
   y0v=sprintf('%d',D);
   v = strrep(v, '$4',y0v);
   fprintf(fout,'%s\n',v);
   disp(v)


  end
  fclose(fin)
  fclose(fout)

copyfile Fluent4FF.jou Design6B2.txt

fin = fopen('Design6B2.txt');
fout = fopen('Fluent4FF.jou','w');
while ~feof(fin)

 u = fgetl(fin);
   y0u=sprintf('%d',E);
   u = strrep(u, '$8', y0u);
   fprintf(fout,'%s\n',u);
```

```
  disp(u)
 end
 fclose(fin)
 fclose(fout)

copyfile Fluent4FF.jou Design6B3.txt

% string replacement to update moving reference origin of the first turbine
%P=-x0(2);
P=-x0(3);
fin = fopen('Design6B3.txt');
fout = fopen('Fluent4FF.jou','w');
while ~feof(fin)

 u = fgetl(fin);
  y0u=sprintf('%d',P);
  u = strrep(u, '$6.75', y0u);
  fprintf(fout,'%s\n',u);
  disp(u)
 end
 fclose(fin)
 fclose(fout)

copyfile Fluent4FF.jou Design6E.txt

% string replacement to update moving reference origin of the second turbine
 fin = fopen('Design6E.txt');
 fout = fopen('Fluent4FF.jou','w');
 while ~feof(fin)
  u = fgetl(fin);
   y0u=sprintf('%d',x0(2));
  u = strrep(u, '$5', y0u);
  fprintf(fout,'%s\n',u);
   disp(u)
  end
  fclose(fin)
  fclose(fout)

% everything ok till here

%3rd row
% string replacement to update geometry (horizontally) of the first turbine
% (third row)

fin = fopen('Design5.txt');
```

```
fout = fopen('AA5.wbjn','w');
 while ~feof(fin)
   s = fgetl(fin);
   %x0s=sprintf('%d',x0(4));
   x0s=sprintf('%d',x0(5));
   s = strrep(s, '$3.5', x0s);
   fprintf(fout,'%s\n',s);
   disp(s)

  end
  fclose(fin)
  fclose(fout)

copyfile AA5.wbjn Design5C.txt

% string replacement to update geometry (horizontally) of the second turbine
fin = fopen('Design5C.txt');
fout = fopen('AA5.wbjn','w');
 while ~feof(fin)
   w = fgetl(fin);
   %w0w=sprintf('%d',x0(3));
   w0w=sprintf('%d',x0(4));
   w = strrep(w, '$4.5', w0w);
   fprintf(fout,'%s\n',w);
   disp(w)

  end
  fclose(fin)
  fclose(fout)

copyfile AA5.wbjn Design5C1.txt

% string replacement to update geometry: horizontal distance bet the 1st
% and 2nd turbine
% no longer needed Jan10th

%fin = fopen('Design5C1.txt');
%fout = fopen('AA5.wbjn','w');
% while ~feof(fin)
%   w = fgetl(fin);
 %  w0w=sprintf('%d',x0(6));
 %  w = strrep(w, '$7', w0w);
 %  fprintf(fout,'%s\n',w);
 %  disp(w)
```

```
 % end
 % fclose(fin)
 % fclose(fout)

% string replacement to update the line in front of the hub1 (in fluent)
%G=-(x0(4)-2.25);
%H=-(x0(4)+2.25);
G=-(x0(5)-2.25);
H=-(x0(5)+2.25);


fin = fopen('Design5A.txt');
fout = fopen('Fluent5FF.jou','w');
while ~feof(fin)
   v = fgetl(fin);
   y0v=sprintf('%d',G);
   v = strrep(v, '$4.5',y0v);
   fprintf(fout,'%s\n',v);
   disp(v)

  end
  fclose(fin)
  fclose(fout)

copyfile Fluent5FF.jou Design5B.txt

fin = fopen('Design5B.txt');
fout = fopen('Fluent5FF.jou','w');
while ~feof(fin)

 u = fgetl(fin);
   y0u=sprintf('%d',H);
   u = strrep(u, '$9', y0u);
   fprintf(fout,'%s\n',u);
   disp(u)
  end
  fclose(fin)
  fclose(fout)

copyfile Fluent5FF.jou Design5B_A.txt

% string replacement to update the line in front of the hub2 (in fluent)
J=x0(4)-2.25;
K=x0(4)+2.25;
%J=x0(3)-2.25;
```

```
%K=x0(3)+2.25;


% copyfile Fluent4FF.jou Design6B_A.txt

fin = fopen('Design5B_A.txt');
fout = fopen('Fluent5FF.jou','w');
while ~feof(fin)
   v = fgetl(fin);
   y0v=sprintf('%d',J);
   v = strrep(v, '$4',y0v);
   fprintf(fout,'%s\n',v);
   disp(v)


  end
  fclose(fin)
  fclose(fout)

copyfile Fluent5FF.jou Design5B2.txt

fin = fopen('Design5B2.txt');
fout = fopen('Fluent5FF.jou','w');
while ~feof(fin)

 u = fgetl(fin);
   y0u=sprintf('%d',K);
   u = strrep(u, '$8', y0u);
   fprintf(fout,'%s\n',u);
   disp(u)
  end
  fclose(fin)
  fclose(fout)

copyfile Fluent5FF.jou Design5B3.txt

% string replacement to update moving reference origin of the first turbine
%S=-x0(4);
S=-x0(5);

fin = fopen('Design5B3.txt');
fout = fopen('Fluent5FF.jou','w');
while ~feof(fin)

 u = fgetl(fin);
```

```
   y0u=sprintf('%d',S);
   u = strrep(u, '$6.75', y0u);
   fprintf(fout,'%s\n',u);
   disp(u)
  end
  fclose(fin)
  fclose(fout)

copyfile Fluent5FF.jou Design5E.txt

% string replacement to update moving reference origin of the second turbine
 fin = fopen('Design5E.txt');
 fout = fopen('Fluent5FF.jou','w');
 while ~feof(fin)
  u = fgetl(fin);
   y0u=sprintf('%d',x0(4));
  u = strrep(u, '$5', y0u);
  fprintf(fout,'%s\n',u);
   disp(u)
  end
  fclose(fin)
  fclose(fout)

copyfile Fluent5FF.jou Design5G.txt


%change matlab directory to the new folder
cd(pathfile)


% ****First row of turbines: simulation****

% run output.wbjn (new geometrical design), run workbench to generate a new msh
file
! runwb2 -i -R AA7.wbjn -X

% copy mesh file to the pathfile (work directory)
copyfile('C:\Users\Rafael Rodrigues\Documents\Rafael\Winter 2018\Week
5\Oct5th_E_1st_row_A_files\dp0\FFF\MECH\FFF.1.msh',pathfile)
delete('C:\Users\Rafael Rodrigues\Documents\Rafael\Winter 2018\Week
5\Oct5th_E_1st_row_A_files\dp0\FFF\MECH\FFF.1.msh')

cd(pathfile)

% run the new mesh file on fluent
```

```
! fluent fluent 3ddp -t8 -i Fluent7FF.jou -wait

cd(pathfile)

% ****Second row of turbines: simulation****

% run output.wbjn (new geometrical design), run workbench to generate a new msh
file
! runwb2 -i -R AA6.wbjn -X

% copy mesh file to the pathfile (work directory)
copyfile('C:\Users\Rafael Rodrigues\Documents\Rafael\Winter 2018\Week
5\Oct5th_E1_files\dp0\FFF\MECH\FFF.1.msh',pathfile)
delete('C:\Users\Rafael Rodrigues\Documents\Rafael\Winter 2018\Week
5\Oct5th_E1_files\dp0\FFF\MECH\FFF.1.msh')

cd(pathfile)

% run the new mesh file on fluent
! fluent fluent 3ddp -t8 -i Fluent4FF.jou -wait

cd(pathfile)

% scan the velocity at the wake (a line right in front of the hub1)
velocity=textscan(fopen('velocity1_2ndrow.srp'),'%s');
velocity=velocity{1}{20};
velocity=str2double(velocity);

% calculate power acording to the velocity at the wake (hub-line1)
filename = 'myExample2.xlsx';
M = {'Free-Stream Velocity','Angular velocity';velocity,44.45;15,30};
sheet = 1;
xlRange = 'U3';
xlswrite(filename,M,sheet,xlRange);

% scan the velocity at the wake (a line right in front of the hub)
velocity2=textscan(fopen('velocity2_2ndrow.srp'),'%s');
velocity2=velocity2{1}{16};
velocity2=str2double(velocity2);

% calculate power acording to the velocity at the wake (hub-line1)
filename2 = 'myExample2A.xlsx';
Q = {'Free-Stream Velocity','Angular velocity';velocity2,44.45;15,30};
sheet = 1;
xlRange = 'U3';
```

```
xlswrite(filename2,Q,sheet,xlRange);

% Third  row of turbines: simulation

% run output.wbjn (new geometrical design), run workbench to generate a new msh
file
! runwb2 -i -R AA5.wbjn -X

% copy mesh file to the pathfile (work directory)
copyfile('C:\Users\Rafael Rodrigues\Documents\Rafael\Winter 2018\Week
5\Oct5th_E1A_files\dp0\FFF\MECH\FFF.1.msh',pathfile)
delete('C:\Users\Rafael Rodrigues\Documents\Rafael\Winter 2018\Week
5\Oct5th_E1A_files\dp0\FFF\MECH\FFF.1.msh')

cd(pathfile)

% run the new mesh file on fluent
! fluent fluent 3ddp -t8 -i Fluent5FF.jou -wait

cd(pathfile)

% scan the velocity at the wake (a line right in front of the hub1)
velocity_A=textscan(fopen('velocity1_3rdrow.srp'),'%s');
velocity_A=velocity_A{1}{20};
velocity_A=str2double(velocity_A);

% calculate power acording to the velocity at the wake (hub-line1)
filename3 = 'myExample5.xlsx';
N = {'Free-Stream Velocity','Angular velocity';velocity_A,44.45;15,30};
sheet = 1;
xlRange = 'U3';
xlswrite(filename3,N,sheet,xlRange);

% scan the velocity at the wake (a line right in front of the hub1)
velocity_A2=textscan(fopen('velocity2_3rdrow.srp'),'%s');
velocity_A2=velocity_A2{1}{16};
velocity_A2=str2double(velocity_A2);

% calculate power acording to the velocity at the wake (hub-line1)
filename4 = 'myExample5A.xlsx';
R = {'Free-Stream Velocity','Angular velocity';velocity_A2,44.45;15,30};
sheet = 1;
xlRange = 'U3';
xlswrite(filename4,R,sheet,xlRange);
```

```
filename = 'myExample2.xlsx';
column = xlsread(filename,'U54:U54')
filename2 = 'myExample2A.xlsx';
column2 = xlsread(filename2,'U54:U54')
filename3='myExample5.xlsx';
column3 = xlsread(filename3,'U54:U54')
filename4='myExample5A.xlsx';
column4 = xlsread(filename4,'U54:U54')
%f=column/(x(4)*(x0(1)*x0(3)))+column2/(x(8)*(x0(5)*x0(7)));

% last fmincon objective function Jan10th
f=(column+column2)/((x0(2)+x0(4))*0.5*0.5*(x0(1)+x0(3)))+(column3+column4)/((x0(
6)+x0(8))*0.5*0.5*(x0(5)+x0(7)));

% Jan 31st f=(330/(x0(6)*27))+
(column+column2)/((x0(1)+x0(2))*x0(5))+(column3+column4)/((x0(3)+x0(4))*20);

% Jan31st correction
% f=(660/((x0(1)+31.4)*27))+
(column+column2)/((x0(2)+x0(3))*(x0(6)+31.4))+(column3+column4)/((x0(4)+x0(5))*3
1.4);

% f=1/((660/((x0(1)+31.4)*27))+
(column+column2)/((x0(2)+x0(3))*(x0(6)+31.4))+(column3+column4)/((x0(4)+x0(5))*3
1.4));

T=(660/((x0(1)+31.4)*27))+
(column+column2)/((x0(2)+x0(3))*(x0(6)+31.4))+(column3+column4)/((x0(4)+x0(5))*3
1.4);
U=-T;

f=U;

fclose('all')
gnum=gnum+1;
cd(dir)
```

C3 – ANSYS Fluent Journal Files

file read-case FFF.1.msh

define units angular-velocity rpm

file read-profile back_wall.prof

define models viscous kw-sst yes

define materials change-create air air yes ideal-gas no no no no no no

define boundary-conditions fluid rotative_fluid_1 no no no yes 24 no 424.49 no 0 no 0 no 0 no 2.25 no 0 no $6.75 no 1 no 0 no 0 none no no no no no

define boundary-conditions fluid rotative_fluid_2 no no no yes 23 no 424.48 no 0 no 0 no 0 no 2.25 no 0 no $5 no 1 no 0 no 0 none no no no no no

define boundary-conditions zone-type inf_wall wall

define boundary-conditions zone-type back_wall pressure-outlet

define boundary-conditions zone-type lat_wall1 pressure-far-field

define boundary-conditions zone-type lat_wall2 pressure-far-field

define boundary-conditions zone-type sup_wall pressure-far-field

define boundary-conditions velocity-inlet velocity_inlet no yes yes no 0 yes yes no back_wall x-velocity yes no back_wall y-velocity yes no back_wall z-velocity no 300 yes yes no back_wall turb-kinetic-energy yes no back_wall specific-diss-rate

define boundary-conditions wall inf_wall 0 no 0 no no no 0 no no yes shear-bc-spec-shear no 0 no 0.5 no 0 no 0 no 0 no 1

define boundary-conditions pressure-far-field lat_wall1 no 0 no 0.1 no 300 yes no 1 no 0 no 0 no no yes 5 10

define boundary-conditions pressure-far-field lat_wall2 no 0 no 0.1 no 300 yes no 1 no 0 no 0 no no yes 5 10

define boundary-conditions pressure-far-field sup_wall no 0 no 0.1 no 300 yes no 1 no 0 no 0 no no yes 5 10

solve set p-v-coupling 24

solve monitors residual plot yes

solve monitors force set-drag-monitor cd yes rotor () no no yes 2 no 1 0 0

solve monitors force set-lift-monitor cl yes rotor () no no yes 3 no 1 0 0

solve initialize hyb-initialization

solve iterate 80

file write-case-data output2.cas.gz

surface line-surface line-hub1 1.25 0 $4.5 1.25 0 $9

surface line-surface line-hub2 1.25 0 $4 1.25 0 $8

report surface-integrals facet-avg line-hub1 line-hub1 () x-velocity yes velocity1_2ndrow.srp

report surface-integrals facet-avg line-hub1 line-hub2 () x-velocity yes velocity2_2ndrow.srp

file write-profile backwall1.prof back_wall () x-velocity y-velocity z-velocity turb-intensity turb-kinetic-energy specific-diss-rate ()

exit OK

C4 – ANSYS Workbench WBJN files

```
# encoding: utf-8
# Release 17.0
SetScriptVersion(Version="17.0.323")
Open(FilePath="C:\Users\Rafael  Rodrigues\Documents\Rafael\Winter  2018\Week 5\Oct5th_E.wbpj")


designPoint1 = Parameters.GetDesignPoint(Name="0")
parameter1 = Parameters.GetParameter(Name="P1")
designPoint1.SetParameterExpression(
   Parameter=parameter1,
   Expression="$4.5 [m]")


parameter2 = Parameters.GetParameter(Name="P2")
designPoint1.SetParameterExpression(
   Parameter=parameter2,
   Expression="$4.5 [m]")

parameter3 = Parameters.GetParameter(Name="P3")
designPoint1.SetParameterExpression(
   Parameter=parameter3,
   Expression="$3.5 [m]")


parameter4 = Parameters.GetParameter(Name="P4")
designPoint1.SetParameterExpression(
   Parameter=parameter4,
   Expression="$3.5 [m]")


parameter5 = Parameters.GetParameter(Name="P5")
designPoint1.SetParameterExpression(
   Parameter=parameter5,
   Expression="$5 [m]")

parameter6 = Parameters.GetParameter(Name="P6")
designPoint1.SetParameterExpression(
   Parameter=parameter6,
   Expression="$5 [m]")
```

```
system1 = GetSystem(Name="FFF")
geometryComponent1 = system1.GetComponent(Name="Geometry")
geometryComponent1.Update(AllDependencies=True)
meshComponent1 = system1.GetComponent(Name="Mesh")
meshComponent1.Update(AllDependencies=True)


##save as file
Save(
   FilePath="C:\Users\Rafael Rodrigues\Documents\Rafael\Winter 2018\Week 5\Oct5th_E1.wbpj", Overwrite=True)
```

Appendix D – Mesh Sensitivity Study

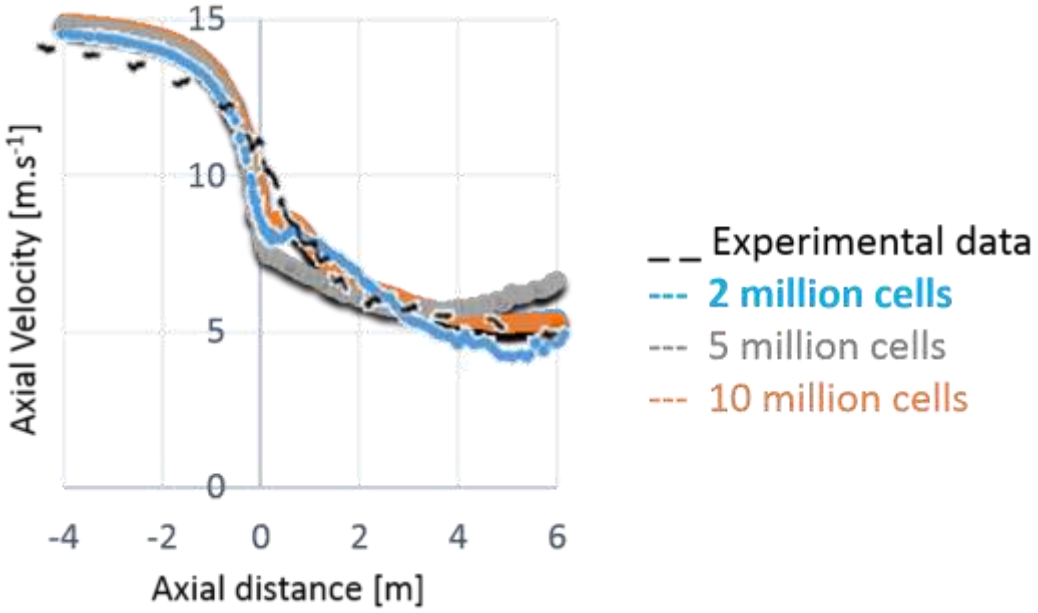

Figure D.1 – Mesh sensitivity study for study 1 (chapter 2).

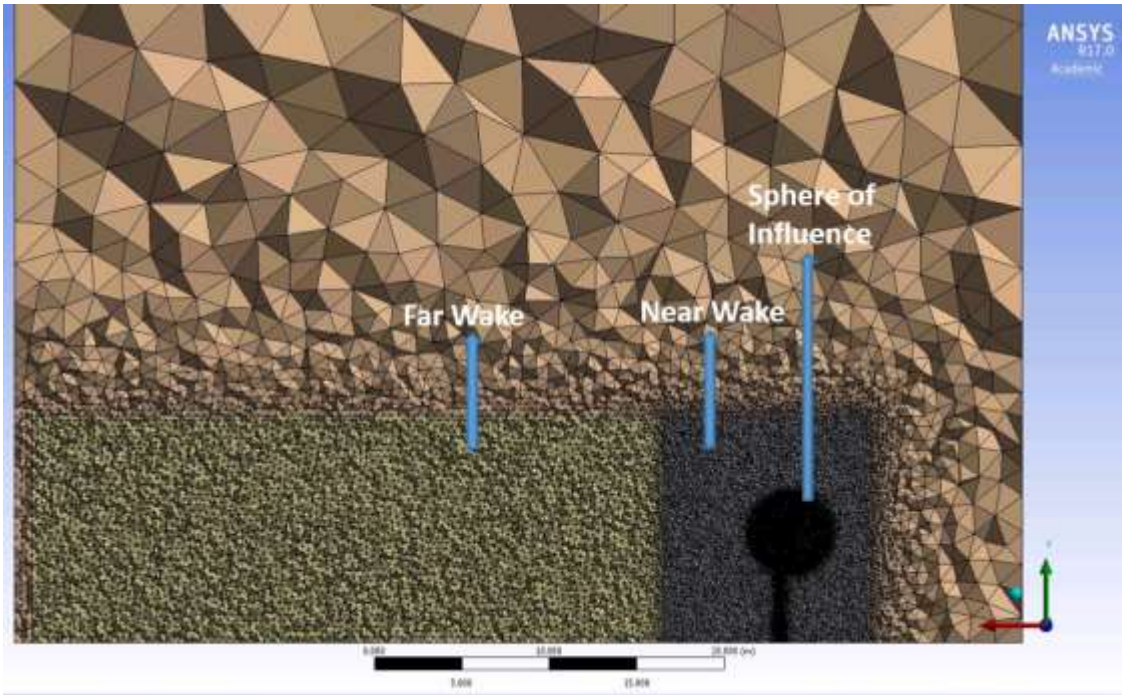

Figure D.2 – Physical domain showing the refinement of the mesh at different regions in the wake.

Table D.1 – Four cases of mesh sensitivity study

	Elements	Nodes	Rotor [m]	Central Disc [m]	Sphere of Influence [m]	Near Wake [m]	Far Wake [m]
Case 1	19,602,483	3,325,671	0.025	0.05	0.075	0.15	0.3
Case 2	10,424,238	1,782,980	0.025	0.05	0.075	0.2	0.4
Case 3	7,055,590	1,215,712	0.025	0.05	0.075	0.25	0.5
Case 4	4,025,982	705,040	0.025	0.05	0.075	0.5	0.75

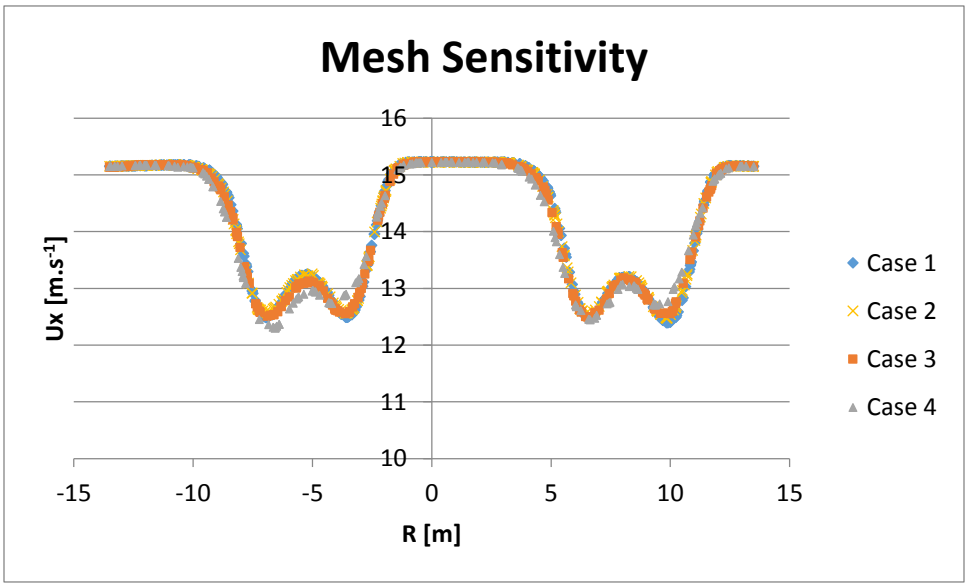

Figure D.3 – Mesh Sensitivity Study.